

**A SERIAL-PARALLEL HYBRID ROBOT FOR
MACHINING OF COMPLEX SURFACES**

YAN SHIJUN

(M.ENG. BUAA)

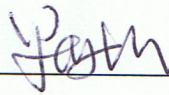
A THESIS SUBMITTED
FOR THE DEGREE OF DOCTOR OF PHILOSOPHY
DEPARTMENT OF MECHANICAL ENGINEERING
NATIONAL UNIVERSITY OF SINGAPORE

2015

DECLARATION

I hereby declare that this thesis is my original work and it has been written by me in its entirety. I have duly acknowledged all the sources of information which have been used in the thesis.

This thesis has also not been submitted for any degree in any university previously.

A handwritten signature in black ink, appearing to read 'Yan Shijun', is written over a horizontal line.

Yan Shijun

01 September 2015

ACKNOWLEDGEMENTS

The author would like to express the deepest appreciation to his supervisors, Prof. Andrew Nee Yeh Ching and Assoc. Prof. Ong Soh Khim from the Department of Mechanical Engineering. During the candidature period, they continually and convincingly conveyed a spirit of adventure and persistent helps. Without their guidance, this dissertation would not have been possible.

The author also wishes to thank all the colleagues in Stewart Platform research group, Augmented Reality research group and Remanufacturing research group. Special thanks to Dr. Vincensius Billy Saputra, Dr. Fang Hongchao and Mr. Zheng Xin for their valuable suggestions, ideas, and precious friendship.

Additionally, the author wants to thank all the lecturers from the Faculty of Engineering who have taught him during the years of his study. Besides, the author appreciates the technical assistance from the staffs in the Advanced Manufacturing Laboratory, especially to Mr. Tan Choon Huat, Mr. Lim Soon Cheong, Mr. Simon Tan Suan Beng and Mr. Lee Chiang Soon, for their support to the construction of the hybrid robot. The author also thanks Dr. Geng Lin from the Singapore Institute of Manufacturing Technology and Mr. Wang Sibao from the National University of Singapore for their assistance during the machining operation using a computer numerical control system.

In this very special moment, the author extends his appreciations to his parents and his wife for their constant encouragement throughout the whole research period.

Last but not least, the author wants to thank the supports and financial assistance provided by the National University of Singapore.

TABLE OF CONTENTS

DECLARATION	i
ACKNOWLEDGEMENTS	ii
TABLE OF CONTENTS	iv
SUMMARY	ix
LIST OF TABLES	I
LIST OF FIGURES	II
LIST OF ABBREVIATIONS	V
LIST OF SYMBOLS	VII
CHAPTER 1 INTRODUCTION.....	1
1.1 Overview	1
1.2 Comparison of general methods for MOCS.....	2
1.3 Motivation of the study	3
1.3.1 Optimization of parallel manipulators	4
1.3.2 Workspace analysis of parallel manipulators	4
1.3.3 Stiffness analysis of parallel manipulators	5
1.3.4 Registration of industrial robots.....	6
1.4 Objectives of the study	7
1.5 Structure of the thesis	9
CHAPTER 2 LITERATURE REVIEW.....	12
2.1 Workspace analysis of parallel manipulators.....	12

2.1.1	Numerical methods	12
2.1.2	Geometrical methods	17
2.2	Stiffness analysis of parallel manipulators.....	19
2.2.1	Experimental methods	19
2.2.2	FEA methods	21
2.2.3	Algebraic methods	21
2.3	Optimization of parallel manipulators.....	23
2.3.1	Single performance optimization.....	23
2.3.2	Multi-performance optimization.....	25
2.4	Registration of industrial robots.....	27
2.4.1	Hand-eye calibration.....	27
2.4.2	Robot-world and hand-eye calibration.....	30
2.4.3	Registration of a hybrid robot.....	33
2.5	Conclusion.....	34
CHAPTER 3 STRUCTURE OF THE HYBRID ROBOT AND THE		
WORKSPACE ANALYSIS OF THE PARALLEL MANIPULATOR.....		36
3.1	Structure of the hybrid robot	37
3.1.1	Structure of the parallel manipulator	37
3.1.2	Structure of the hybrid robot.....	39
3.2	Kinematics of the parallel manipulator	40
3.2.1	Inverse kinematics	42
3.2.2	Forward kinematics.....	44

3.3	Workspace analysis of the parallel manipulator	45
3.3.1	Workspace boundary	45
3.3.2	Workspace volume.....	48
3.4	Comparison with the discretization method.....	51
3.5	Regular workspace	55
3.6	Conclusion.....	57
CHAPTER 4 STIFFNESS ANALYSIS OF THE PARALLEL MANIPULATOR		58
4.1	Stiffness analysis using strain energy method.....	59
4.1.1	Inverse compliant Jacobian matrix	60
4.1.2	Strain energy of the mobile platform	61
4.1.3	Strain energy of the parallelogram limb	63
4.1.4	Strain energy of the actuator	66
4.1.5	The total strain energy of a triglide.....	68
4.2	Comparison with FEA method.....	70
4.3	Stiffness index	72
4.4	Conclusion.....	78
CHAPTER 5 OPTIMIZATION OF THE PARALLEL MANIPULATOR.		80
5.1	Performance measures.....	81
5.1.1	Dexterity	81
5.1.2	Stiffness.....	84
5.1.3	Space utilization.....	84

5.2	Constraints.....	86
5.2.1	Motion range of passive joints.....	86
5.2.2	Collision-Free requirement of limbs.....	87
5.2.3	Prescribed Task Space	87
5.3	Architecture optimization.....	90
5.3.1	Design Variables	90
5.3.2	Objective functions	91
5.3.3	Solution algorithm	91
5.4	Optimization results and comparison.....	92
5.5	Conclusion.....	99
CHAPTER 6 REGISTRATION OF THE HYBRID ROBOT.....		100
6.1	The D-K method.....	101
6.2	The PN method.....	104
6.3	The POE method	106
6.4	Simulations.....	109
6.5	Experiments.....	113
6.6	Conclusion.....	117
CHAPTER 7 ACCURACY INVESTIGATION OF THE HYBRID ROBOT		
119		
7.1	Materials.....	119
7.2	Definitions.....	120
7.2.1	Circularity	120

7.2.2	Straightness	121
7.2.3	Cylindricity	121
7.3	Machining Results	121
7.4	Conclusion.....	125
CHAPTER 8 CONCLUSIONS AND FUTURE WORKS		126
8.1	Conclusions and contributions	126
8.2	Future works.....	129
REFERENCES		132
PUBLICATIONS FROM THE RESEARCH.....		143

SUMMARY

Machining of complex surfaces (MOCS) is a global technological topic. Many products are designed with complex surfaces to enhance their appearances and/or functions. Although computer numerical control (CNC) systems, serial robots and parallel manipulators are competent in completing MOCS, CNC systems lack flexibility, while serial robots find it difficult to achieve high accuracy and parallel manipulators possess smaller workspace. In an attempt to overcome these problems, this study constructs a hybrid robot to combine the advantages of a serial robot and a parallel manipulator. The serial robot works as an approximate positioner and is locked during machining. The parallel manipulator is used for fine-tuning and completes the machining task.

In order to improve the performance of the parallel manipulator, a method is proposed to optimize the dexterity, stiffness and space utilization of the parallel manipulator. Its workspace is analyzed using a geometrical method, which is capable of providing accurate boundary and volume for the manipulators with similar structures. Since most researchers ignore the deformation of the mobile platform, an algebraic expression is presented to obtain the stiffness matrix of the parallel manipulator considering the compliance of the mobile platform, the limbs and the actuators. This algebraic expression is convenient, fast and has comparable accuracy compared to a FEA method. To evaluate the stiffness property, a novel stiffness index is proposed to measure the resistance of a parallel manipulator to the deformation due to the applied external wrench. Compared with several other

indices, this index is able to relate the stiffness property to the direction of the applied wrench and avoid the interpretation difficulty of arithmetic operations between translations and orientations with different units. For the optimization of the space utilization, the variable volume of the manipulator due to its changing postures in movements is integrated into the index calculation, which has not been considered by other researchers. Comparing with the optimal solution obtained by other researchers, this study is able to obtain an optimal parallel manipulator with better dexterity, stiffness and space utilization.

The registration of the hybrid robot is crucial whenever its interaction with objects is to be detected by a tracking system. However, there is no reported solution to address this issue for a hybrid robot. This study gives a first attempt to propose several different methods to solve this problem. With the evaluation of these methods, they are able to provide globally robust solutions. The proposed Degradation-Kronecker method is faster and the purely nonlinear method is more accurate.

Finally, the accuracy of the hybrid robot is compared with a CNC machining center and a serial robot. The comparison shows that the accuracy of the hybrid robot is much better than the serial robot. Although the accuracy of the hybrid robot cannot reach the level of the CNC machining center, it should be noted that the hybrid robot is more flexible than a CNC system.

LIST OF TABLES

Table 2-1: The comparison of several methods proposed to solve HEC.....	30
Table 3-1: Dimensions of a triglide and the discretization step in z direction	52
Table 4-1: The physical properties of an analyzed triglide.....	71
Table 4-2: The configurations of the triglide and the applied wrenches on the triglide.....	71
Table 4-3: The deformation of the central point of the mobile platform.....	72
Table 5-1: Variable values of references 1, 2 and 3	94
Table 5-2: The geometrical and physical properties of the optimized parallel manipulator	94
Table 5-3: Design variables and constraints	94
Table 6-1: The average computation time of the POE, D-K and PN methods under different noise levels.....	113
Table 6-2: Dimensions of the triglide	114
Table 6-3: Average residuals and average computation time obtained with the POE, D-K and PN methods	117
Table 7-1: Information of the serial robot, the CNC machining center and the CMM.....	120
Table 7-2: Circularity, straightness and cylindricity of workpieces machined using the CNC system, the hybrid robot and the serial robot	122

LIST OF FIGURES

Figure 2-1: Radial search technique within one layer	15
Figure 2-2: General setup for displacement measurement of a parallel manipulator	20
Figure 2-3: The RWHEC setup of a serial robot	31
Figure 2-4: The registration setup of a hybrid robot.....	34
Figure 3-1: The structure of a general triglide	39
Figure 3-2: The structure of the hybrid robot	40
Figure 3-3: The structure of one limb of a triglide	41
Figure 3-4: The effective DOFs of the parallelogram structure and the U-U limb structure	42
Figure 3-5: The workspace boundary of one limb on a slicing plane.....	47
Figure 3-6: The workspace boundary of a triglide on a slicing plane	47
Figure 3-7: The flow chart for solving the workspace boundary on an arbitrary slicing plane	50
Figure 3-8: The workspace boundary obtained using the GM and the grid points obtained using the GDM on the $z = 100mm$ plane.....	54
Figure 3-9: The workspace volume obtained using the GM and the GDM.....	54
Figure 3-10: The average computation time of the GM and GDM.....	55
Figure 3-11: The workspace boundary of the triglide obtained using the GM on the slicing plane $z = 90mm$	56
Figure 3-12: The workspace boundary of a triglide on a slicing plane	56
Figure 4-1: The applied external wrench and reaction forces on the mobile platform.....	61
Figure 4-2: Internal forces and moments experienced by a cross section of the mobile platform.....	62
Figure 4-4: Internal forces and moments exerted in the bottom shaft	65
Figure 4-5: The internal force exerted in the side shaft of the limb	66
Figure 4-6: The internal force and moment experienced by the lead screw	67

Figure 4-7: The discretized workspace of a PTPM and its workspace in the plane of $z = 10\text{ mm}$	74
Figure 4-8: The distribution of the VW index of the triglide in the plane of $z = 10\text{ mm}$ when a unit wrench is applied.....	75
Figure 4-9: The distributions of the (a) determinant, (b) maximal and (c) minimal eigenvalues of the stiffness matrix in the plane of $z = 10\text{ mm}$	77
Figure 4-10: The distribution of the VW index of the triglide in the plane of $z = 10\text{ mm}$ when a different unit wrench is applied.....	78
Figure 5-1: The structure of the triglide and a constant prism and a variable prism in its structure.....	86
Figure 5-2: The motion range of a parallelogram limb.....	87
Figure 5-3: The flow chart of constraint evaluation of prescribed task space.....	90
Figure 5-4: The selection principle of the NSGA.....	92
Figure 5-5: The Pareto front obtained using the NSGA algorithm.....	96
Figure 5-6: The objective values of reference 1 and 14 optimal solutions.....	96
Figure 5-7: The objective values of reference 2 and the seven optimal solutions.....	97
Figure 5-8: The GDI, GSI and RWV of references 1, 2 and 3.....	98
Figure 6-1: The flowchart of the D-K method.....	103
Figure 6-2: The flowchart of POE method.....	109
Figure 6-3: Rotation residuals obtained from the POE, D-K and PN method.....	112
Figure 6-4: Translation residuals obtained from the POE, D-K and PN method.....	112
Figure 6-5: The experimental setup of a hybrid robot.....	114
Figure 6-6: Rotation residuals obtained using the POE, D-K and the PN method.....	115
Figure 6-7: Translation residuals obtained using the POE, D-K and the PN method.....	116
Figure 7-1: The top view of the workpiece.....	120
Figure 7-2: The machined workpieces using the CNC machining center, the hybrid robot and the serial robot.....	123

Figure 7-3: Surfaces of the semi-circle platforms machined using the CNC machining center, the hybrid robot and the serial robot123

Figure 7-4: The error ranges of the workpieces machined using the CNC machine, the hybrid robot and the serial robot124

LIST OF ABBREVIATIONS

CMM	Coordinate measuring machine
CNC	Computer numerical control
D-K	Degradation-Kronecker
DOF	Degree of freedom
FEA	Finite element analysis
GA	Genetic algorithm
GCI	Global conditioning index
GDI	Global dexterity index
GDM	Grid discretization method
GM	Geometrical method
GSI	Global stiffness index
HEC	Hand-eye calibration
L-M	Levenberg–Marquardt
MOCS	Machining of complex surface
NBI	Normal Boundary Intersection
NSGA	Non-dominance sorted genetic algorithm
PN	Purely nonlinear
POE	Product of exponentials
PUU	Prismatic-universal-universal limb structure of a parallel manipulator
RWHEC	robot-world and hand-eye calibration
RWV	Ratio of the workspace to dimensional volume
SVD	Singular value decomposition

UPU	Universal-prismatic-universal limb structure of a parallel manipulator
UU	Universal-Universal limb structure of a parallel manipulator
VW	Virtual work

LIST OF SYMBOLS

η_c	Global conditioning index
η	Global dexterity index
J	Jacobian matrix
κ	Condition number of the Jacobian matrix
η_κ	Global stiffness index
κ_V	Virtual work stiffness index
η_V	Ratio of the workspace to dimensional volume of a parallel manipulator
W	Workspace
X, Y, Z	Unknown transformation matrix
A, B, C	Known transformation matrix
O	Global coordinate frame
O'	Local coordinate frame
R_a	Radius of the base plate of a parallel manipulator
R_b	Radius of the mobile platform of a parallel manipulator
l	Limb length of a parallel manipulator
α	Tilting angle between the actuator and the base plate of a parallel manipulator
d_i	Moving distance of a translational actuator
s_d	Full stroke distance of a translational actuator
\mathbf{s}_i	Unit vector of a translational actuator
x, y, z	Spatial position of the mobile platform of a parallel

	manipulator
V	Workspace volume
Δz	Increment between two adjacent slicing planes
\mathbf{K}	Overall stiffness matrix
\mathbf{W}	Applied external wrench
$\delta\xi$	Infinitesimal twist
$\delta\chi$	Infinitesimal translation
$\delta\psi$	Infinitesimal rotation
U	Strain energy
\mathbf{C}	Overall compliance matrix
\mathbf{A}	Inverse compliant Jacobian matrix
\mathbf{f}	Reaction forces exerted at the six upper ball joints of three parallelogram limbs
U_{MP}	Strain energy of the mobile platform
E_{MP}	Elastic modulus of the mobile platform
G_{MP}	Shear modulus of the mobile platform
$I_{MP,i}$	Area moment of inertia of the cross section of the mobile platform
$J_{MP,i}$	Polar moment of inertia of the cross section of the mobile platform
$A_{MP,i}$	Area of the cross section of the mobile platform
E_{uPL}	Elastic modulus of the bottom shaft of a parallelogram limb
$I_{uPL,i}$	Area moment of inertia of the bottom shaft of a parallelogram limb

$A_{uPL,i}$	Area of the cross section of the bottom shaft of a parallelogram limb
$E_{vPL,i}$	Elastic modulus of the side shaft of a parallelogram limb
$A_{vPL,i}$	Area of the cross section of the side shaft of a parallelogram limb
U_{ES}	Strain energy of the bottom shafts
U_{LS}	Strain energy of the side shafts
U_{PL}	Strain energy of a parallelogram limb
P_i	Lead of the lead screw of a translational actuator
k_{tor}	Torsional stiffness of a motor
N	Transmission ratio of a gear box
$E_{AS,i}$	Elastic modulus of the lead screw of a translational actuator
$G_{AS,i}$	Shear modulus of the lead screw of a translational actuator
$J_{As,i}$	Polar moment of inertia of the cross section of the lead screw
$A_{As,i}$	Area of the cross section of the lead screw
F_x	Force in the x direction of the global coordinate frame
F_y	Force in the y direction of the global coordinate frame
F_z	Force in the z direction of the global coordinate frame
M_x	Moment about the x axis of the global coordinate frame
M_y	Moment about the y axis of the global coordinate frame
M_z	Moment about the z axis of the global coordinate frame
δx	Translation in the x direction of the global coordinate

	frame
δy	Translation in the y direction of the global coordinate frame
δz	Translation in the z direction of the global coordinate frame
δM_x	Rotation about the x axis of the global coordinate frame
δM_y	Rotation about the y axis of the global coordinate frame
δM_z	Rotation about the z axis of the global coordinate frame
μ, ν	Penalty factors defined in an optimization function of a parallel manipulator.
C_i	Constraints posed by passive joints and specified task space of a parallel manipulator
\mathbf{v}_i	Position vector of the i th joint axis of a robot
$\boldsymbol{\omega}_i$	Unit directional vector of the i th joint axis of a robot
$\hat{\boldsymbol{\omega}}_i$	Skew-symmetric matrix of $\boldsymbol{\omega}_i$
$\hat{\boldsymbol{\xi}}_i$	Twist of the i th joint of a robot
R_d	The difference between the radius of a best-fit circle and its nominal circle
R_i	The distance range of all the measured points to their best-fit circle
L_i	The distance range of these points to their best-fit line
C_R	The difference between the radii of the best-fit cylindrical surface and its nominal surface
C_i	The distance range of all the points to their best-fit surface

CHAPTER 1 INTRODUCTION

1.1 Overview

Generally, machining of complex surfaces (MOCS) refers to the manufacturing of workpieces which have free-form surfaces. Complex surfaces are widely used in the design of modern products, such as the blades of a turbine, the structural frames of an aircraft, the elegant case of an electrical appliance and anatomical implants. The increasing complexity of free-form parts makes MOCS very common in modern manufacturing. Besides the field of manufacturing, the MOCS are also encountered in orthopaedic surgeries due to unique and complex shapes of human bones.

To perform MOCS, computer numerical control (CNC) systems are widely used because of their high accuracy and ease of manipulation [1–2]. Although CNC systems have dominated this field, serial robots have also emerged for polishing free-form surfaces [3], drilling and riveting in aircraft components manufacturing [4–7] and surgical operations [8, 9]. Aircraft manufacturing seldom uses parallel manipulators for machining, while it has been reported that parallel manipulators are capable of 5-axis machining [10, 11] and can be applied in orthopaedic surgeries [12]. However, the CNC machine, serial robot and parallel manipulator suffer from their own limitations. Thus, it is necessary to make a comparison of this equipment, which will be presented in the following section.

1.2 Comparison of general methods for MOCS

As stated above, CNC systems benefit from their high accuracy and relative ease of manipulation. Generally, their high accuracy is attributed to their precise movements and large rigid tables [13]. On the other hand, the large tables also make CNC systems inflexible. The CNC systems are much larger than workpieces in general. This disadvantage makes them difficult to be used in crowded workplaces, such as the aircraft assembly line and surgical operation theatre. Compared with CNC systems, serial robots possess higher flexibility. The serial robot can also produce a large work volume with high dexterity. However, low stiffness and error accumulation from its base to its end effector are the disadvantages of a serial robot. To achieve high accuracy, parts of high stiffness and high accuracy but low weight have to be used, which will increase the cost of serial robots. Both low applied force capacity and low payload-to-weight ratio limit the applications of serial robots. In comparison, parallel manipulators generally possess high rigidity, high payload-to-weight ratio and are capable of achieving high accuracy at lower cost. However, parallel manipulators suffer from smaller work volume and lower dexterity than serial robots.

To overcome these existing issues in CNC systems, serial robots and parallel manipulators, one possible solution is to design specific systems for given tasks, such as an one-sided cell end effector described in [14] for the drilling operation in aircraft assembly. These specific systems increase the manufacturing cost and lack flexibility to satisfy the requirements of other tasks. Considering these problems, another method is to combine a parallel

manipulator and a serial robot to form a hybrid robot. In this method, the serial robot works as an approximate positioner and the parallel manipulator, which is attached to the serial robot, is used for fine-tuning to increase the accuracy. As a result, the hybrid robot is more flexible and has a lower cost than a CNC system. It also has higher accuracy than a serial robot and with a larger workspace than a parallel manipulator.

It should be noted that the attachment of a parallel manipulator onto a serial robot increases the load of the serial robot, which might weaken the stiffness of the hybrid robot. To address this issue, an optimized approach is necessary to design a compact parallel manipulator. Additionally, it is common to overlook the original reference position of the workpiece before machining. For example, during fuselage assembly of an aircraft, the position of the fuselage should be obtained first with the aid of tracking systems [15–17]. In the case of a surgical operation aided with a robotic system, the positions of the robot and the patient should be coupled to allow the robot to register the target coordinates [18–22]. Therefore, before machining with the hybrid robot, it is crucial to know the coordinates of the workpiece and the hybrid robot, if the workpiece used in MOCS lacks its original reference positions. This thesis focuses on the optimization of the parallel manipulator, and the registration of the hybrid robot.

1.3 Motivation of the study

A hybrid robot can be a combination of several serial robots, a combination of several parallel manipulators, or a combination of serial robots and parallel

manipulators. Since this study aims to combine the advantages of a serial robot and a parallel manipulator, the hybrid robot in this study is a parallel manipulator connected as the end effector of a serial robot.

1.3.1 Optimization of parallel manipulators

As parallel manipulators have good performance in terms of accuracy, rigidity and load-weight ratio, they can be applied in precision machining, medical surgery, pick-and-place operations, and other fields [23]. The performance analysis of a parallel manipulator is complex, however, a good optimization design approach is able to bring significant improvements, and this has attracted much interest from the researchers [24–32]. Although the parallel manipulator possesses several advantages, its applications are limited by its small workspace. It is also difficult to have a large workspace with a miniature parallel manipulator. Most of the research focuses on the maximization of the workspace of a parallel manipulator and/or the optimization of its performance measures. There are few studies to minimize its dimension with respect to specific tasks. Although researchers [33] have addressed a similar issue in the optimization field, the performance measures have been neglected.

1.3.2 Workspace analysis of parallel manipulators

For the study of a parallel manipulator, it is common to compute and optimize the workspace volume or the workspace boundary of the manipulator. Since it is complicated to obtain the exact boundary of the workspace, many researchers conduct space discretization and then search for feasible points within a bounded space [24, 25, 27, 29, 32–34]. The discretization method

simplifies the determination of the workspace, but the computation time of this method becomes too long to achieve an accurate result. During an optimization procedure, it is necessary to run each iterative step in the searching process. As a result, the process is very time consuming. Besides the discretization method, a geometrical method can be used to analyze the trajectory of each limb of the manipulator in space and obtain their intersections to outline the workspace boundary. Although this method can reduce computation time significantly and is accurate, it lacks general applicability. For different parallel manipulators, the workspace has to be reanalyzed, and it is difficult to consider the various physical constraints in a particular geometrical analysis.

1.3.3 Stiffness analysis of parallel manipulators

Although parallel manipulators have good performance in terms of accuracy and rigidity, it is still necessary to consider the stiffness in the pre-design stage as it is dependent on the material property, the structural configuration and its dimension. Stiffness is related to the accuracy of a manipulator since it reflects the direct mapping between the externally applied wrench and the deformation of the manipulator. Stiffness analysis of parallel manipulators has attracted constant attention of researchers [35–42]. Although experimental methods are recommended to validate the mechanical design of a robotic system, it is still challenging to set up a precise experimental configuration to investigate the stiffness of a multi-body robot, such as a parallel manipulator. Finite element analysis (FEA) methods are alternatives to the experimental methods, however, the FEA methods are typically time-consuming [43]. Compared with the FEA

methods, design using algebraic methods can deduce the stiffness of a parallel manipulator using algebraic expressions. The reported algebraic methods have generally ignored the deformation of the mobile platform. In stiffness analysis, Cheng [36] found that the deformation of a parallel manipulator using FEA is larger than that obtained using an algebraic method, in which the actuator and the limb are assumed to be flexible. Based on this finding, Cheng mentioned that the difference might be caused by neglecting the deformation of the mobile platform and the passive joints.

1.3.4 Registration of industrial robots

The registration of an industrial robot is crucial whenever its interaction with objects has to be detected by a tracking system. If a tracking system is used to guide the movements of a robot, the pose of its end-effector with respect to its origin has to be connected with a global coordinate frame. This connection can be achieved with a registration procedure which has been addressed by many researchers [44–55]. Currently, there are two registration procedures, which are the hand-eye calibration and the robot-world and hand-eye calibration. In the hand-eye calibration, the pose of the tool with respect to the camera is unknown and should be identified. In the robot-world and hand-eye calibration, the pose of the tool with respect to the flange, where the tool is fixed, and the pose of the robot's origin with respect to the camera are two unknowns and should be solved. However, none of the various solutions proposed are for the registration of a hybrid robot, which consists of a serial robot and a parallel manipulator. Different from classical registration methods, the registration of a hybrid robot has three unknowns to be determined, which include the pose of

the tool with respect to the flange, the pose of the origin of the serial robot with respect to the camera and the pose of the parallel manipulator with respect to the serial robot, i.e., two more unknowns as compared to the hand-eye calibration case, and one more unknown as compared to the robot-world and hand-eye calibration. In addition, the registration equation of a hybrid robot cannot separate the unknowns and has a product of at least two unknowns. The product couples the unknowns together, which makes it difficult to be solved using the existing methods.

1.4 Objectives of the study

A hybrid robot, which consists of a serial robot and a parallel manipulator, is more flexible and has lower cost than a CNC system for a specific task. A hybrid robot could combine and complement the advantages of the serial robot and the parallel manipulator. A heavy parallel manipulator can increase the payload of the hybrid robot. With a large manipulator, it is difficult to decrease its weight, and hence the load on the serial robot which the manipulator is attached. Additionally, a large parallel manipulator can increase the risk of collision between the manipulator and its working environment. A compact parallel manipulator, which also has competent workspace, is capable of overcoming these disadvantages. As mentioned earlier, researchers focus mostly on workspace maximization, and little attention has been paid to dimensional minimization of a parallel manipulator. It is still necessary to optimize and decrease the dimension and improve the performance of the parallel manipulator before attaching this onto the serial robot. Although workspace computation is generally necessary during the optimization of a

parallel manipulator, the current methods require considerable computation work which is time consuming. Stiffness is related to the accuracy of a parallel manipulator and many researchers have adopted the algebraic method to optimize its stiffness and workspace simultaneously. However, many researchers have ignored the deformation of the mobile platform during the computation of the stiffness matrix. It is important to have an accurate registration of an industrial robot with its task objects, but there is still no reported method for the registration of a hybrid robot.

With the shortcomings described above, this study plans to construct a hybrid robot with high accuracy and flexibility, which can be applied for MOCS. The serial robot functions as an approximate positioner, and the parallel manipulator is used for fine-tuning. To achieve this objective, a compact parallel manipulator with optimized operational performance will be presented. This parallel manipulator is designed by maximizing its ratio of workspace to dimensional volume and improving its dexterity and stiffness measures simultaneously, while maintaining a prescribed task space in its workspace. To reduce the computation load, a geometrical method will be described to determine the boundary and volume of the workspace of the parallel manipulator. The stiffness of the parallel manipulator will be analyzed considering the deformation of the mobile platform, limbs and actuators, and this method will be used to obtain the stiffness matrix during the optimization. To link the hybrid robot to the task objects, three different methods will be used to register the hybrid robot and they will be compared to identify the performances of these methods in addressing the registration process.

The optimization results can be used for the construction of a parallel manipulator in practice. Large workspace to dimensional volume ratio guarantees the configuration of a compact parallel manipulator to generate a large workspace, such that for a given task, it would yield the lowest weight and decrease the load to be attached to the serial robot. The geometrical method for analyzing the workspace of the parallel manipulator provides an efficient and accurate way to obtain the workspace boundary and volume. The algebraic method for stiffness analysis provides a general expression for a group of parallel manipulators which have similar structures. Finally, the registration method should be the first solution to address registration of hybrid robots.

1.5 Structure of the thesis

This thesis is organized as follows:

Chapter 2 is a brief review of the existing methods for workspace analysis, stiffness analysis, optimization of parallel manipulators, and registration of industrial robots.

Chapter 3 describes the structure and kinematics of the parallel manipulator and the hybrid robot used in this study, followed by the workspace analysis of the manipulator using a geometrical method. The accuracy and computation time of the method is compared to a discretization method.

An algebraic method is proposed in Chapter 4 for the stiffness analysis of a group of parallel manipulators which have similar structures. This method is compared to a FEA method to validate its accuracy. A new stiffness index is also introduced in this chapter to measure the stiffness property. This stiffness index can relate the stiffness property to the wrench applied on the manipulator for a particular task.

Chapter 5 provides the optimization of a parallel manipulator. Since the dexterity and stiffness properties are dependent of the poses of the mobile platform of the parallel manipulator, two global indices are used to measure the average dexterity and stiffness over the entire workspace. The objective function aims to maximize the ratio of workspace to the dimensional volume, global dexterity index and global stiffness index of the parallel manipulator. The optimization result is compared with a reported optimization technique, which was used to optimize the dexterity and space utilization of a parallel manipulator without considering the stiffness.

A hybrid robot is constructed based on the optimization results shown in Chapter 5. Chapter 6 proposes three different methods for the registration of the hybrid robot. These methods are compared to investigate their properties in addressing the registration of hybrid robots.

The hybrid robot is used to machine a simple part to investigate its accuracy and compared with the serial robot, which is used to fix the parallel manipulator in the hybrid robot, and a CNC machine in Chapter 7.

Chapter 8 summarizes the conclusions made in this study and the works are planned to completed in the future.

CHAPTER 2 LITERATURE REVIEW

Different hybrid robots have been proposed for industrial usage [56, 57] and surgical tasks [58–60]. Although a hybrid robot could combine the advantages of a serial robot and a parallel manipulator, the design of the parallel manipulator should be studied carefully. In this chapter, the workspace analysis, stiffness analysis, and optimization of a parallel manipulator are reviewed. The state-of-art of the registration of an industrial robot is also presented.

2.1 Workspace analysis of parallel manipulators

Since parallel manipulators present some disadvantages like small workspace and high degree of design complexity, workspace is considered one of the most important factors during the design procedure of parallel manipulators. This section reviews the existing methods for the workspace analysis of parallel manipulators. Generally, these methods can be categorized into two groups: numerical methods and geometrical methods.

2.1.1 Numerical methods

Numerical methods use discretized points to represent the approximate workspace of a parallel manipulator. A bounded spatial space, in which the workspace of a parallel manipulator is enclosed completely, is first discretized into points. With the inverse or forward kinematics of the manipulator, these discretized points which satisfy the kinematics are kept, and they are then

considered to form the workspace, if they also satisfy the constraint imposed by the motion range of passive joints and the requirement of no collision.

For numerical methods, the algorithm for the generation of candidate points is important, since it determines the computation time spent on the workspace identification. With different methods, these candidate points are generated differently.

The common method is to find a spatial bounding box which covers the entire workspace, and the bounding box is discretized into points using a given step. All the discretized points are checked one by one to remove the points outside the workspace. This method is also known as the brute force search method. During this process, many non-feasible points are included in the checking procedure and this could cause large computation load. This method was adopted by Stamper et al [24], Tsai and Joshi [25], Altuzarra et al [32], Laribi et al [33], Herrero et al [34], Rao et al [61], Cheng et al [62], and Rezaei et al [63]. Stamper et al used the Monte Carlo method to select points from the spatial box. In theory, the Monte Carlo method guarantees that points left after checking the kinematics and constraints represent the true workspace, if an infinite number of points have been chosen from the spatial box for checking. In practice, it is impossible to choose an infinite number of points. Rao et al [61] sliced the entire workspace into layers and each layer is discretized into points. With inverse kinematics, these points are tested to find an approximate workspace on each layer. However, inverse kinematics is not the only method for the checking of candidate points. Rezaei et al [63] used forward kinematics

to find points in the workspace. This technique enumerates all the possible combinations of the positions of actuators and computes the corresponding postures of the mobile platform of a parallel manipulator. This method is able to avoid the interference of infeasible points, but the point cloud obtained does not have a uniform density.

Besides this exhaustive search method, some researchers adopted the radial search technique to speed up searching [27, 64]. Wang et al [64] used a cylindrical coordinate system to search the workspace boundary. With this coordinate system, the workspace is sliced into layers and each layer is searched using the radial search method. The searching process within one layer is depicted in Figure 2-1. Generally, the starting point is located at the center of a current layer. If a unit direction and a step are given, this method finds points in this direction with an interval of the step until a point outside the workspace is found, and then searching continues in another direction from the starting point. Different from Wang et al [64], Monsarrat and Gosselin [27] conducted a spherical search algorithm to determine the workspace boundary. A spherical coordinate system was used to slice the workspace into layers intersecting at one point. Searching within one layer is similar to the method used by Wang et al [64]. Compared with the brute force search method, the radial search technique can decrease non-feasible points in the searching process.

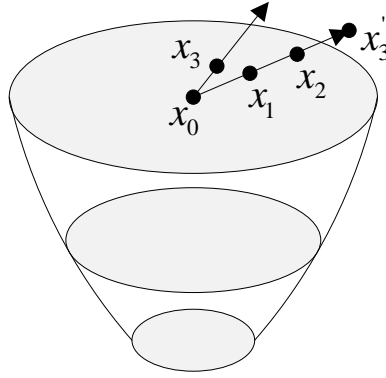


Figure 2-1: Radial search technique within one layer

However, the improvement in the computation load using radial search is not significant. Additionally, the radial search technique cannot find voids in the workspace. To address this problem, Dash et al [65] sliced the workspace into layers and each layer is discretized into many sectors. Each sector is represented by a point located in the sector. If the representative point is in the workspace, the sector is considered as one part of the workspace. This method is similar to the brute force search method, since if the result is required to be exact, the sectors have to be discretized into tiny areas. Different from the above mentioned brute force search method, Dash et al [65] used a geometrical method to estimate approximately the boundary in each layer, so that many non-feasible sectors are excluded from the checking procedure. Correspondingly, the computation speed can be improved. Nevertheless, similar to the radial search technique, the improvement is not significant.

In practice, the points on the boundary are essential for determining the workspace shape. Hence, Wang et al [66] used the information of the last boundary point to search for next boundary point. The workspace is sliced into layers first. The last boundary point of the last layer is projected into the

current layer to generate a new starting point. This point, which is inside or outside the workspace, determines whether the searching direction is outwards or inwards. With this method, it is unnecessary to search the entire workspace thoroughly. However, the voids in the workspace cannot be found.

Besides the kinematics used for the testing of candidate points, Jacobian matrices of kinematic equations can also be used to distinguish workspace boundary. Jo and Haug [67] found that boundaries of the workspace have row rank deficient Jacobian matrices. Although the Jacobian matrix can help identify the boundaries, the time complexity is similar with using kinematics. Additionally, the constraints posed by joints and no collision requirement cannot be integrated into the Jacobian matrix. To address this problem, the kinematics and the constraints can be formulated into an objective function, and then an optimization algorithm can be used to find the workspace boundary by optimizing the objective function [68, 69]. This method is capable of representing the boundary with feasible solutions, while the computation time is also considerable to reach high accuracy [69].

Generally, the advantages of numerical methods are simple implementation and ability to consider all kinds of constraints. The disadvantages are high computation cost and their accuracy is dependent on the resolution of the candidate points. High resolution can improve accuracy with significant increase of computation load.

2.1.2 Geometrical methods

Geometrical methods separate parallel mechanisms into open loops first, and then obtain the workspace of each open loop. The true workspace of a parallel manipulator is the intersection of the workspaces of all the open loops.

Gosselin [70] first presented a geometrical method to compute the workspace of a Stewart platform. A Stewart platform is a 6 degree of freedoms (DOFs) parallel manipulator. The author assumed the orientation of the manipulator was given, and then the workspace is sliced along its height into layers. The boundary in each layer is an intersection of 6 pairs of concentric circles. The total workspace could be obtained by an integration of the intersection along the height. Since the orientation is constant, the workspace obtained is called a constant orientation workspace [71]. The author did not present a method to compute the workspace with variable orientations. To complement Gosselin's work, Huang et al [72] defined the orientation capability of a 6-DOF parallel manipulator to be a range of the orientation. If the range is given, the workspace boundary corresponding to each orientation angle is obtained using a similar method to solve the constant orientation workspace. The intersection of the boundaries obtained in different orientation angles forms the workspace which can be reached by the mobile platform with variable orientations. This workspace is called the total orientation workspace [71]. In general, the total orientation workspace of a parallel manipulator is a subset of its constant orientation workspace. Although the author mentioned that the constraints could decrease the total orientation workspace, the constraints were not formulated into the closed form solution. Similar to Huang et al, Lee and

Perng [73] analyzed the position and orientation workspace of a 6-DOF Hexapod. An inscribed circle and circumscribed circle are used to approximate the workspace boundary, while constraints are ignored. Bonev and Ryu [74] found that the workspace of a parallel manipulator consists of portions of spheres, circular cylinders, elliptic cylinders, and planes if considering constraints. The intersection of these portions consists of spatial algebraic curves. Bonev and Ryu used a geometrical method to obtain intersection vertices of these curves, after which these vertices were used to reconstruct the curves and boundary surfaces of the workspace with the aid of a commercial computer aided design software. It should be noted that Bonev only considered computing the constant orientation workspace.

Besides 6-DOF parallel manipulators, several studies have been focused on 3-DOF purely translational parallel manipulators [75, 76]. An analytic expression was obtained to represent the boundary surfaces of the workspace of two 3-DOF parallel manipulators [75], while the constraints were not integrated into the expression. Pashkevich et al [76] analyzed the singularities and constraints posed by active joints of a 3-DOF parallel manipulator, the orthoglide. Considering the singularities and constraints posed by the active joints, the workspace boundary was obtained with a geometrical method. However, the constraints posed by the passive joints were ignored.

In general, geometrical methods are more accurate and faster to obtain the workspace boundary of a parallel manipulator. The main disadvantages are the lack of general applicability to solve the workspace of parallel manipulators

having different structures. Each method is designed to solve one specific manipulator configuration. Nevertheless, the property of fast computation is able to decrease the computation load significantly during an optimization process.

2.2 Stiffness analysis of parallel manipulators

Accuracy is related to the stiffness of a manipulator since stiffness reflects the direct mapping between the externally applied wrench and the deformation of the manipulator. Although parallel manipulators present good performance in terms of accuracy and rigidity, it is still necessary to consider the stiffness in the pre-design stage, as the stiffness is dependent on material property and structural configuration. Stiffness analysis of parallel manipulators attracts constant attention of researchers. Generally, the analysis methods fall into three categories, namely, experimental methods, FEA methods and algebraic methods.

2.2.1 Experimental methods

Experimental methods are recommended to validate the mechanical design of a robotic system. Nevertheless, it is still challenging to set up a precise experimental configuration to investigate the stiffness of a multi-body robot, such as a parallel manipulator.

The investigation of the stiffness is usually achieved by measuring the displacements of the manipulator under an external wrench. Figure 2-2 depicts a general setup for displacement measurement. In practice, the displacements

are attributed to the deformation of the manipulator, the clearance between connected components and the backlash of the actuators. The clearance and backlash cannot be avoided due to manufacturing and assembly tolerance and errors. Therefore, the accuracy of experimental methods cannot be guaranteed, except that the deformation can be distinguished from the clearance and backlash. However, this distinction is difficult in practice.

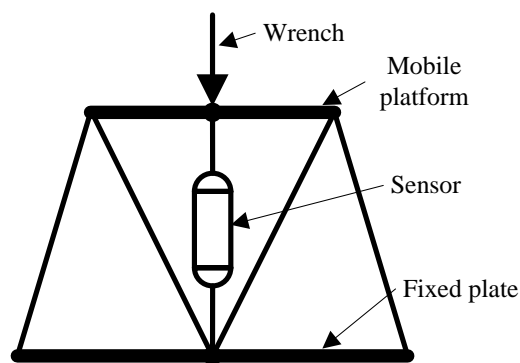


Figure 2-2: General setup for displacement measurement of a parallel manipulator

To decrease the effect of clearance and backlash, Aginaga et al [35] applied an external force in the positive and negative directions consecutively to obtain an average result, although the author admitted that error sources were not excluded successfully in the experiments. Applying a preload on a parallel manipulator is another method to reduce the clearance and backlash. This method was adopted by Huang et al [76] and Pinto et al [78]. Although the preload is able to decrease the clearance and backlash, it is difficult to determine an appropriate magnitude of the preload. Although the experimental methods are capable of obtaining the total displacement of a parallel

manipulator under an external wrench, it is difficult to isolate its deformation of from the source errors, and the effect of source errors is still unknown.

2.2.2 FEA methods

FEA methods are alternatives to the experimental methods. With appropriate settings, modelling and meshing, FEA methods are able to obtain accurate results. Therefore, the FEA methods have been adopted by many researchers to evaluate their analytical results [36–41]. Generally, commercial FEA software is used to implement the analysis. Before the analysis, some assumptions have to be made, such as Rezaei [37] who assumed all the passive joints to be rigid. The motors of the actuators are modelled using linear spring elements. FEA methods are generally very time-consuming [43].

Since stiffness is dependent of the configuration and dimension of a parallel manipulator, FEA methods always require a complete re-meshing and re-calculation if the configuration or the dimension is changed. Re-meshing can generate a huge computation load if the stiffness is considered in the optimization design stage.

2.2.3 Algebraic methods

Compared with FEA methods, algebraic methods deduce the stiffness of a parallel manipulator using algebraic expressions. With algebraic expressions, it is easy to obtain the stiffness matrix even if the configuration or the dimension has been changed.

However, algebraic methods always require several assumptions to be made. Gosselin [42] used a Jacobian matrix, which relates the velocity of the mobile platform of a parallel manipulator to the velocities of the actuators, to quantify the stiffness matrix. This quantification considers the compliance of the actuators, while the other components are assumed to be rigid. Several researchers [38, 40] considered the compliance of the limbs of a parallel manipulator while the other components are assumed to be rigid. The compliances of the limbs and the actuators have drawn much research attention [35]. El-Khasawneh [41] integrated the compliance of the limbs and the compliance of the actuators into the stiffness analysis of a Stewart platform, but had ignored the compliance of the mobile plate of the Stewart platform. Cheng [36] found that the deformation of a parallel manipulator using FEA method for stiffness analysis is larger than that obtained using the algebraic method, in which the actuators and the limbs are assumed to be flexible. Based on this finding, Cheng mentioned that the difference might be caused by neglecting the deformation of the mobile platform and the passive joints of the parallel manipulator. Rezaei [37] first considered the compliance of the mobile platform, the limbs and the actuators to analyze the stiffness of a parallel manipulator which uses three translational actuators. The compliance of the motors in the actuators was included in Rezaei's algebraic model. Nevertheless, the deformation of the lead screws in the actuators was neglected.

It can be seen that the reported algebraic methods generally ignore the deformation of the mobile platform, although Cheng [36] mentioned that this

could cause different results when compared with the FEA method. Although algebraic methods can provide an expression to obtain the stiffness matrix easily, the analysis should be carried out carefully to avoid considerably negative effect of the assumptions on the accuracy, such as the low accuracy of stiffness prediction due to the neglect of the deformation of the mobile platform.

2.3 Optimization of parallel manipulators

Optimization design of a parallel manipulator has attracted much interest from researchers to achieve high performance. These optimization methodologies can fall into two groups, namely, single performance and multi-performance optimization.

2.3.1 Single performance optimization

Single performance optimization usually only concerns one criterion in the whole process. Tsai and Joshi [25] undertook architecture optimization to maximize the global conditioning index (GCI) of a purely translational manipulator. This index assesses the distribution of the condition number of the Jacobian matrix over the entire workspace of a parallel manipulator. The condition number is a measure of the error amplification between the joints and the Cartesian spaces due to kinematic transformation. Since the Jacobian matrix depends on the configuration of the manipulator, the condition number presents only a local property of the manipulator, while the GCI gives a global property measurement. If J denotes the Jacobian matrix, W denotes the whole workspace, the GCI η_c can be obtained using Equation (2-1):

$$\eta_c = \frac{\int_w \|\mathbf{J}^{-1}\| \cdot \|\mathbf{J}\| dW}{\int_w dW} \quad (2-1)$$

The GCI first proposed by Gosselin and Angeles [79] has been widely used by researchers for the optimization of parallel manipulators [23, 27, 79, 80]. The GCI has the advantages of using a single value to describe the kinematic behavior of a parallel manipulator. It can be used to describe the performance related to dexterity and singularity. However, if the manipulator has both translation and orientation, the Jacobian matrix for computing the GCI is not homogeneous in terms of units.

The stiffness property of a parallel manipulator is another optimization aspect to be considered. Kim and Tsai [26] defined nine design variables for the maximization of the stiffness of a 3-DOF parallel manipulator with a given workspace volume which is an important property. As the exact true workspace volume is difficult to be evaluated with a given manipulator, the volume is assumed to be equal to the product of the stroke lengths of the three linear actuators used in the parallel manipulator. Kim and Tsai also assumed all the links of the manipulator to be rigid to obtain the stiffness matrix.

Maximization of the workspace volume was presented in [27] for the design of a 3-leg 6-DOF parallel manipulator. The absence of critical singularities is one of the important constraints in their optimization. The maximization of the workspace of a parallel manipulator was also presented in [31]. Their work includes constraints on actuated/passive joint limits and link interference in the

optimization, which is solved using a controlled random search algorithm. Besides workspace maximization, an optimal dimensional synthesis method of a delta parallel manipulator was presented in [33] to find the smallest workspace such that the prescribed task space can be enveloped. Since the objective is to minimize the workspace, the dimension and kinematic behavior of the robot are not considered.

Since the objective of single performance optimization contains only one criterion function, the other performance behavior might be affected or even compromised during optimization.

2.3.2 Multi-performance optimization

Since several performance behaviors might be conflicting, multi-performance optimization can guarantee that several compromising performance indices can be obtained simultaneously. An optimal design of a 3-DOF parallel manipulator was proposed in [82] with the objective of minimizing the cost function which affects the global and fluctuation condition indices. This fluctuation condition index can be interpreted as the standard deviation of GCI and it is considered to reflect the fluctuation of GCI in a specified workspace. The GCI was optimized with a global stiffness index which has been used to represent the stiffness property in [83] for a spherical parallel manipulator. In [29], the authors presented a multi-objective optimization method for the dimensional design of one class of parallel mechanism, namely, hexaslides. The global dexterity index and a workspace volume index are adopted as performance measures to be maximized. A multi-objective optimization of a

parallel manipulator was presented in [84]. A global isotropy index and a global dynamic index are chosen as the kinematic/dynamic performance quantization of the mechanism. The isotropy index is maximized while the dynamic index is simultaneously minimized in this optimization problem. The Normal Boundary Intersection (NBI) method was used to obtain Pareto-front hypersurface of the dual-objective optimal design. In [32], it also considers the kinematic and dynamic criteria. The multi-objective optimal design was presented in [85] for a 3-DOF parallel manipulator. The optimal stiffness in workspace and the transmission quality index was formulated as a single objective function. Genetic algorithm (GA) was used to solve this problem due to its robust convergence property.

In general, there are two types of methods to solve multi-objective optimization. One method is to solve the optimization problem by aggregating all the objectives into a scalar function using weighting parameters. Although this method can produce a single solution without interaction with the user, the solution is highly dependent on the setting of the weighting parameters which are unknown prior to optimization. If the optimal solution cannot satisfy the user's requirement, he/she may need to perform the optimization many times using different settings of weighting parameters until a suitable optimal solution is found [86]. The Pareto method incorporates all the objectives within the optimization process and attempts to find a set of trade-off solutions in the objective space. Once the trade-off hypersurface of the solutions is obtained, the user can select the appropriate design considering other requirements. To obtain the hypersurface, Zitzler [87] claimed that the GA

method can perform better than the random search method in multi-modal multi-objective optimization. According to Shukla and Deb [88], compared to NBI, the GA method, especially the non-dominance sorted genetic algorithm (NSGA) method, proposed in [89], performs better in achieving both convergence and diversity of solutions. However, the Pareto method needs longer computation time compared to the first type of methods, and the Pareto method provides final results near the globally optimal solution. In order to achieve the optimal solution accurately, the first type of methods can be used to improve the final results.

2.4 Registration of industrial robots

If a tracking system is used to guide the movements of a robot, the pose of its end-effector with respect to its origin and a global coordinate frame has to be coupled. This can be achieved with a registration procedure.

2.4.1 Hand-eye calibration

In the 1980s, the registration of an industrial robot was simplified as hand-eye calibration (HEC) [43, 89], and solved using several approaches. For the HEC, the registration is formulated to solve Equation (2-2), where \mathbf{X} is the transformation matrix of the relative pose of the camera with respect to the gripper of a robot, \mathbf{A} is the transformation matrix of the current pose of the gripper with respect to its last pose, and \mathbf{B} is the transformation matrix of the current pose of the camera with respect to its last pose. The camera is mounted rigidly with respect to the gripper.

$$\mathbf{AX} = \mathbf{XB} \quad (2-2)$$

Shiu and Ahmad [44] proposed a general closed-form solution where the transformation matrix is separated into its rotation and translation components. It is stated that a unique solution could be obtained with at least two sets of data [90]. In the work reported by Richter et al [45], a non-orthogonal method was used to obtain the calibration solution. This method is proven to be more accurate than the method proposed by Tsai and Lenz [90]. To guarantee the orthogonality of the rotation component, Andreff et al [91] proposed an online calibration using a two-step method for the estimation of the rotation component, while the method produces larger errors compared with an axis/angle method, dual quaternion method and nonlinear method.

Different from the previous methods, Chou and Kamel [46] used quaternions as equivalent forms of rotation and translation. Without using the least-square method to solve the over-determined equation system, a criterion was developed to choose three linear equations and one nonlinear equation to obtain the rotation and two linear equations to obtain the translation. Horaud and Dornaika [47] proposed a nonlinear technique based on the quaternion method to solve the rotation and translation simultaneously. Dual quaternion [48] is another approach to solve the calibration in order to obtain a simultaneous solution for rotation and translation.

Chen [49] made the first attempt to address this registration with the screw theory. This approach was adopted by Zhao and Liu [92], where the rotation

and translation are solved simultaneously using the singular value decomposition (SVD) analysis.

The HEC has merged with camera calibration in a few reported works [93–95]. The combined calibration approach can determine the hand-eye parameters and the camera intrinsic parameters. However, combined calibration becomes unnecessary when the camera has been calibrated using self-calibration techniques.

All these mentioned approaches require the HEC data to have a known correspondence and they cannot solve the HEC if prior knowledge of the correspondence is not known. Ackerman and Chirikjian [50] proposed a probabilistic solution for the HEC without the requirement of the correspondence. Although this approach addressed the problem caused by unknown correspondence, the authors assumed that the relative motions between consecutive reference frames were small during the calibration. They did not prove its validity in the case of large motions.

Table 2-1 summarizes the merits and shortcomings of all the methods mentioned in this subsection.

Table 2-1: The comparison of several methods proposed to solve HEC

Methods	Correspondence requirement of input and output data	Closed-form solution	Pros	Cons
Separation closed-form method [44]	Yes	Yes	Fast computation; orthogonalization is not required.	Cannot obtain the translation and rotation simultaneously; low accuracy.
Non-orthogonal method [45]	Yes	Yes	Able to obtain the translation and rotation simultaneously.	An additional orthogonalization procedure is required.
Online calibration [91]	Yes	Yes	Orthogonalization is not required.	Cannot obtain the translation and rotation simultaneously; low accuracy.
Quaternion method [47]	Yes	No	Able to obtain the translation and rotation simultaneously; orthogonalization is not required.	Low computation speed.
Dual quaternion method [48]	Yes	Yes	Able to obtain the translation and rotation simultaneously; fast computation	Lower accuracy than the Kronecker product method if used to solve robot-world and hand-eye calibration.
Screw theory method [49, 92]	Yes	Yes	Able to obtain the translation and rotation simultaneously; fast computation	Similar accuracy with the dual quaternion method.
Combined calibration approach [93-95]	Yes	No	Able to obtain the translation, rotation and camera parameters simultaneously	Low computation speed
Probabilistic solution [50]	No	Yes	Orthogonalization is not required	Cannot obtain the translation and rotation simultaneously; continuous motion of the robot is required.

2.4.2 Robot-world and hand-eye calibration

For HEC, the camera should be rigidly attached on the robot's end-effector. However, this attachment is not always necessary. For convenience, the camera can be fixed at a specific location in the environment. In this case, the

registration has more unknown parameters than that of the original HEC. The registration is also referred to as the robot-world and hand-eye calibration (RWHEC) [51, 52, 96] or the robot-world and tool-flange calibration [53, 97]. Different from HEC, the RWHEC can be formulated as in Equation (2-3), where \mathbf{X} and \mathbf{Y} are two unknown transformations. For the experimental setup in Figure 2-3, \mathbf{X} denotes the transformation from the tool to the gripper of the robot, and \mathbf{Y} is a transformation from a global coordinate frame to the base coordinate frame of the robot. The matrix \mathbf{A} denotes the transformation of the tool pose with respect to the coordinate frame of the camera and \mathbf{B} denotes the transformation of the gripper pose with respect to the origin coordinate frame of the robot. These two transformations are constant after grasping the tool with the gripper of the robot and fixing the position of the camera.

$$\mathbf{AX} = \mathbf{YB} \quad (2-3)$$

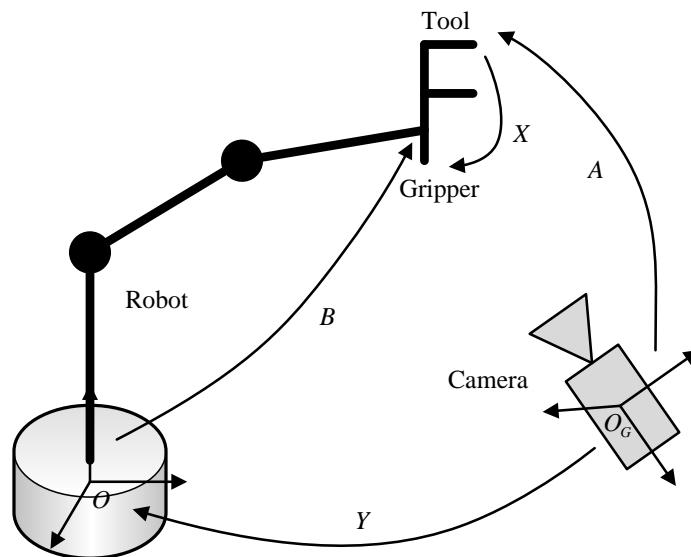


Figure 2-3: The RWHEC setup of a serial robot

Most of the solutions fall into two categories, namely, closed-form and iterative form.

A linear closed-form solution was proposed [53] to obtain the unknowns of the RWHEC with the quaternion and the screw theory. The authors [53] claimed that this method is fast and robust. In this method, each rigid transformation is separated into a rotation and a translation. This separation was adopted by Dornaika and Horaud [51] and Shah [96] in their closed-form methods. Shah [96] formulated a solution using the Kronecker product method. After comparing with the quaternion method, the Kronecker product method is proven to be reliable and accurate. To avoid accumulative errors caused by the separation, Li [52] combined the rotation and translation together and solved them using the Kronecker product method. However, the Kronecker product method fails to provide orthogonal rotation matrices. Ernst et al [97] used a similar method to solve the same equation, where the same problem has occurred. In general, closed-form methods are fast and robust although they have limited accuracy.

Different from closed-form methods, iterative methods usually have better performance but require longer computation time. In the work reported by Dornaika and Horaud [51], the rotation and translation residuals in each configuration were combined into an error function. With simulation and experimental results, it was found that the proposed nonlinear methods have better accuracy. Without a minimization function, an iterative estimation method [54] was used to solve the rotation and translation unknowns. This

method was stated to be robust against noise and convergent within a reasonable tolerance. However, the authors [54] did not compare their method with other different methods. In the work reported by Strobl and Hirzinger [55], an optimal model was built based on the minimization of the sum of prediction errors with normal distribution. After a comparison with several other methods, it was found that the proposed method presented superior performance. This method assumes that the error and noise in the registration complies with normal distribution.

2.4.3 Registration of a hybrid robot

Both HEC and RWHEC can be considered as classical registration methods. Different from the classical registration, the registration of a hybrid robot has three unknowns to be determined, i.e., two more unknowns, which include the transformation \mathbf{Y} from the coordinate frame of the camera to that of the origin of the serial robot and the transformation \mathbf{Z} from the flange of the serial robot to the base of the parallel manipulator, as compared to the HEC. As compared to RWHEC, the registration equation of the hybrid robot has one more unknown, which is the transformation \mathbf{Z} . In addition, the registration equation of a hybrid robot has two unknowns coupled together. The registration can be represented by Equation (2-4), where \mathbf{Z} is an unknown constant matrix, and \mathbf{C} is the transformation from the base of the parallel manipulator to its flange as shown in Figure 2-4.

$$\mathbf{AX} = \mathbf{YBZC} \quad (2-4)$$

Although different hybrid robots have been proposed, their registration methods have not been reported. One possible solution is a specific interface to provide a known transformation from the parallel manipulator to the serial robot. In this case, the registration becomes the same as in RWHEC. If this transformation cannot be obtained, all the closed-form solutions discussed above will not be able to provide a solution, since the closed-form solutions are proposed to solve specific registration equations; if the equations are modified, their applicability is lost.

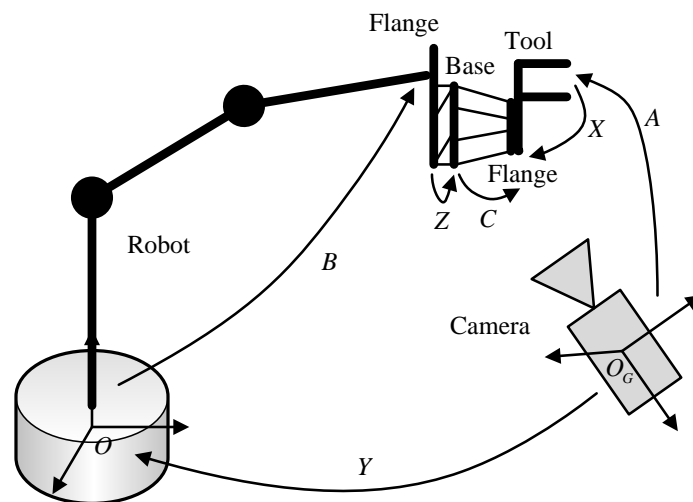


Figure 2-4: The registration setup of a hybrid robot

2.5 Conclusion

Numerical methods can obtain the workspace of a parallel manipulator and are simple to implement and deal with various constraints. However, these methods require long computation time and can generate considerable computation load if used in an optimization process. Although it is more

difficult for geometrical methods to consider all the constraints in workspace computation, they are fast and suitable to achieve optimized results.

Experimental methods are recommended to investigate the stiffness of a parallel manipulator. The difficulty is the lack of precise setup of an experiment to exclude the effects of source errors on the accuracy. FEA methods can be considered as alternatives to experimental methods. However, FEA methods have large computation load. It is time-consuming to use FEA methods to obtain the stiffness in an optimization process. During the stiffness optimization, algebraic methods are more suitable, since they are fast and have comparable accuracy with FEA methods.

Since single performance optimization concerns only one criterion, it is easy to use one objective function to measure its behavior. It should be noted that single performance optimization may deteriorate several other criteria, since some of them may be conflicting. Multi-performance optimization is able to address this issue, since it can provide results to reach compromising optimization.

Various approaches have been proposed to solve HEC and RWHEC. Since the registration of a hybrid robot is different from those in HEC and RWHEC, the proposed approaches would have some difficulty to address the registration of a hybrid robot. It is necessary to propose an appropriate method to solve this problem.

CHAPTER 3 STRUCTURE OF THE HYBRID ROBOT

AND THE WORKSPACE ANALYSIS OF THE

PARALLEL MANIPULATOR

The hybrid robot consists of a serial robot and a parallel manipulator. This chapter will first illustrate the structure of the parallel manipulator and the hybrid robot. The parallel manipulator is a parallelogram-type manipulator using translational actuators. This type of parallel manipulators can be termed a triglide [98].

Since the workspace of a parallel manipulator is limited, its analysis is a crucial step to investigate its capability during its design stage. Discretization methods are often used to solve the workspace boundary of a parallel manipulator. However, these methods generate more computation load and consume longer processing time compared with geometrical methods. Although many researchers have proposed various geometrical studies of the workspace boundary of a parallel manipulator, the analysis of a triglide has not been reported.

After the structure description, the kinematics of the parallel manipulator is presented, and then the workspace boundary of the parallel manipulator is obtained in this chapter using a geometrical method. This method is compared with the discretization method to evaluate their performance. Since the workspace of a general triglide is irregular, this chapter uses a regular workspace to represent approximately the true workspace for practical

applications, such as the determination of task space and path planning in the workspace.

3.1 Structure of the hybrid robot

3.1.1 Structure of the parallel manipulator

Stewart platform application is popular in the industry, since they can provide 3-DOF translations and 3-DOF orientations. However, more DOFs would mean more actuators and more limbs in the structure of a parallel manipulator. The weight of the manipulator will increase due to increasing number of actuators and limbs. As the proposed hybrid robot is to install a parallel manipulator at the end effector position of a serial robot, the weight of the manipulator will affect the stiffness of the hybrid robot.

In recent years, several studies have been focused on 3-DOF pure translational parallel manipulators [33, 98, 99]. In the class of 3-DOF pure translational parallel manipulators, the delta robot is probably the best known manipulator. It was first patented in 1990s [100] and has been applied for picking or packaging operations because of its fast movement. The orientation of the mobile platform of the delta robot is constrained by a parallelogram structure. However, fast movements may not be needed in other fields. After the development of the delta robot, the parallelogram structure was adopted by several researchers to construct the limbs of the linear delta [101] and the orthoglide [102], by replacing the rotary actuators of the delta robot with translational actuators. This replacement is able to decrease the velocity of its mobile platform. Besides the delta mechanism, the 3-DOF parallel

manipulator having universal-prismatic-universal (UPU) or prismatic-universal-universal (PUU) limb structure has attracted attention for its elegant and symmetric topology [25, 103, 104]. The structure of 3-PUU or 3-UPU parallel manipulator may be the simplest of all the 3-DOF pure translational parallel manipulators. Nevertheless, this structure also makes the movement of the mobile platform sensitive to the unavoidable minute clearance of the passive joints [105], making pure translation difficult to achieve with this type of structure in practice. Compared to 3-PUU or 3-UPU mechanism, the parallelogram structure used in the delta robot constrains the orientation motion of its mobile platform successfully. In this study, the linear delta and the orthoglide are grouped as pure translational parallelogram-type parallel manipulators using translational actuators, which are termed triglide. A triglide is defined to be a 3-DOF pure translational parallel kinematic manipulator which uses translational actuators and has three independent limbs, each of which is of parallelogram structure.

Figure 3-1 depicts the structure of a general triglide. A general triglide consists of a base plate, a mobile platform and three parallelogram limbs which connect the mobile platform with the base plate. Three translational actuators are distributed on the base plate. A general parallelogram contains four ball joints which link four rods together. These ball joints can be replaced with universal or rotational joints.

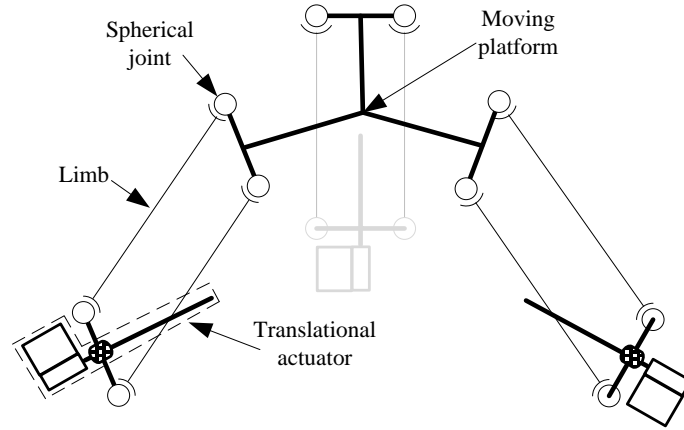


Figure 3-1: The structure of a general triglide

The DOFs of the triglide can be obtained with the modified Grübler criterion [106].

$$F = \lambda(n - j - 1) + \sum_{i=1}^j f_i - f_p \quad (3-1)$$

where F is the DOFs of a mechanism, f_i is the degrees of relative motion permitted by joint i , f_p is the passive DOFs, j is the number of joints, and n is the number of links in the mechanism, including the fixed link, and λ is the DOFs of the space in which the mechanism functions.

For a triglide, the number of passive joints is $f_p = 6$. As the triglide has three prismatic joints and 12 ball joints, $f_i = 39$ and $j = 15$. Since $n = 11$ and $\lambda = 6$, the DOFs of the triglide is $F = 3$.

3.1.2 Structure of the hybrid robot

In order to adjust the position and orientation of the parallel manipulator in space, a 5-axis serial robot, Scorbot-ER VII (Eshed Robotec Inc.), is used to

construct the hybrid robot. The serial robot works as an approximate positioner. Its function is to position the parallel manipulator near the target area. During the machining process, the serial robot is locked and the parallel manipulator is used to complete the machining operation. Figure 3-2 illustrates the structure of the hybrid robot.

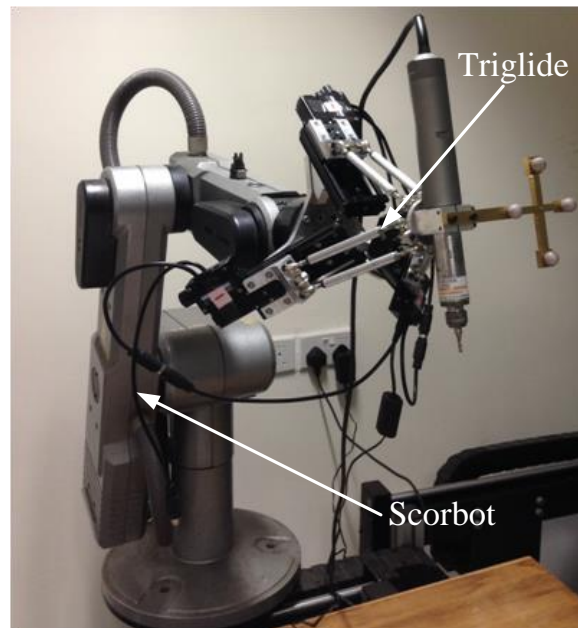


Figure 3-2: The structure of the hybrid robot

3.2 Kinematics of the parallel manipulator

It is necessary to obtain the kinematics of the parallel manipulator, since its workspace is determined by its kinematics. Considering that the coordinate frame O' is fixed with the mobile platform, while the frame O is fixed with the base plate which is considered the global frame, points A_i and C_i denote respectively the original and current position of the moving slider of the translational actuator with $i=1, 2, 3$, and d_i is the distance of A_iC_i . The length of B_iC_i is denoted by l . The distances of OA_i and $O'B_i$ are represented

respectively by R_a and R_b . The angle between the actuator's axis and the reference plane XOY is given by α . Symbols β_i and γ_i denote angles $\angle XOA_i$ and $\angle X'O'B_i$ respectively. In order to achieve a symmetric workspace, this study assumes that the triglide has three identical limbs and three identical translational actuators, and the actuators are distributed symmetrically on the base plate.

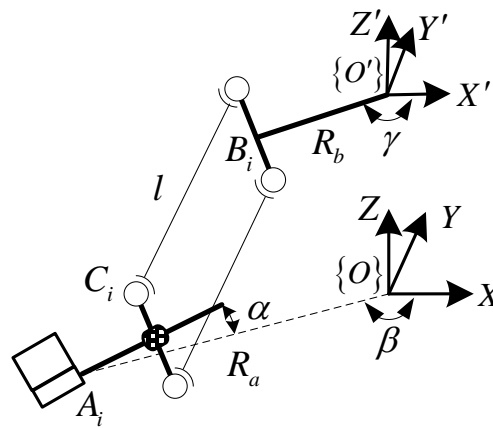
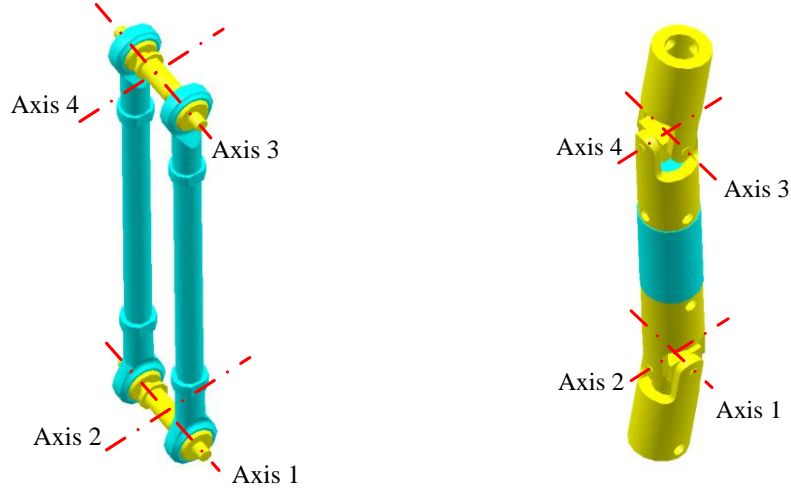


Figure 3-3: The structure of one limb of a triglide

In general, each ball joint can rotate about three orthogonal axes. However, only two axis rotations have effect on the DOFs of the parallelogram structure. Thus, this structure presents four rotation DOFs from its lower rod to its upper rod as depicted in Figure 3-4(a). In this figure, the axes 1 and 3 are parallel to each other and along the shafts of the lower and upper rods respectively. The axes 2 and 4 are perpendicular to the plane formed by the axes 1 and 3 and through the central points of the lower and upper rods respectively. This is very similar with the universal joint-universal joint (U-U) limb structure shown in Figure 3-4(b). In this figure, the axes 1 and 2 are perpendicular to each other and along the two shafts of the cross of the lower universal joint.

The axes 3 and 4 are perpendicular to each other and along the two shafts of the cross of the upper universal joint. Therefore, the kinematics of the triglide can be considered to be the same as that of a 3-PUU parallel manipulator.



(a) The parallelogram structure

(b) The U-U limb structure

Figure 3-4: The effective DOFs of the parallelogram structure and the U-U limb structure

3.2.1 Inverse kinematics

For inverse kinematics, the traveling distance of each actuator needs to be solved with the given position of O' . If \mathbf{s}_i is the unit vector of A_iC_i , it can be obtained using Equation (3-2).

$$\mathbf{s}_i = \frac{1}{\sqrt{1 + \tan^2 \alpha}} [-\cos \beta_i \quad -\sin \beta_i \quad \tan \alpha]^T \quad (3-2)$$

It can also be shown that

$$\mathbf{O}\mathbf{A}_i = [R_a \cos \beta_i \quad R_a \sin \beta_i \quad 0]^T \quad (3-3)$$

$$\mathbf{O}'\mathbf{B}_i = [R_b \cos \gamma_i \quad R_b \sin \gamma_i \quad 0]^T \quad (3-4)$$

Since the mobile platform has only three translational DOFs, it is assumed that

$\mathbf{OO}' = [x \ y \ z]^T$. Equation (3-5) can be obtained according to the geometrical relationship.

$$\mathbf{B}_i \mathbf{C}_i = \mathbf{OC}_i - \mathbf{OB}_i = (\mathbf{OA}_i + \mathbf{A}_i \mathbf{C}_i) - (\mathbf{OO}' + \mathbf{O}' \mathbf{B}_i) \quad (3-5)$$

For a simple representation, assume that

$$\begin{cases} K_{i1} = R_a \cos \beta_i - R_b \cos \gamma_i \\ K_{i2} = -\frac{\cos \beta_i}{\sqrt{1 + \tan^2 \alpha}} \\ M_{i1} = R_a \sin \beta_i - R_b \sin \gamma_i \\ M_{i2} = -\frac{\sin \beta_i}{\sqrt{1 + \tan^2 \alpha}} \\ N = \frac{\tan \alpha}{\sqrt{1 + \tan^2 \alpha}} \end{cases} \quad (3-6)$$

Equation (3-5) yields

$$\mathbf{B}_i \mathbf{C}_i = \begin{bmatrix} K_{i1} + d_i K_{i2} - x \\ M_{i1} + d_i M_{i2} - y \\ d_i N - z \end{bmatrix} \quad (3-7)$$

Since the limb length is constant, $\|\mathbf{B}_i \mathbf{C}_i\| = l$, and $K_{i2}^2 + M_{i2}^2 + N^2 = 1$. if

$$\begin{cases} B_i = 2(K_{i1} K_{i2} + M_{i1} M_{i2} - K_{i2} x - M_{i2} y - N z) \\ C_i = (K_{i1} - x)^2 + (M_{i1} - y)^2 + z^2 - l^2 \end{cases} \quad (3-8)$$

It can be obtained that

$$d_i^2 + B_i d_i + C_i = 0 \quad (3-9)$$

Hence, the solutions of the inverse kinematics are

$$d_i = \frac{-B_i \pm \sqrt{B_i^2 - 4C_i}}{2} \quad (3-10)$$

From Equation (3-10), two solutions can be obtained. Due to the limitations of the motion ranges of actuators and passive joints, there is only one solution satisfying the limitations in general.

3.2.2 Forward kinematics

The forward kinematics solves the position of the mobile platform when the travelling distance of each actuator is given. The forward kinematics solution is as follows.

$$\begin{cases} x = k_1 + zk_2 \\ y = k_3 + zk_4 \\ z = \frac{-k_6 \pm \sqrt{k_6^2 - 4k_5k_7}}{2k_5} \end{cases} \quad (3-11)$$

Coefficients $k_1, k_2, k_3, k_4, k_5, k_6$ and k_7 in Equation (3-11) can be obtained using Equation (3-12).

$$\left\{ \begin{array}{l}
k_1 = \frac{a_2c_1 - a_1c_2 + a_1c_3 - a_3c_1 - a_2c_3 + a_3c_2}{a_1b_2 - a_2b_1 - a_1b_3 + a_3b_1 + a_2b_3 - a_3b_2} \\
k_2 = \frac{a_2h_1 - a_1h_2 + a_1h_3 - a_3h_1 - a_2h_3 + a_3h_2}{a_1b_2 - a_2b_1 - a_1b_3 + a_3b_1 + a_2b_3 - a_3b_2} \\
k_3 = \frac{b_1c_2 - b_2c_1 - b_1c_3 + b_3c_1 + b_2c_3 - b_3c_2}{a_1b_2 - a_2b_1 - a_1b_3 + a_3b_1 + a_2b_3 - a_3b_2} \\
k_4 = \frac{b_1h_2 - b_2h_1 - b_1h_3 + b_3h_1 + b_2h_3 - b_3h_2}{a_1b_2 - a_2b_1 - a_1b_3 + a_3b_1 + a_2b_3 - a_3b_2} \\
k_5 = k_1^2 + k_3^2 + 1 \\
k_6 = c_1 + a_1k_3 + b_1k_1 + 2k_1k_2 + 2k_3k_4 \\
k_7 = k_2^2 + b_1k_2 + k_4^2 + a_1k_4 + d_1
\end{array} \right. \quad (3-12)$$

where, $a_i = 2(R_b \cos \gamma_i - R_a \cos \beta_i + d_i \cos \beta_i \sin \alpha_i)$,

$b_i = 2(R_b \sin \gamma_i - R_a \sin \beta_i + d_i \sin \beta_i \sin \alpha_i)$, $c_i = -2d_i \cos \alpha_i$,

$h_i = R_a^2 + R_b^2 + d_i^2 - l^2 + 2R_a \sin \alpha_i$
 $-2(R_a R_b + R_b \sin \alpha_i)(\sin \beta_i \sin \gamma_i + \cos \beta_i \cos \gamma_i)$

3.3 Workspace analysis of the parallel manipulator

3.3.1 Workspace boundary

According to the kinematics of a general triglide, Equation (3-13) can be obtained.

$$\mathbf{B}_i \mathbf{C}_i = \begin{bmatrix} \left(R_a - \frac{d_i}{\sqrt{1 + \tan^2 \alpha}} \right) \cos \beta_i - R_b \cos \gamma_i - x \\ \left(R_a - \frac{d_i}{\sqrt{1 + \tan^2 \alpha}} \right) \sin \beta_i - R_b \sin \gamma_i - y \\ \frac{d_i \tan \alpha}{\sqrt{1 + \tan^2 \alpha}} - z \end{bmatrix} \quad (3-13)$$

Since $\|\mathbf{B}_i \mathbf{C}_i\| = l$, Equation (3-14) can be obtained with Equation (3-13).

$$(x - A_i)^2 + (y - B_i)^2 + (z - C_i)^2 = l^2 \quad (3-14)$$

where
$$A_i = \left(r_a - \frac{d_i}{\sqrt{1 + \tan^2 \alpha}} \right) \cos \beta_i - r_b \cos \beta_i \quad ,$$

$$B_i = \left(r_a - \frac{d_i}{\sqrt{1 + \tan^2 \alpha}} \right) \sin \beta_i - r_b \sin \beta_i, \text{ and } C_i = \frac{d_i \tan \alpha}{\sqrt{1 + \tan^2 \alpha}} .$$

Equation (3-14) shows that each limb of a general triglide produces a spherical surface with its center located at (A_i, B_i, C_i) . As a triglide has three limbs, each location of the moving platform of the triglide is an intersection point of these three spherical surfaces.

If the workspace is sliced with a plane parallel to plane XOY, the workspace on the slicing plane can be obtained using Equation (3-15). On the slicing plane, the workspace becomes an intersection of three circles.

$$(x - A_i)^2 + (y - B_i)^2 = l^2 - (z - C_i)^2 \quad (3-15)$$

Equation (3-15) shows that the positions and radii of all the circles are dependent on the value of d_i , which is the travelling distance of the i th actuator, if the slicing plane is confirmed. Thus, the limiting values of d_i produces the workspace boundary on the slicing plane. It should be noted that the minimal value of d_i can be defined to be 0, so that $d_i \geq 0$. The center of the circle formed with one limb when $d_i = 0$ is denoted by O_{i_i} . With different values of d_i , the centers of the circles are moving away from O_{i_i} towards the other two limbs. Hence, the circle with the largest value of d_{L_i} , which is the longest distance from O_{i_i} to the circle, produces boundary sections which are

far away from O_{li} . This circle is called as distal circle. The circle with the smallest value of d_{Li} produces boundary sections which are near O_{li} , and this circle is called as proximal circle. Figure 3-5 plots the workspace boundary formed with one limb on a slicing plane. The shadowed area illustrates the true workspace. Therefore, for a triglide, the workspace on a slicing plane is the intersection of the shadowed areas formed with three limbs as shown in Figure 3-6.

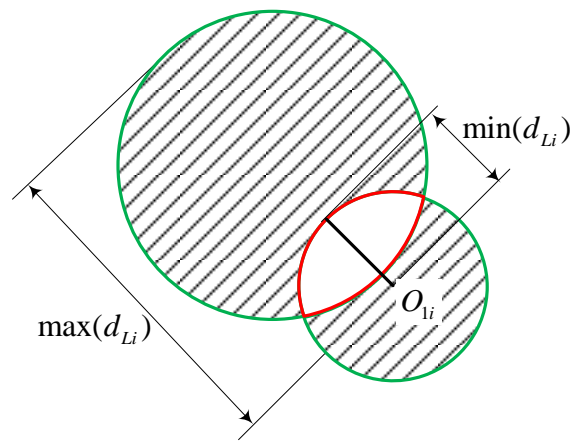


Figure 3-5: The workspace boundary of one limb on a slicing plane

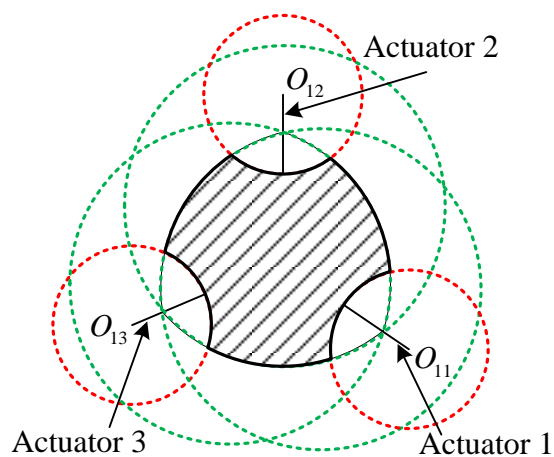


Figure 3-6: The workspace boundary of a triglide on a slicing plane

3.3.2 Workspace volume

The workspace volume V can be obtained using Equation (3-16).

$$V = \int A dz \approx \sum A \Delta z \quad (3-16)$$

where A denotes the workspace area on an arbitrary slicing plane, and Δz denotes the increment between two adjacent slicing planes. If Δz approaches 0, $V = \int A dz$.

Equation (3-16) shows that the calculation of area A which is a crucial step to obtain the workspace volume. In order to obtain area A , the boundary should be found first. Figure (3-6) presents the workspace located inside the intersection of three distal circles and outside all the proximal circles. The arcs of the distal and proximal circles constitute the workspace boundary. The following procedures provide a solution to obtain these boundary arcs. Figure (3-7) shows the flowchart of the procedures to solve the workspace boundary on an arbitrary slicing plane. After solving the workspace boundary on a slicing plane, area A can be obtained by calculating the area of the enclosed shape.

- 1 Solve the intersection of three distal circles. If the intersection exists, the arcs enclosing the intersection area can be obtained and go to step 2, else go to step 8;
- 2 Solve the intersection of the proximal circle of one limb with the distal circles of the other limbs. If intersection exists, the arcs enclosing the intersection area can be obtained and go to step 3, else go to step 4;

- 3 If the arc obtained in step 2 belongs to a distal circle, the arc's overlapped portion with the arc obtained in step 1 is removed, and the left portion of the arc obtained in step 1 is kept as a boundary, else the arc obtained in step 2 is kept as a boundary;
- 4 If any proximal circle has not been used to calculate an intersection, go to step 2, else go to step 5;
- 5 Solve the intersection of any two proximal circles. If the intersection exists, the arcs enclosing the intersection area can be obtained and go to step 6, else go to step 7;
- 6 The overlapped portion of the arc obtained in step 5 with the arc obtained in step 2 is removed and the left portion of the arc obtained in step 2 is kept as a boundary;
- 7 If the intersection of any two proximal circles has not been solved, go to step 5, else go to step 8;
- 8 If the left arcs are not empty, they constitute the workspace boundary, else the workspace is empty.

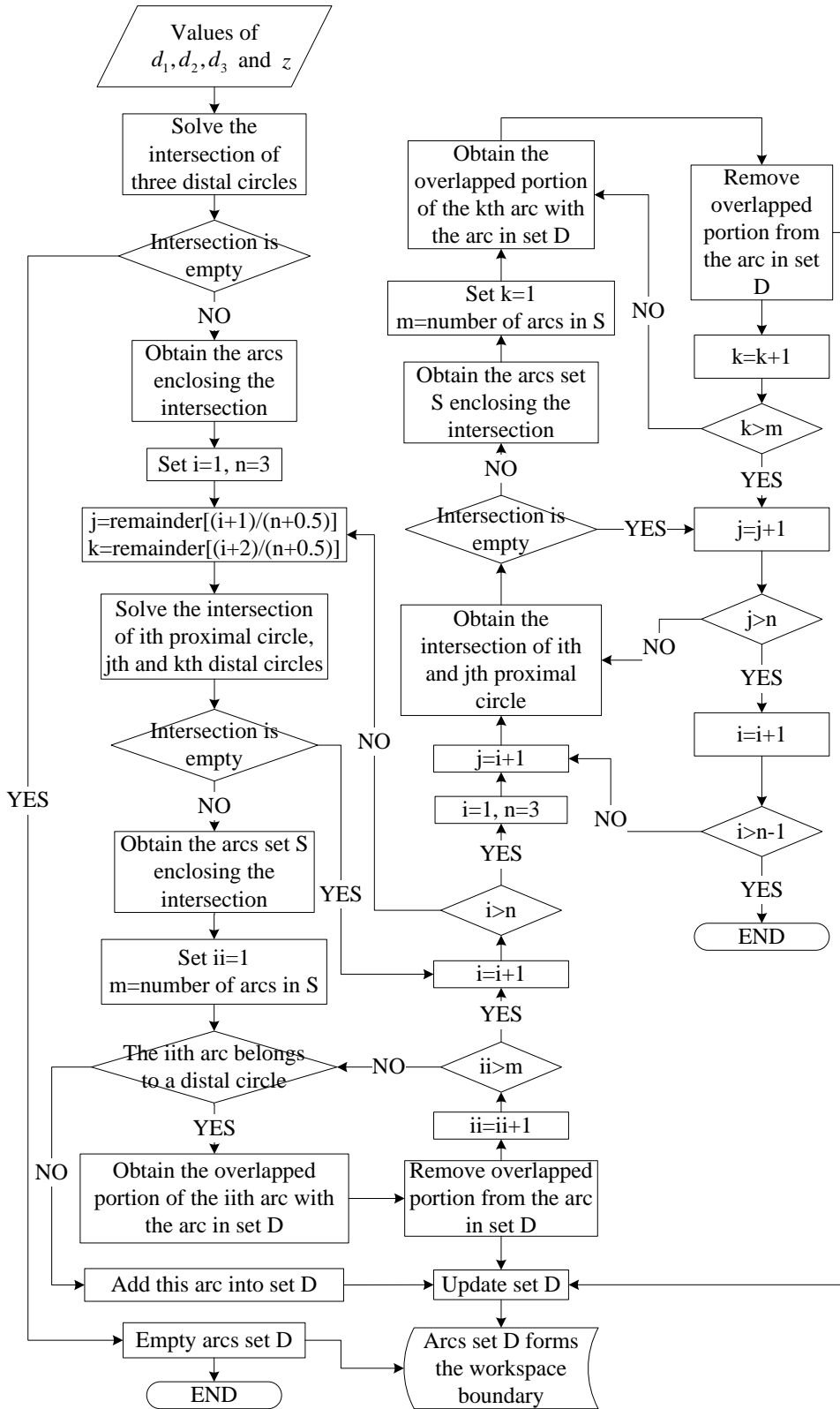


Figure 3-7: The flow chart for solving the workspace boundary on an arbitrary slicing plane

3.4 Comparison with the discretization method

This section compares the proposed geometrical method (GM) with a discretization method. This discretization method has been used by several researchers to obtain the workspace of a parallel manipulator [32–34, 61, 63]. This method is known as the grid discretization method (GDM), since it discretizes the workspace into points using a defined step, and finally these points form a grid workspace.

To obtain the workspace using the GDM, an estimation of the workspace should be provided first. This estimation determines a bounding box which is the maximum possible space to cover the workspace. For a triglide, each limb produces a spherical workspace as shown in Equation (3-14). With this sphere, it is able to confirm the limit in each direction of the workspace of each limb. After combining the limits of all the limbs, the bounding box can be obtained.

All the discretization points are generated within the bounding box. These points are called candidate points. The inverse kinematics of the triglide is used to evaluate each candidate point. If the point can be reached with the mobile platform of the triglide, this point is considered a grid point in the true workspace. The final workspace is represented using all the grid points.

It is noted that both the GM and GDM need to discretize the workspace in the z direction. Hence, the discretization step in z is the same for the GM and GDM and it is listed in Table 3-1 and denoted using Δz . Since the steps of the GDM in the other two directions can be the same, the resolution of the GDM

is defined to be the discretization step in x or y direction. In order to compare the accuracy of the computation of workspace volume, the resolution is changed from 10mm to 0.5mm, as shown in Figure 3-8.

A general triglide is used to evaluate the performances of the GM and GDM on solving its workspace. Table 3-1 lists the dimensions of the triglide.

Table 3-1: Dimensions of a triglide and the discretization step in z direction

Parameters	Units	Value
R_a	mm	100
R_b	mm	50
l	mm	100
α	degree	40
Δz	mm	0.5

Figure 3-8 plots the workspace boundary using the GM and the grid points obtained using the GDM on a slicing plane $z = 100mm$ which is in the middle of the entire workspace along the z direction, if the resolution of the GDM is 1mm. The black curves depict the boundary and red stars represent the grid points. It can be seen that all the grid points are located inside the boundary. Figure 3-9 presents the workspace volume obtained using the GM and the GDM. This figure shows that the result obtained using the GDM is closing to that obtained using the GM as the resolution of the GDM is becoming higher. If the resolution increases to 0.5mm, the result obtained using the GDM is nearly equal to that obtained using the GM as shown in Figure 3-9. From Figure 3-8 and Figure 3-9, it can be seen that the GM provides an alternative way for the GDM to obtain the boundary and volume of the workspace of a triglide.

In order to compare the computation cost of the GM and GDM, each method is executed 100 times using MatLab installed on a Dell Optiplex 980 desktop incorporating one 3.2GHz Intel Core i5-650 processor and two 2GB DDR3 SDRAM memory cards. The operating system is 32-bit Windows 7 Enterprise. The average computation time is shown in Figure 3-10. In this figure, the red columns present the computation time of the GDM with different resolutions, and the black columns shows the computation time of the GM. It can be seen that the average computation time of the GM is less than 10 seconds and slightly shorter than the average computation time of the GDM when the resolution is 10mm. If the resolution becomes higher, the computation time of the GDM increases significantly and are much larger than that of the GM. If the resolution is improved to be 0.5mm, the average computation time of the GDM increases to 6203 seconds. From Figure 3-9 and Figure 3-10, it can be stated that higher resolution can make the GDM have higher accuracy but longer computation time. Considering the accuracy and computation load, the GM is a better method to obtain the workspace boundary of a triglide, since it can reach higher accuracy with faster computation.

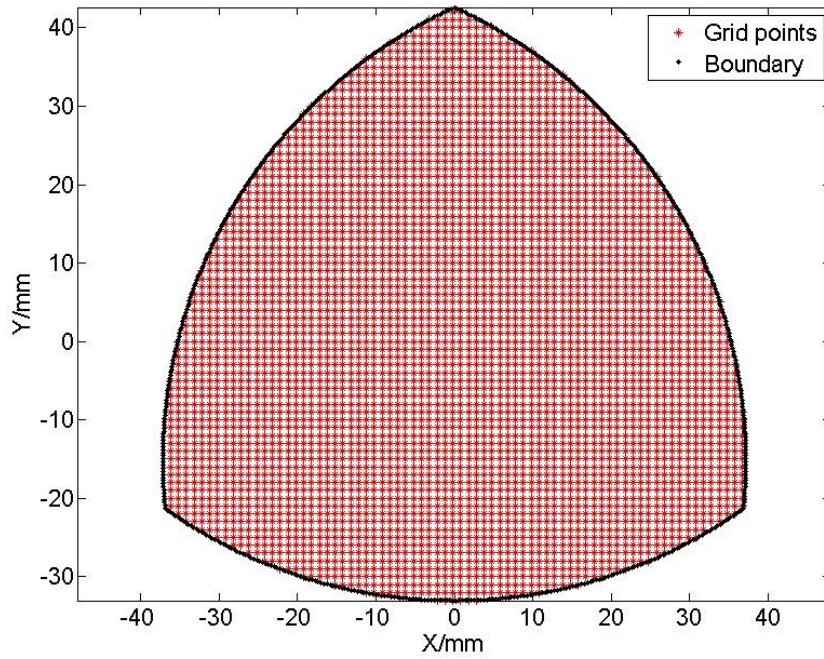


Figure 3-8: The workspace boundary obtained using the GM and the grid points obtained using the GDM on the $z = 100\text{mm}$ plane

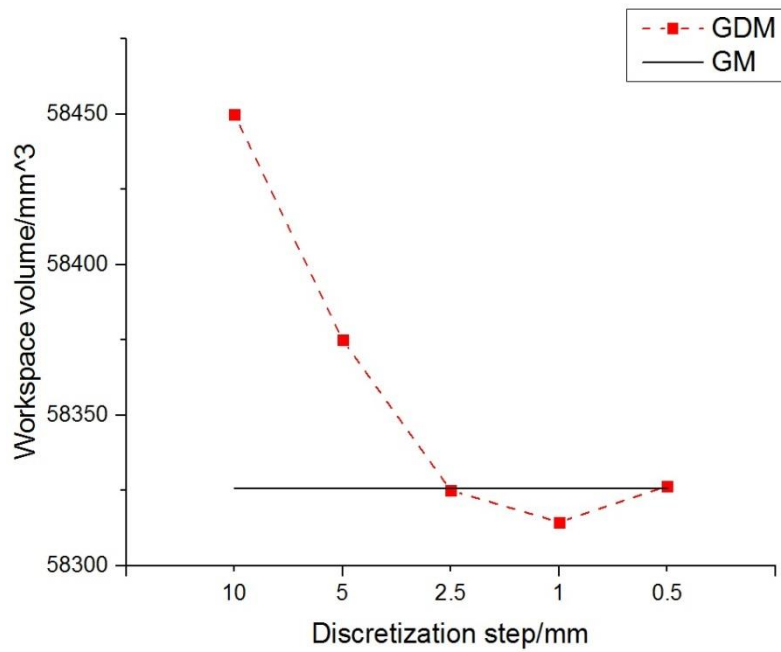


Figure 3-9: The workspace volume obtained using the GM and the GDM

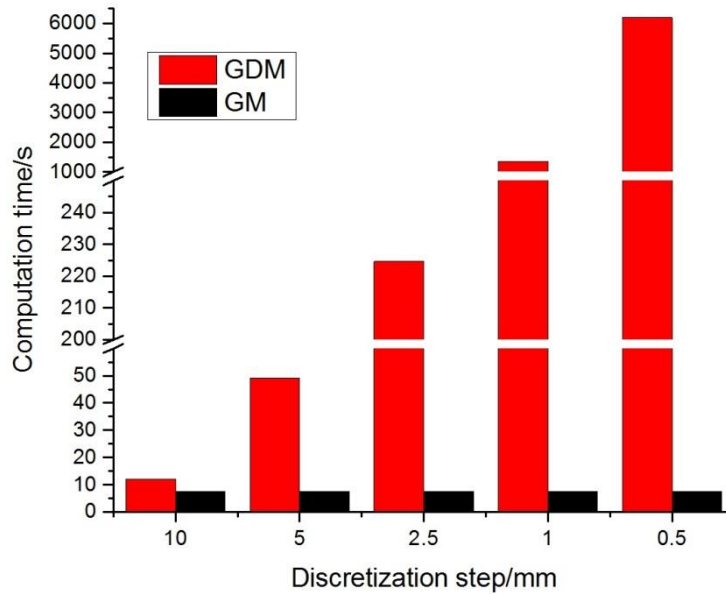


Figure 3-10: The average computation time of the GM and GDM

3.5 Regular workspace

The workspace of a triglide is usually irregular. The irregular workspace increases the complexity for its representation and its application in path planning. Since the workspace of a parallel manipulator is limited, it is common and necessary to check whether the task space is enclosed in its workspace. An irregular workspace can have difficulties to implement the verification of the task space. It can be found that the workspace boundary of a triglide is formed with several arcs. Hence, it is easy to obtain an inscribed circle within the workspace boundary. This section uses this inscribed circle to represent the approximate true workspace on a slicing plane. All the inscribed circles on all the slicing planes are integrated through the z direction to form a regular workspace. This regular workspace will be used in Chapter 5 to guarantee a task space covered by the workspace of an optimized triglide.

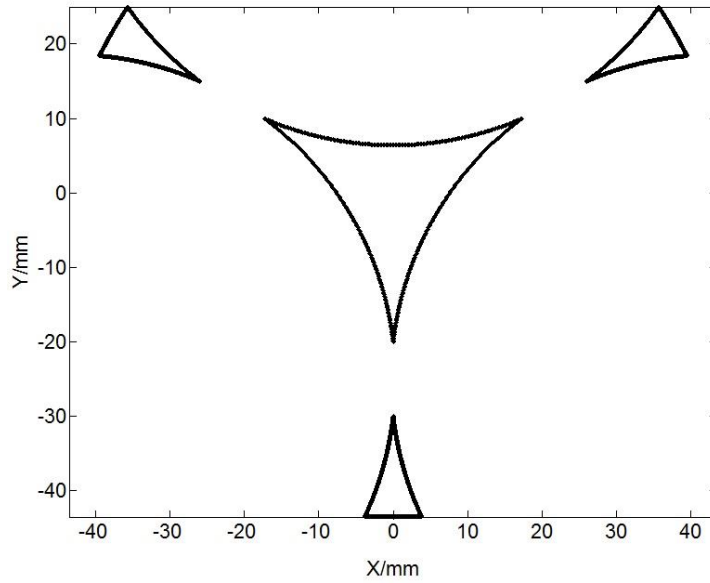


Figure 3-11: The workspace boundary of the triglide obtained using the GM on the slicing plane $z = 90mm$

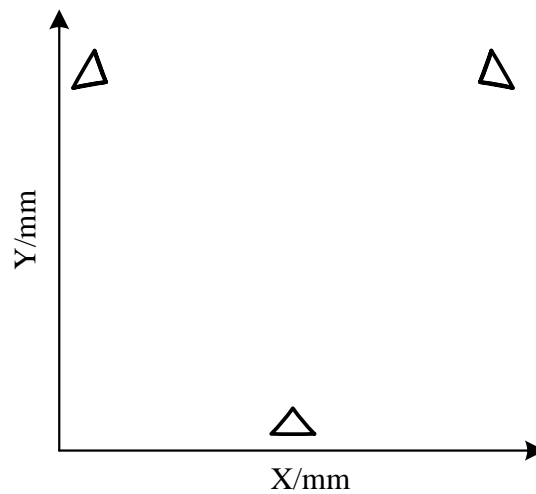


Figure 3-12: The workspace boundary of a triglide on a slicing plane

However, the workspace boundary on some slicing planes has several enclosed areas. Figure 3-11 depicts the workspace boundary of the triglide listed in Table 3-1 on the slicing plane $z = 90mm$. As is shown, this workspace contains four independent enclosed areas. Since it is difficult to represent these four areas with one regular shape, the peripheral areas are ignored and only the central area is considered to obtain its inscribed circle.

Nevertheless, the central area may disappear for some other triglides on some slicing planes. Figure 3-12 depicts a workspace boundary without the central area. In this case, these peripheral areas are ignored and the workspace on the slicing plane is considered to be null to construct the regular workspace, since they are difficult to be represented and are usually quite small.

3.6 Conclusion

Although various 3-DOF pure translational parallel manipulators have been proposed, this chapter chooses a parallel manipulator using parallelogram-type limbs, since such structure has been proved to be able to constrain the orientation of its mobile platform successfully.

This chapter uses a geometrical method to obtain the workspace boundary and the volume of a general triglide. After a comparison with a grid discretization method, it is found that the geometrical method is able to reach higher accuracy with faster computation for obtaining the workspace boundary and volume. Higher resolution can improve the accuracy of the grid discretization method, but cause higher computation load.

Since the workspace of a triglide is usually irregular which causes its difficulty to be applied in path planning, this chapter uses a group of inscribed circles integrated through the z direction to represent the approximate true workspace.

CHAPTER 4 STIFFNESS ANALYSIS OF THE PARALLEL MANIPULATOR

Stiffness analyses of a linear delta and orthoglide have been reported by several researchers, but a general algebraic expression is still needed to obtain the stiffness of a triglide. More importantly, the reported algebraic methods have generally ignored the deformation of the mobile platform. To address this issue, this chapter uses a strain energy method considering the compliance of the mobile platform, and the limbs and the actuators of a triglide. In this method, the deformation of the mobile platform is integrated in the total deformation of the triglide.

A stiffness matrix can always be derived from the stiffness analysis. In the optimization stage, the stiffness matrix is required to be converted to a stiffness index to evaluate the stiffness quality of a parallel manipulator. Generally, the maximum or minimum eigenvalue of the stiffness matrix is used as the stiffness index [106–108], since the maximum and minimum eigenvalues present the greatest and least rigid values in the directions specified by the corresponding eigenvectors. It should be noted that the maximum and minimum eigenvalues are used to define upper and lower bounds of the stiffness. They should be evaluated together and cannot be combined to form a single index. Besides the eigenvalues, the Euclidean norm of the diagonal elements of the stiffness matrix [26], the condition number of the stiffness matrix [83], and the determinant of the stiffness matrix [108] can be accepted as stiffness indices. Since the translation and orientation of a

parallel manipulator have different units, these indices cannot be interpreted easily. Additionally, these stiffness indices fail to relate the stiffness property of a parallel manipulator to the direction of a wrench applied on it. This relationship is important as a parallel manipulator presents different stiffness properties in different directions. A stiffness index, which can be interpreted easily, is used to evaluate the stiffness property of a triglide in this chapter. The stiffness index measures the stiffness property of the triglide along the direction of the wrench applied on the mobile platform during an operation.

4.1 Stiffness analysis using strain energy method

The overall stiffness matrix \mathbf{K} of a triglide is the mapping between the applied external wrench \mathbf{W} and the infinitesimal twist $\delta\xi$ of the central point of its mobile platform. The wrench \mathbf{W} contains forces \mathbf{F} and moments \mathbf{M} , $\mathbf{W} = [\mathbf{F} \quad \mathbf{M}]^T$. Both \mathbf{F} and \mathbf{M} are 1×3 row vector. The twist $\delta\xi$, which is a 6×1 column vector, contains infinitesimal translation $\delta\chi$ and infinitesimal rotation $\delta\psi$. This mapping can be expressed as Equation (4-1), where \mathbf{K} is a 6×6 matrix.

$$\mathbf{W} = \mathbf{K}\delta\xi \quad (4-1)$$

According to Castigliano's second theorem, the infinitesimal twist of an elastic structure is the partial derivative of the strain energy U of the structure with respect to the applied external wrench, given as Equation (4-2) if W_i denotes the i th entry of \mathbf{W} .

$$\delta\xi = \frac{\partial U}{\partial \mathbf{W}} = \left[\frac{\partial U}{\partial W_1} \quad \frac{\partial U}{\partial W_2} \quad \frac{\partial U}{\partial W_3} \quad \frac{\partial U}{\partial W_4} \quad \frac{\partial U}{\partial W_5} \quad \frac{\partial U}{\partial W_6} \right]^T \quad (4-2)$$

If the relationship in Equation (4-3) can be found, where \mathbf{C} is the overall compliance matrix, the stiffness matrix can be obtained as Equation (4-4).

$$\frac{\partial U}{\partial \mathbf{W}} = \mathbf{C}\mathbf{W} \quad (4-3)$$

$$\mathbf{K} = \mathbf{C}^{-1} \quad (4-4)$$

To obtain the compliance matrix \mathbf{C} , the total strain energy of a triglide should be solved. This study assumes that the mobile platform, the parallelogram-type limbs and the actuators are flexible, while the other components are infinitely rigid. The strain energy of the mobile platform, the limbs and the actuators are solved respectively and summed to obtain the total strain energy.

4.1.1 Inverse compliant Jacobian matrix

Assuming that the mobile platform experiences an external wrench \mathbf{W} , defined in the global coordinate frame $\{O\}$ as shown in Figure 4-1, the relation between reaction forces and the applied external wrench \mathbf{W} may be written as Equation (4-5).

$$\begin{cases} \sum_{i=1}^3 (f_{i1} + f_{i2})\mathbf{l}_i + \mathbf{F} = 0 \\ \sum_{i=1}^3 [f_{i1}(\mathbf{b}'_{i1} \times \mathbf{l}_i) + f_{i2}(\mathbf{b}'_{i2} \times \mathbf{l}_i)] + \mathbf{M} = 0 \end{cases} \quad (4-5)$$

In Equation (4-5), f_{ij} denotes the reaction force exerted at the end of the side shaft of the parallelogram limb, \mathbf{l}_i denotes the unit vector of the i th limb, and \mathbf{b}'_{i1} and \mathbf{b}'_{i2} denote the vectors $O'B_{i1}$ and $O'B_{i2}$.

If $\mathbf{f} = [f_{11} \ f_{12} \ f_{21} \ f_{22} \ f_{31} \ f_{32}]^T$, and

$$\mathbf{A}^* = \begin{bmatrix} \mathbf{l}_1 & \mathbf{l}_2 & \mathbf{l}_3 & \mathbf{l}_1 & \mathbf{l}_2 & \mathbf{l}_3 \\ \mathbf{b}'_{11} \times \mathbf{l}_1 & \mathbf{b}'_{12} \times \mathbf{l}_1 & \mathbf{b}'_{21} \times \mathbf{l}_2 & \mathbf{b}'_{22} \times \mathbf{l}_2 & \mathbf{b}'_{31} \times \mathbf{l}_3 & \mathbf{b}'_{32} \times \mathbf{l}_3 \end{bmatrix}$$

Equation (4-6) can be obtained from Equation (4-5), where \mathbf{A} is the inverse of the matrix \mathbf{A}^* and termed inverse compliant Jacobian matrix.

$$\mathbf{f} = \mathbf{A}\mathbf{W} \quad (4-6)$$

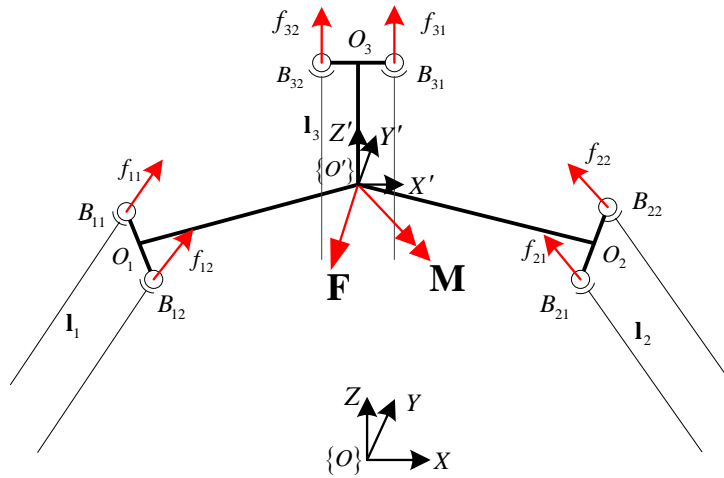


Figure 4-1: The applied external wrench and reaction forces on the mobile platform

4.1.2 Strain energy of the mobile platform

The internal forces and moments experienced by an arbitrary cross section of the mobile platform are depicted in Figure 4-2, and Figure 4-3 depicts the local coordinate system attached to the cross section. The z axis is

perpendicular to the mobile platform and the x axis is parallel to the shaft $B_{i2}B_{i1}$. As shown in Figure 4-2, the cross section experiences an axial force f_{iy} and two shear forces f_{ix} and f_{iz} , given below.

$$\begin{cases} f_{ix} = (f_{i1} + f_{i2})\mathbf{l}_i \cdot \mathbf{b}_{i1} \\ f_{iy} = (f_{i1} + f_{i2})\mathbf{l}_i \cdot \mathbf{q}_i \\ f_{iz} = (f_{i1} + f_{i2})\mathbf{l}_i \cdot (\mathbf{b}_{i1} \times \mathbf{q}_i) \end{cases}$$

The cross section experiences three moments M_{ix} , M_{iz} and τ_i , given below.

$$\begin{cases} M_{ix} = v_i(f_{i1} + f_{i2})\mathbf{l}_i \cdot (\mathbf{b}_{i1} \times \mathbf{q}_i) \\ M_{iz} = (b_{i2}f_{i2} - b_{i1}f_{i1})\mathbf{l}_i \cdot \mathbf{q}_i + v_i(f_{i1} + f_{i2})\mathbf{l}_i \cdot \mathbf{b}_{i1} \\ \tau_i = (b_{i1}f_{i1} - b_{i2}f_{i2})\mathbf{l}_i \cdot (\mathbf{b}_{i1} \times \mathbf{q}_i) \end{cases}$$

In the above expressions, \mathbf{q}_i denotes the unit vector of $O'O_i$, \mathbf{b}_{i1} denotes the unit vector of O_iB_{i1} , b_{i1} and b_{i2} denote the lengths of vectors O_iB_{i1} and O_iB_{i2} , and v_i denotes the distance of the cross section to the connection point between the mobile platform and the limb.

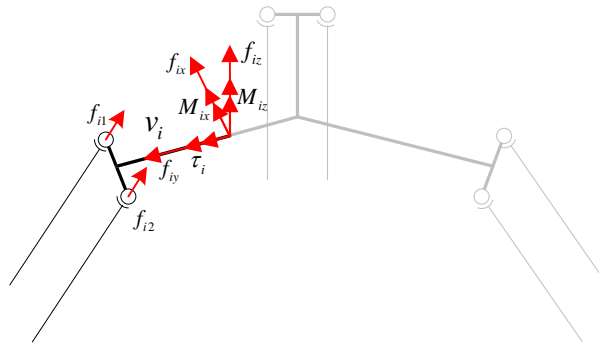


Figure 4-2: Internal forces and moments experienced by a cross section of the mobile platform

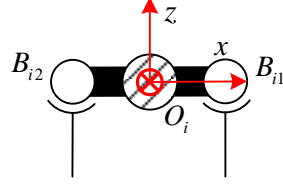


Figure 4-3: Local coordinate system at an arbitrary cross section of the mobile platform

With the internal forces and moments, the strain energy of the mobile platform can be obtained using Equation (4-7).

$$\begin{aligned}
 U_{MP} &= \sum_{i=1}^3 \int_0^{R_i} \left[\frac{M_{ix}^2}{2E_{MP} I_{xx,MP}} + \frac{M_{iz}^2}{2E_{MP} I_{zz,MP}} + \frac{\tau_i^2}{2G_{MP} J_{MP}} + \frac{f_{iy}^2}{2E_{MP} A_{MP}} + \frac{f_{ix}^2}{2G_{MP} A_{x,MP}} + \frac{f_{iz}^2}{2G_{MP} A_{z,MP}} \right] dv_i \\
 &= \sum_{i=1}^3 \mu_{MP1,i} f_{i1}^2 + \mu_{MP2,i} f_{i1} f_{i2} + \mu_{MP3,i} f_{i2}^2
 \end{aligned} \quad (4-7)$$

In Equation (4-7), E_{MP} and G_{MP} denote the elastic modulus and the shear modulus of the mobile platform; $I_{xx,MP}$ and $I_{zz,MP}$ denote the area moment of inertia of the cross section about the x and z axes; J_{MP} denotes the polar moment of inertia of the cross section; and A_{MP} denotes the area of the cross section; $A_{x,MP}$ and $A_{z,MP}$ denote the effective shear area of the cross section along the x and z axes. The coefficients $\mu_{MP1,i}$, $\mu_{MP2,i}$ and $\mu_{MP3,i}$ are dependent on the geometrical properties of the cross section and the material properties of the mobile platform.

4.1.3 Strain energy of the parallelogram limb

The parallelogram limb consists of two bottom shafts and two side shafts. The bottom shaft can be separated into two parts from point O_i as shown in Figure

4-4. The internal forces and moments experienced by the part $O_i B_{i1}$ are analyzed first. An arbitrary cross section of $O_i B_{i1}$ experiences one internal axial force and two shear forces f_{iy} and f_{iz} given below.

$$\begin{cases} f_{ix} = f_{i1} \mathbf{l}_i \cdot \mathbf{b}_{i1} \\ f_{iy} = f_{i1} \mathbf{l}_i \cdot \mathbf{q}_i \\ f_{iz} = f_{i1} \mathbf{l}_i \cdot (\mathbf{b}_{i1} \times \mathbf{q}_i) \end{cases}$$

The cross section experiences two internal moments M_{iy} and M_{iz} which are given below.

$$\begin{cases} M_{iy} = v_i f_{i1} \mathbf{l}_i \cdot (\mathbf{b}_{i1} \times \mathbf{q}_i) \\ M_{iz} = v_i f_{i1} \mathbf{l}_i \cdot \mathbf{q}_i \end{cases}$$

where v_i denotes the distance of the cross section to the vertex B_{i1} .

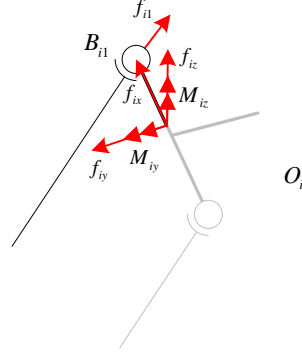
The other part $O_i B_{i2}$ experiences similar internal forces and moments as shown in Figure 4-4(b). The internal axial force and shear forces are

$$\begin{cases} f'_{ix} = f_{i2} \mathbf{l}_i \cdot \mathbf{b}_{i1} \\ f'_{iy} = f_{i2} \mathbf{l}_i \cdot \mathbf{q}_i \\ f'_{iz} = f_{i2} \mathbf{l}_i \cdot (\mathbf{b}_{i1} \times \mathbf{q}_i) \end{cases}$$

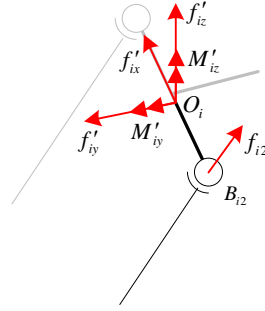
and the internal moments are

$$\begin{cases} M'_{iy} = v_i f_{i2} \mathbf{l}_i \cdot (\mathbf{b}_{i1} \times \mathbf{q}_i) \\ M'_{iz} = v_i f_{i2} \mathbf{l}_i \cdot \mathbf{q}_i \end{cases}$$

where v_i denotes the distance of the cross section to the vertex B_{i2} .



(a) The internal force and moments experienced by $O_i B_{i1}$



(b) The internal force and moments experienced by $O_i B_{i2}$

Figure 4-4: Internal forces and moments exerted in the bottom shaft

Thus, the strain energy of the bottom shafts is given by Equation (4-8), where E_{uPL} and G_{uPL} denote the elastic modulus and shear modulus of the bottom shaft, $I_{yy,uPL}$ and $I_{zz,uPL}$ denote the area moment of inertia about the y and z axes, $A_{y,uPL}$ and $A_{z,uPL}$ denote the effective area along the y and z axes, and $A_{uPL,i}$ denotes the area of the cross section.

$$\begin{aligned}
 U_{ES} = & \sum_{i=1}^3 \int_0^{b_{i1}} \left(\frac{M_{iy}^2}{E_{uPL} I_{yy,uPL}} + \frac{M_{iz}^2}{E_{uPL} I_{zz,uPL}} + \frac{f_{ix}^2}{E_{uPL} A_{uPL}} + \frac{f_{iy}^2}{G_{uPL} A_{y,uPL}} + \frac{f_{iz}^2}{G_{uPL} A_{z,uPL}} \right) dv_i \\
 & + \sum_{i=1}^3 \int_0^{b_{i2}} \left(\frac{M'_{iy}^2}{E_{uPL} I_{yy,uPL}} + \frac{M'_{iz}^2}{E_{uPL} I_{zz,uPL}} + \frac{f'_{ix}{}^2}{E_{uPL} A_{uPL}} + \frac{f'_{iy}{}^2}{G_{uPL} A_{y,uPL}} + \frac{f'_{iz}{}^2}{G_{uPL} A_{z,uPL}} \right) dv_i
 \end{aligned} \quad (4-8)$$

The side shaft experiences only axial force as shown in Figure 4-4. Hence, the strain energy of the side shafts is given by Equation (4-9), where $E_{vPL,i}$

denotes the elastic modulus of the side shaft and $A_{vPL,i}$ is the area of the cross section.

$$U_{LS} = \sum_{i=1}^3 \frac{l_i(f_{i1}^2 + f_{i2}^2)}{2E_{vPL,i}A_{vPL,i}} \quad (4-9)$$

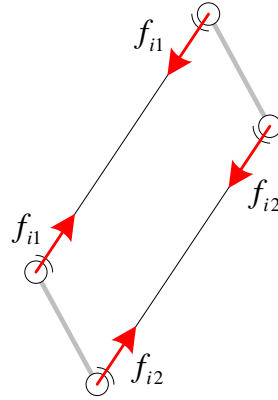


Figure 4-5: The internal force exerted in the side shaft of the limb

The total strain energy of the limb is the sum of the strain energy of the side shafts and the bottom shafts, given by Equation (4-10), where the coefficients $\mu_{PL1,i}$ and $\mu_{PL2,i}$ are dependent on the geometrical properties of the cross section and the material properties of the limb.

$$U_{PL} = U_{ES} + U_{LS} = \sum_{i=1}^3 (\mu_{PL1,i}f_{i1}^2 + \mu_{PL2,i}f_{i2}^2) \quad (4-10)$$

4.1.4 Strain energy of the actuator

If the actuator is translational, the slider and the frame, which constrain the orientations of the slider, are assumed to be infinitely rigid. The internal force and moments experienced by the lead screw is depicted in Figure 4-6. As shown in Figure 4-6, the lead screw experiences an axial force

$$f_{ix} = (f_{i1} + f_{i2})\mathbf{l}_i \cdot \mathbf{d}_i$$

and a torque

$$\tau_i = \frac{f_{ix}P_i}{2\pi} = \frac{P_i(f_{i1} + f_{i2})\mathbf{l}_i \cdot \mathbf{d}_i}{2\pi}$$

where \mathbf{d}_i denotes the unit vector of the lead screw and P_i is the lead of the lead screw.

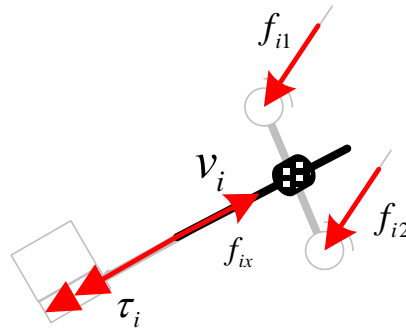


Figure 4-6: The internal force and moment experienced by the lead screw

With the internal force and moments, the strain energy of the lead screw can be obtained using Equation (4-11).

$$\begin{aligned} U_{AS} &= \sum_{i=1}^3 \left(\frac{d_i f_{ix}^2}{2E_{AS,i} A_{AS,i}} + \frac{d_i \tau_i^2}{2G_{AS,i} J_{AS,i}} \right) \\ &= \sum_{i=1}^3 \left(\frac{d_i (\mathbf{l}_i \cdot \mathbf{d}_i)^2 (f_{i1} + f_{i2})^2}{2E_{AS,i} A_{AS,i}} + \frac{d_i P_i^2 (\mathbf{l}_i \cdot \mathbf{d}_i)^2 (f_{i1} + f_{i2})^2}{8\pi^2 G_{AS,i} J_{AS,i}} \right) \end{aligned} \quad (4-11)$$

The motor experiences a torque given below, where N_i denotes the transmission ratio of the gear box in the actuator.

$$\tau_{mi} = \frac{\tau_i}{N_i}$$

If $k_{tor,i}$ is the equivalent torsional stiffness of the motor, the strain energy of the motor is obtained using Equation (4-12).

$$U_{AM} = \sum_{i=1}^3 \frac{\tau_{mi}^2}{2k_{tor,i}} = \sum_{i=1}^3 \frac{P_i^2 l_{di}^2 (f_{i1} + f_{i2})^2}{8\pi^2 N_i^2 k_{tor,i}} \quad (4-12)$$

With Equations (4-11) and (4-12), the total strain energy of the actuators can be obtained using Equation (4-13), where the coefficients $\mu_{Act1,i}$, $\mu_{Act2,i}$ and $\mu_{Act3,i}$ are dependent on the physical properties of the motor and the lead screw of the actuator.

$$U_{Act} = U_{AS} + U_{AM} = \sum_{i=1}^3 \mu_{Act1,i} f_{i1}^2 + \mu_{Act2,i} f_{i1} f_{i2} + \mu_{Act3,i} f_{i2}^2 \quad (4-13)$$

4.1.5 The total strain energy of a triglide

With the formulations given in the previous sections, the total strain energy of a triglide is given by Equation (4-14), where $\mu_{1,i} = \mu_{MP1,i} + \mu_{PL1,i} + \mu_{Act1,i}$, $\mu_{2,i} = \mu_{MP2,i} + \mu_{Act2,i}$ and $\mu_{3,i} = \mu_{MP3,i} + \mu_{PL2,i} + \mu_{Act3,i}$.

$$\begin{aligned} U &= U_{MP} + U_{PL} + U_{Act} \\ &= \sum_{i=1}^3 (\mu_{1,i} f_{i1}^2 + \mu_{2,i} f_{i1} f_{i2} + \mu_{3,i} f_{i2}^2) \end{aligned} \quad (4-14)$$

With infinitesimal translation $\delta\chi = [\delta\chi_x \quad \delta\chi_y \quad \delta\chi_z]^T$ and infinitesimal rotation $\delta\psi = [\delta\psi_x \quad \delta\psi_y \quad \delta\psi_z]^T$, Equation (4-2) will form the following Equation (4-15), where $a_{i,j}$ denotes the element located in the i th row and

j th column of the inverse compliant Jacobian matrix \mathbf{A} , and \mathbf{a}_i denotes the i th row vector of the matrix \mathbf{A} .

$$\left\{ \begin{array}{l} \delta\chi_x = \frac{\partial U}{\partial f_x} = \sum_{i=1}^3 (2\mu_{1,i} a_{2i-1,1} \mathbf{a}_{2i-1} + \mu_{2,i} a_{2i-1,1} \mathbf{a}_{2i} + \mu_{2,i} a_{2i,1} \mathbf{a}_{2i-1} + 2\mu_{3,i} a_{2i,1} \mathbf{a}_{2i}) \mathbf{W} \\ \delta\chi_y = \frac{\partial U}{\partial f_y} = \sum_{i=1}^3 (2\mu_{1,i} a_{2i-1,2} \mathbf{a}_{2i-1} + \mu_{2,i} a_{2i-1,2} \mathbf{a}_{2i} + \mu_{2,i} a_{2i,2} \mathbf{a}_{2i-1} + 2\mu_{3,i} a_{2i,2} \mathbf{a}_{2i}) \mathbf{W} \\ \delta\chi_z = \frac{\partial U}{\partial f_z} = \sum_{i=1}^3 (2\mu_{1,i} a_{2i-1,3} \mathbf{a}_{2i-1} + \mu_{2,i} a_{2i-1,3} \mathbf{a}_{2i} + \mu_{2,i} a_{2i,3} \mathbf{a}_{2i-1} + 2\mu_{3,i} a_{2i,3} \mathbf{a}_{2i}) \mathbf{W} \\ \delta\psi_x = \frac{\partial U}{\partial M_x} = \sum_{i=1}^3 (2\mu_{1,i} a_{2i-1,4} \mathbf{a}_{2i-1} + \mu_{2,i} a_{2i-1,4} \mathbf{a}_{2i} + \mu_{2,i} a_{2i,4} \mathbf{a}_{2i-1} + 2\mu_{3,i} a_{2i,4} \mathbf{a}_{2i}) \mathbf{W} \\ \delta\psi_y = \frac{\partial U}{\partial M_y} = \sum_{i=1}^3 (2\mu_{1,i} a_{2i-1,5} \mathbf{a}_{2i-1} + \mu_{2,i} a_{2i-1,5} \mathbf{a}_{2i} + \mu_{2,i} a_{2i,5} \mathbf{a}_{2i-1} + 2\mu_{3,i} a_{2i,5} \mathbf{a}_{2i}) \mathbf{W} \\ \delta\psi_z = \frac{\partial U}{\partial M_z} = \sum_{i=1}^3 (2\mu_{1,i} a_{2i-1,6} \mathbf{a}_{2i-1} + \mu_{2,i} a_{2i-1,6} \mathbf{a}_{2i} + \mu_{2,i} a_{2i,6} \mathbf{a}_{2i-1} + 2\mu_{3,i} a_{2i,6} \mathbf{a}_{2i}) \mathbf{W} \end{array} \right. \quad (4-15)$$

With Equation (4-3), Equation (4-16) can be obtained.

$$\mathbf{C} = \left[\begin{array}{l} \sum_{i=1}^3 (2\mu_{1,i} a_{2i-1,1} \mathbf{a}_{2i-1} + \mu_{2,i} a_{2i-1,1} \mathbf{a}_{2i} + \mu_{2,i} a_{2i,1} \mathbf{a}_{2i-1} + 2\mu_{3,i} a_{2i,1} \mathbf{a}_{2i}) \\ \sum_{i=1}^3 (2\mu_{1,i} a_{2i-1,2} \mathbf{a}_{2i-1} + \mu_{2,i} a_{2i-1,2} \mathbf{a}_{2i} + \mu_{2,i} a_{2i,2} \mathbf{a}_{2i-1} + 2\mu_{3,i} a_{2i,2} \mathbf{a}_{2i}) \\ \sum_{i=1}^3 (2\mu_{1,i} a_{2i-1,3} \mathbf{a}_{2i-1} + \mu_{2,i} a_{2i-1,3} \mathbf{a}_{2i} + \mu_{2,i} a_{2i,3} \mathbf{a}_{2i-1} + 2\mu_{3,i} a_{2i,3} \mathbf{a}_{2i}) \\ \sum_{i=1}^3 (2\mu_{1,i} a_{2i-1,4} \mathbf{a}_{2i-1} + \mu_{2,i} a_{2i-1,4} \mathbf{a}_{2i} + \mu_{2,i} a_{2i,4} \mathbf{a}_{2i-1} + 2\mu_{3,i} a_{2i,4} \mathbf{a}_{2i}) \\ \sum_{i=1}^3 (2\mu_{1,i} a_{2i-1,5} \mathbf{a}_{2i-1} + \mu_{2,i} a_{2i-1,5} \mathbf{a}_{2i} + \mu_{2,i} a_{2i,5} \mathbf{a}_{2i-1} + 2\mu_{3,i} a_{2i,5} \mathbf{a}_{2i}) \\ \sum_{i=1}^3 (2\mu_{1,i} a_{2i-1,6} \mathbf{a}_{2i-1} + \mu_{2,i} a_{2i-1,6} \mathbf{a}_{2i} + \mu_{2,i} a_{2i,6} \mathbf{a}_{2i-1} + 2\mu_{3,i} a_{2i,6} \mathbf{a}_{2i}) \end{array} \right] \quad (4-16)$$

After obtaining the total compliant matrix \mathbf{C} , the total stiffness matrix \mathbf{K} can be obtained easily using Equation (4-4).

4.2 Comparison with FEA method

With appropriate settings, modelling and meshing, FEA methods are able to obtain accurate results. Since the FEA methods have been adopted by many researchers to evaluate their analytical results, an FEA model is built in this study to evaluate and compare with the proposed algebraic analysis. In this evaluation, the geometrical and material properties of the triglide are listed in Table 4-1. It should be noted that the cross sections of all the analyzed components of the triglide are of the same solid circular shape, and the materials of all the components are the same. The limbs of the triglide are identical and the actuators are distributed symmetrically.

Besides the physical properties of the triglide, it is necessary to provide the configuration of the triglide, since stiffness is a local property and is dependent on the configuration. It is time-consuming and difficult to analyze the stiffness of all the configurations within the entire workspace. The configurations of the PTPM can be categorised into two groups based on whether the PTPM is rotational symmetric. Hence, this study selects a rotational symmetric configuration, in which the actuators have the same displacement, and an asymmetric configuration, in which the actuators have different displacements. In the symmetric configuration, two different wrenches are applied at the centre of the mobile platform. The first wrench is a force along the z direction in which the PTPM is assumed to be stiffest and the second one includes random forces and moments. In the asymmetric configuration, the PTPM experiences a general wrench. Table 4-2 lists these configurations and the applied wrenches.

Table 4-1: The physical properties of an analyzed triglide

Parameters	Units	Value
R_a	mm	10
R_b	mm	5
l	mm	10
n	mm	6
α	degree	40
A	mm ²	3.1416
E	GPa	210
G	GPa	80
N		5
P	mm	3
k_{tor}	N·m/rad	3×10^5

Table 4-2: The configurations of the triglide and the applied wrenches on the triglide

Parameters	Units	Configuration 1	Configuration 2	Configuration 3
Actuator 1	mm	1	1	1
Actuator 2	mm	1	1	2
Actuator 3	mm	1	1	3
Force F_x	N	0	19	46
Force F_y	N	0	-18	-1
Force F_z	N	-100	45	30
Moment M_x	N·m	0	-46	-36
Moment M_y	N·m	0	-6	-8
Moment M_z	N·m	0	-12	42

A commercial FEA software, Abaqus (Dassault Systèmes), is used to model the triglide. The actuators of the triglide are modelled using spring elements. Beam elements are used to model the mobile platform and the limbs of the triglide. All the passive joints are assumed to be non-deformable. Table 4-3 lists the deformation of the central point of the mobile platform obtained using the FEA method and the algebraic method. Table 4-3 shows that displacements less than 1.0×10^{-6} mm and orientations less than 1.0×10^{-6}

radian are much smaller than the other values. These values can be attributed to computation errors. Therefore, values less than 1.0×10^{-6} are not used to compute the relative errors between the results obtained using the algebraic and FEA methods.

From Table 4-3, it can be seen that the differences between the results from the FEA and algebraic methods are not obvious. The maximum relative error is less than 10%. With this comparison, it can be stated that the algebraic method can be chosen as an alternative to the FEA method in the pre-design stage, especially in optimization design.

Table 4-3: The deformation of the central point of the mobile platform

Configuration	Method	δx	δy	δz	δM_x	δM_y	δM_z
		mm	mm	mm	radian	radian	radian
1	Algebraic	-4.3×10^{-17}	2.0×10^{-17}	-0.0148	6.1×10^{-19}	3.7×10^{-18}	-1.4×10^{-18}
	FEA	-3.0×10^{-7}	1.8×10^{-7}	-0.0141	6.1×10^{-8}	1.5×10^{-10}	-3.3×10^{-10}
	Relative error			4.73%			
2	Algebraic	0.1196	-0.1314	-0.0067	-0.0100	-0.0088	-0.0012
	FEA	0.1093	-0.1198	-0.0063	-0.0091	-0.0080	-0.0011
	Relative error	8.61%	8.83%	5.79%	9%	9.09%	8.33%
3	Algebraic	0.3058	-0.0126	-0.0790	-0.0018	-0.0190	0.0043
	FEA	0.2770	-0.0121	-0.0716	-0.0017	-0.0172	0.0039
	Relative error	9.42%	3.97%	9.37%	5.56%	9.47%	9.30%

4.3 Stiffness index

This study proposes a new stiffness index, which measures the inverse of the virtual work completed by a unit wrench, to evaluate the stiffness of a triglide.

This stiffness index can be termed the virtual work (VW) stiffness index.

Supposing a unit wrench \mathbf{W} is applied on the mobile platform of a triglide, the virtual work completed by the wrench is given by Equation (4-17).

$$W_v = \mathbf{W}^T \delta \xi \quad (4-17)$$

Since the infinitesimal twist $\delta \xi = \mathbf{K}^{-1} \mathbf{W}$, the VW stiffness index is given by Equation (4-18).

$$\kappa_v = \frac{1}{\mathbf{W}^T \mathbf{K}^{-1} \mathbf{W}} \quad (4-18)$$

With the VW stiffness index, the stiffness matrix is converted into a single value. This value measures the resistance of a triglide to deformation under a given wrench. It should be noted that the virtual work completed by the forces and moments of the wrench \mathbf{W} must have the same unit in order to compute the VW stiffness index. The unit wrench used in Equation (4-18) is required to satisfy $\|\mathbf{W}\| = 1$.

The VW index is used as a local presentation of the stiffness property of the triglide defined in Table 4-1. The workspace of a PTPM is plotted in Figure 4-7. The workspace is discretized into points with an interval of 0.25mm along the x , y and z directions. The workspace in the plane of $z = 10$ mm, which is in the middle of the entire workspace along the z direction, is selected to evaluate the VW index of the PTPM. In this plane, the configurations of the PTPM include the general configurations and a rotational symmetric configuration, in which the mobile platform is located at the centre of the plane. If the unit of the virtual work is unified to be 0.001 joule and the wrench $\mathbf{W} = [0 \ 0 \ 1 \ 0 \ 0 \ 0]^T$, the distributions of the index in the plane

of $z = 10\text{ mm}$ are illustrated in Figure 4-8. It can be seen that the VW index is higher and increases sharply as the mobile platform is closer to the center of the workspace. The boundary of the workspace has the lowest value of the VW index. With the same applied wrench, the index measures the resistance to deformation. Thus, it can be stated that the triglide is the stiffest at the central position if the applied wrench is a force along the z direction, and its stiffness becomes lower if the mobile platform is closer to the boundary of the workspace.

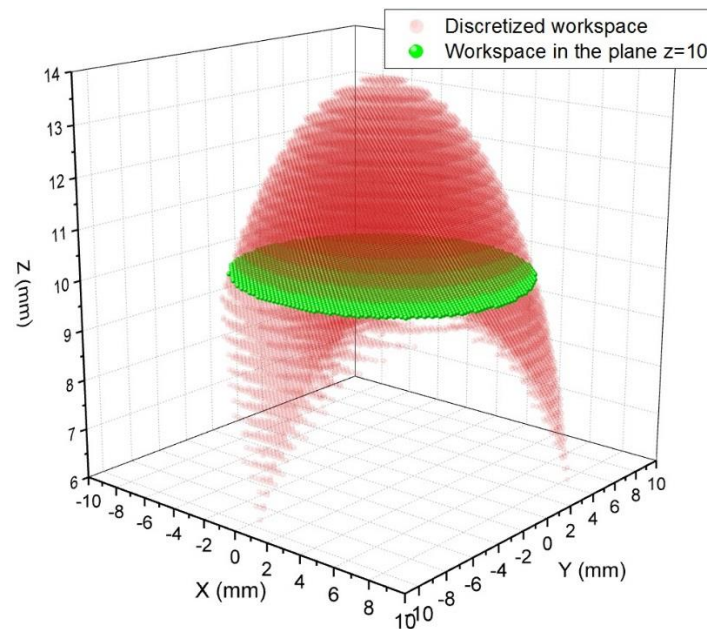


Figure 4-7: The discretized workspace of a PTPM and its workspace in the plane of $z = 10\text{ mm}$

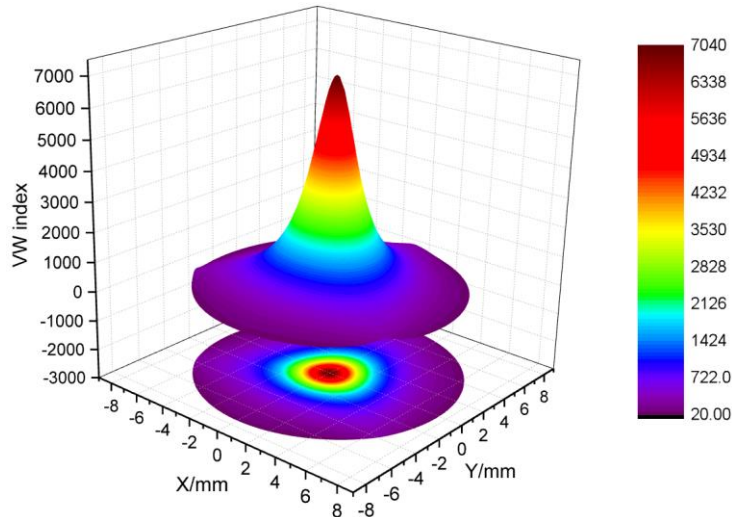
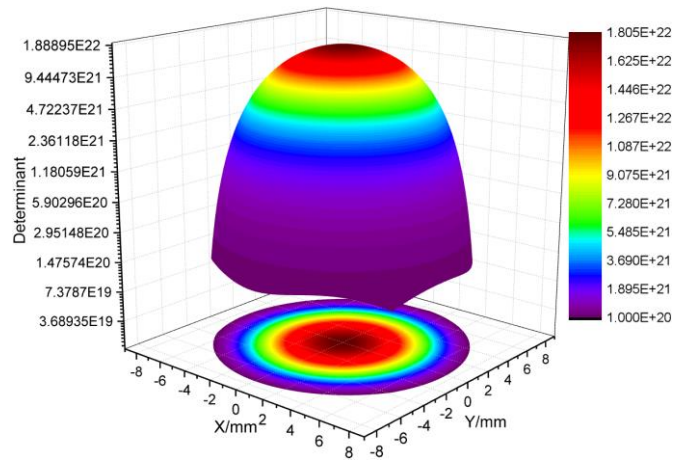


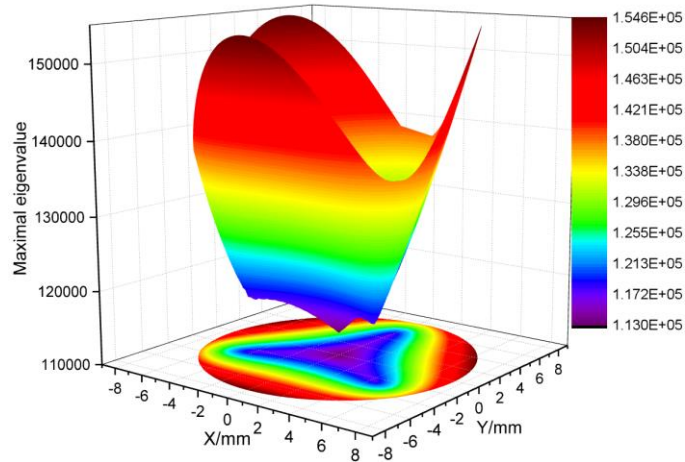
Figure 4-8: The distribution of the VW index of the triglide in the plane of $z = 10\text{ mm}$ when a unit wrench is applied

The VW index is compared with two other indices, which are the determinant and the eigenvalues of the stiffness matrix. The determinant index uses a single value to evaluate the stiffness of a parallel manipulator, while the eigenvalues use the maximum and minimum values to define a boundary of the stiffness. Figure 4-9(a) plots the distributions of the determinant index in the plane of $z = 10\text{ mm}$, and the distributions of maximum and minimum eigenvalues in the plane of $z = 10\text{ mm}$ are depicted in Figure 4-9(b) and Figure 4-9(c). Similar to the VW index, the triglide has the largest determinant and minimal eigenvalues at the center of the workspace, and they become smaller farther away from the center as presented in Figure 4-9(a) and Figure 4-9(c). However, the maximum eigenvalue becomes smaller closer to the center and it is the largest at the boundary as shown in Figure 4-9(b). This phenomenon illustrates that the triglide is stiffest at the boundary with an applied wrench in the direction specified by the eigenvector corresponding to the maximal eigenvalue, while it is the most deformable at the boundary if the applied wrench has the same direction with the eigenvector corresponding to the

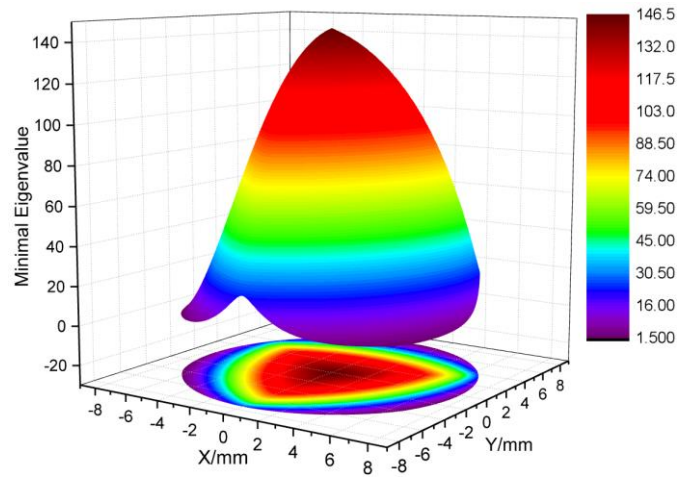
minimal eigenvalue. The wrenches from different directions cause the triglide to behave differently. Unfortunately, the determinant and the eigenvalues fail to relate the stiffness property with the direction of the applied wrench on the triglide.



(a)



(b)



(c)

Figure 4-9: The distributions of the (a) determinant, (b) maximal and (c) minimal eigenvalues of the stiffness matrix in the plane of $z = 10$ mm

If a unit wrench $\mathbf{W} = [0.4082 \ 0.4082 \ 0.4082 \ 0.4082 \ 0.4082 \ 0.4082]^T$ is applied on the triglide, Figure 4-10 depicts the distributions of the VW index in the plane of $z = 10$ mm. From Figure 4-10, it can be seen that the distributions are different from that depicted in Figure 4-8. The triglide is not the stiffest when its mobile platform is at the central position. The stiffest position is located between the center and the boundary of the workspace. Although the triglide with its mobile platform at a boundary position still behaves to be more deformable, the triglide becomes stiffer when the boundary position is nearer to the stiffest position. The comparison between Figure 4-8 and Figure 4-10 shows that the stiffness properties are very different in different directions. It is necessary to relate the value of a stiffness index to the direction of the wrench experienced by the manipulator.

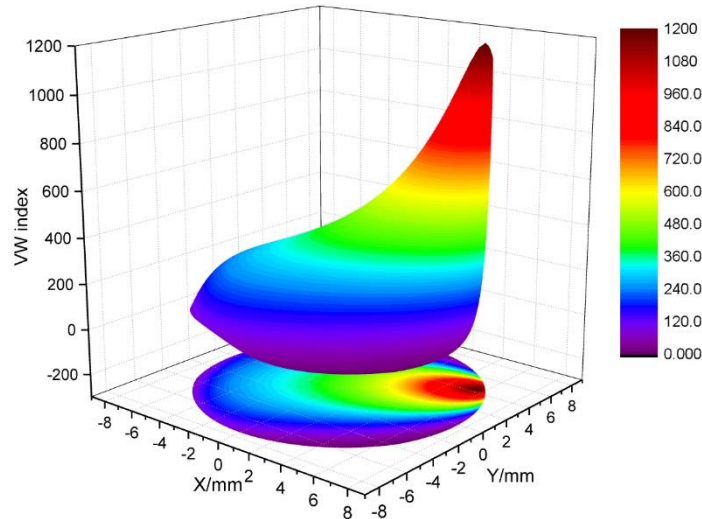


Figure 4-10: The distribution of the VW index of the triglide in the plane of $z = 10\text{mm}$ when a different unit wrench is applied

It should be noted that elementary arithmetic operation of translation and orientation is interpreted differently, since the units of translation and orientation are different. However, this operation is common to compute several stiffness indices. Compared with the determinant and the eigenvalue indices, the VW index uses virtual work to avoid the problem caused by the different units of translation and orientation and relates the index value to the direction of the wrench applied on the manipulator. With the VW index, the stiffness of a parallel manipulator can be optimized by changing its structural configuration and dimension when the wrench applied on the mobile platform is known for a specified task. In addition, the VW index can be used to find the direction in which the manipulator is stiffest in the entire workspace when its structure and dimension are known.

4.4 Conclusion

Based on Castigliano's second theorem, this study uses the strain energy method to deduce an algebraic expression for the stiffness of a general triglide.

In the proposed method, the deformations of the mobile platform, the limbs and the actuators of the triglide are considered, while the other components are assumed to be infinitely rigid. With this algebraic expression, the stiffness matrix can be obtained easily even when the configuration or the dimension of the PTPM has been changed. After a comparison with an FEA method, it is found that the relative error between the algebraic method and the FEA method is lower than 10%. The algebraic method can be considered to be an alternative of the FEA method and is suitable to be used in the pre-design stage, especially in design optimization as it requires less computation.

To evaluate the stiffness of a triglide, a new stiffness index is proposed to measure the resistance of a parallel manipulator to deformation with an applied wrench. Compared with other stiffness indices, this index uses virtual work to avoid interpretation difficulty caused by different units of translation and orientation, and relates the index value to the direction of the wrench experienced by the manipulator during an operation. This index can be used to optimize the structure or plan the trajectory of a parallel manipulator to achieve high stiffness.

CHAPTER 5 OPTIMIZATION OF THE PARALLEL MANIPULATOR

Although the performance analysis of a parallel manipulator is complicated, it is believed that a good optimization design approach is able to bring significant improvements of its performance. Optimization design of a parallel manipulator has attracted much interest from researchers. The optimization of a linear delta and an Orthoglide has been presented in [30, 110, 111]. However, the optimization of a general triglide has not been reported. This chapter proposes a method aiming to provide the optimization of a general triglide considering its dexterity, stiffness and ratio of dimensional volume to workspace.

Stiffness optimization has been addressed by many researchers, as in the case of a linear delta [28], a 5-DOF tripod [112], and a 3-DOF parallel manipulator [113], while they only considered the compliance of actuators and have ignored the compliance of limbs, mobile platforms of the manipulators. Since the ignored compliance has significant effects on the static stiffness of a parallel manipulator, this chapter includes the compliance of actuators, limbs and the mobile platform into the optimization study.

The ratio of workspace to dimensional volume of a parallel manipulator was developed by Miller [114] to measure the factor of space utilization. The dimensional volume of the parallel manipulator is represented with a bounding box, which is defined to be a minimum prism containing all the actuators and

positions within its workspace. This ratio was also adopted by Liu [28] to optimize a linear delta. Liu used a cylinder enclosing the structure of the robot to represent its dimensional volume. These representations are easy to obtain a constant value of the space utilization of a parallel manipulator. However, the space utilization changes during the movement of the mobile platform, but the variable utilization is ignored by these researchers. This chapter uses a constant volume to obtain the basic space utilization of a parallel manipulator and an average variable volume to represent the variable utilization due to movement.

This chapter first introduces three performance criteria to measure dexterity, stiffness and ratio of workspace to dimensional volume, followed with the possible constraints posed in the optimization. After the description of the constraints, the optimization results using the proposed method are compared with a reported optimal solution of a parallel manipulator, which has a similar structure as the triglide, and conclusions are drawn.

5.1 Performance measures

5.1.1 Dexterity

Singularity avoidance is one important requirement of a parallel manipulator during an operation, since its controllability is lost in a singular configuration. A parallel manipulator can have three kinds of kinematic singularities, which are forward kinematic singularity, inverse kinematic singularity and a combination of the previous two singularities. In order to assess singularity avoidance and position accuracy, several performance criteria have been used

by the researchers, such as the condition number or the minimum singular value of kinematic Jacobian matrix, and the manipulability [115]. The global dexterity was defined by Altuzarra et al [32] to be an average distribution of the condition number of the kinematic Jacobian matrix on a given trajectory. Before Altuzarra et al, the global dexterity was calculated by Rao et al [29] and Abbasnejad et al [116] using the average distribution of the condition number over the workspace of a parallel manipulator. This calculation was also used by Stock and Miller [117] to measure the manipulability of a parallel manipulator. Actually, the average distribution of the condition number was first proposed by Gosselin and Angeles as the global conditioning index [79] to measure the error amplification between the joints and the Cartesian spaces. This index has been widely used by many researchers [24, 28, 80, 81] as a criterion of kinematic performance. Hence, this chapter uses a similar index used by Abbasnejad et al [116] to measure the global dexterity of a general triglide.

Before the calculation of the global dexterity index (GDI), it is necessary to obtain the kinematic Jacobian matrix first. The structure of a general triglide is depicted in Figure 3-1. For more information about a general triglide, it is suggested to refer to Chapter 3. The Jacobian matrix can be obtained using the method proposed by Tsai and Joshi [25]. If \mathbf{t}_i denotes the unit vector of $\mathbf{B}_i\mathbf{C}_i$, $\dot{\mathbf{x}}$ and \dot{q}_i denote respectively the velocity of the mobile platform and the i th actuator, and \mathbf{s}_i is the unit vector of $\mathbf{A}_i\mathbf{C}_i$, Equation (5-1) can be obtained.

$$\mathbf{t}_i^T \dot{\mathbf{x}} = \mathbf{t}_i^T \mathbf{s}_i \dot{q}_i \quad (5-1)$$

Thus, the forward kinematic Jacobian matrix is obtained using Equation (5-2).

$$\mathbf{J}_q = \begin{bmatrix} \mathbf{t}_1^T \mathbf{s}_1 & & \\ & \mathbf{t}_2^T \mathbf{s}_2 & \\ & & \mathbf{t}_3^T \mathbf{s}_3 \end{bmatrix} \quad (5-2)$$

The inverse kinematic Jacobian matrix is obtained using Equation (5-3).

$$\mathbf{J}_x = [\mathbf{t}_1 \quad \mathbf{t}_2 \quad \mathbf{t}_3]^T \quad (5-3)$$

Both \mathbf{J}_q and \mathbf{J}_x are 3×3 matrices. Therefore, the Jacobian matrix is

$$\mathbf{J} = \mathbf{J}_x^{-1} \mathbf{J}_q \quad (5-4)$$

The GDI can be calculated using Equation (5-5).

$$\eta = \frac{\int_W \frac{1}{\kappa} dW}{\int_W dW} \quad (5-5)$$

where κ is the condition number of the Jacobian matrix, which can be obtained using $\kappa = \|J^{-1}\| \|J\|$, and W is the entire workspace of the parallel manipulator.

Since κ tends to infinity at singularities, and is equal to 1 at isotropic positions, the global dexterity index is within the interval $[0,1]$ and larger value of η gives better dexterity of the triglide.

5.1.2 Stiffness

As described in Chapter 4, the strain energy method is used to obtain the stiffness matrix of the triglide considering the compliances of its mobile platform, limbs and translational actuators. As discussed in Chapter 4, the VW stiffness index is able to avoid the problem caused by different units of translation and orientation and relates the index value to the direction of the wrench applied on the manipulator. This index is used to evaluate the stiffness behavior. Larger index can make the manipulator more difficult to be deformed.

It should be noted that the VW index presents local stiffness property. Its value is dependent on the configuration of the triglide. The GSI can be obtained using Equation (5-6).

$$\eta_{\kappa} = \frac{\int_W \kappa_V dW}{\int_W dW} \quad (5-6)$$

where κ_V is the VW index and can be obtained using Equation (4-18).

5.1.3 Space utilization

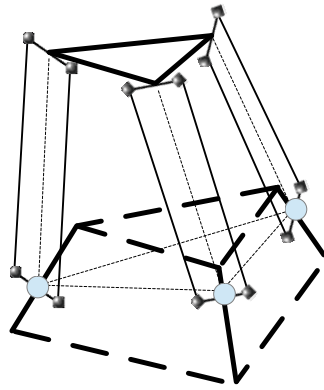
As described in Chapter 3, the workspace volume can be obtained using the geometrical method, which is fast and accurate. The workspace volume can be denoted as V . Since the triglide is a 3-identical-leg parallel mechanism, the volume of the triangular prism is used to represent the dimensions of the triglide. The volume can be separated into a constant size and a variable size as shown in Figure 5-1. The volume of the constant prism P_1 remains the

same, while the volume of the variable prism P_2 depends on the postures of the triglide. If the volume of P_1 is denoted by V_1 , it can be obtained using Equation (5-7), in which s_d is the full stroke distance of the actuator.

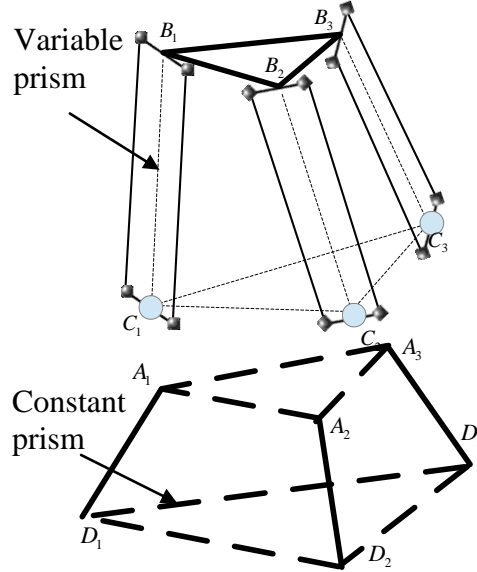
$$V_1 = \frac{\sqrt{3}}{4} (3R_a^2 s_d \sin \alpha + 3R_a s_d^2 \sin \alpha \cos \alpha + s_d^3 \sin \alpha \cos^2 \alpha) \quad (5-7)$$

However, the variable prism P_2 is not always a normal prism, since any two instances of B_1C_1 , B_2C_2 and B_3C_3 are not always coplanar. If V_2 denotes the volume of P_2 , then it can be computed as the sum of the volumes of three triangular pyramids $B_1-C_1C_2C_3$, $C_2-B_1B_2B_3$ and $B_1-B_3C_2C_3$. Since V_2 changes due to the movement of the mobile platform, its average value over the workspace is used to represent the variable volume, and the average of constant volume and variable volume is used to represent the total dimensional volume of the triglide. As shown in Figure 5-1(a), the volumes V_1 and V_2 have an overlapped volume, which is the volume of the prism $A_1A_2A_3-C_1C_2C_3$. If the overlapped volume is denoted by V_3 , the ratio of the workspace to dimensional volume (RWV) can be obtained using Equation (5-8). Larger ratio reflects better space utilization of the manipulator.

$$\eta_v = \frac{2V}{V_1 + \frac{\int (V_2 - V_3) dW}{\int_w dW}} \quad (5-8)$$



(a) Structure of the triglide



(b) The constant prism and the variable prism

Figure 5-1: The structure of the triglide and a constant prism and a variable prism in its structure

5.2 Constraints

5.2.1 Motion range of passive joints

In the design of a general triglide, some physical constraints should be taken into consideration, such as the motion range of passive joints. If the parallelogram limb is considered as one integrated part, each limb has two rotation DOFs, so that the rotating shaft can rotate about the frame origin along directions n_1 and n_2 as shown in Figure 5-2. Therefore, the physical

constraint posed by the passive joints allows rotation angles about the two axes smaller than α_{lim} and β_{lim} .

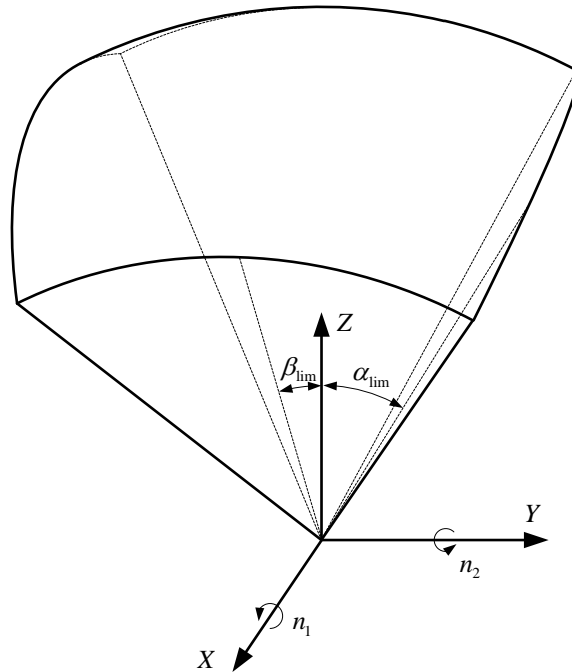


Figure 5-2: The motion range of a parallelogram limb

5.2.2 Collision-Free requirement of limbs

Besides the constraint due to the motion range of the passive joints, collision among all the limbs of the trigrade should be avoided in the movement of the mobile platform. If all the limbs are simplified as identical solid cylinders, collision-free movement can be achieved by ensuring that the shortest distance between any two limbs is larger than the diameter of the limb.

5.2.3 Prescribed Task Space

It is common to define a prescribed task space before the optimization of a parallel manipulator to guarantee that the manipulator can complete an

expected task in practice. Generally, a prescribed task space can be a sphere, cylinder or cuboid. As described in Chapter 3, a regular workspace can be used to represent approximately the true workspace of the triglide. If the workspace is sliced along the z direction, the workspace boundary can be represented approximately using an inscribed circle. If the task space is defined to be a sphere or cylinder, the radius of the task space on the slicing plane should not be larger than that of the inscribed circle. For a cuboid task space, it is required that the radius of the inscribed circle is not smaller than that of the circumscribed circle of the rectangle task space on the slicing plane. To check whether the whole task space is covered in the workspace, the flow chart of the procedures is outlined in Figure 5-3 and the following describes the checking procedures.

- 1 Obtain an approximate range of the workspace in the z direction. Obtain the dimensions of the task space. Use the radius to represent a spherical task space, the radius and height to represent a cylindrical task space, and the radius of the circumscribed circle and height to represent a rectangle task space. Set the flag value to be 0, set the value of z to be the minimum in its range and set the current height of the task space to be 0.
- 2 If the value of z is in its range, go to step 3, else go to step 8.
- 3 Obtain the workspace boundary and volume on the slicing plane z . If the flag is larger than 0, go to step 4, else go to step 5.
- 4 Increase the value of z with a step t , and then go to step 2.
- 5 Obtain the radius of the inscribed circle of the workspace on the slicing plane z . If the radius is larger than 0, go to step 6, else go to step 4.

- 6 If the current height of the task space is over its true height, set the flag to be 1 and then go to step 4, else go to step 7.
- 7 Check whether the circle of the task space at the current height is larger than the inscribed circle of the workspace. If yes, decrease the current height with a step t and continue to check until the current height is 0 or the checking result is no. If no or the current height is 0, increase the current height with a step t and then go to step 4.
- 8 If the flag is larger than 0, the task space is enveloped in the workspace, else the workspace cannot cover the task space. Return the workspace volume.

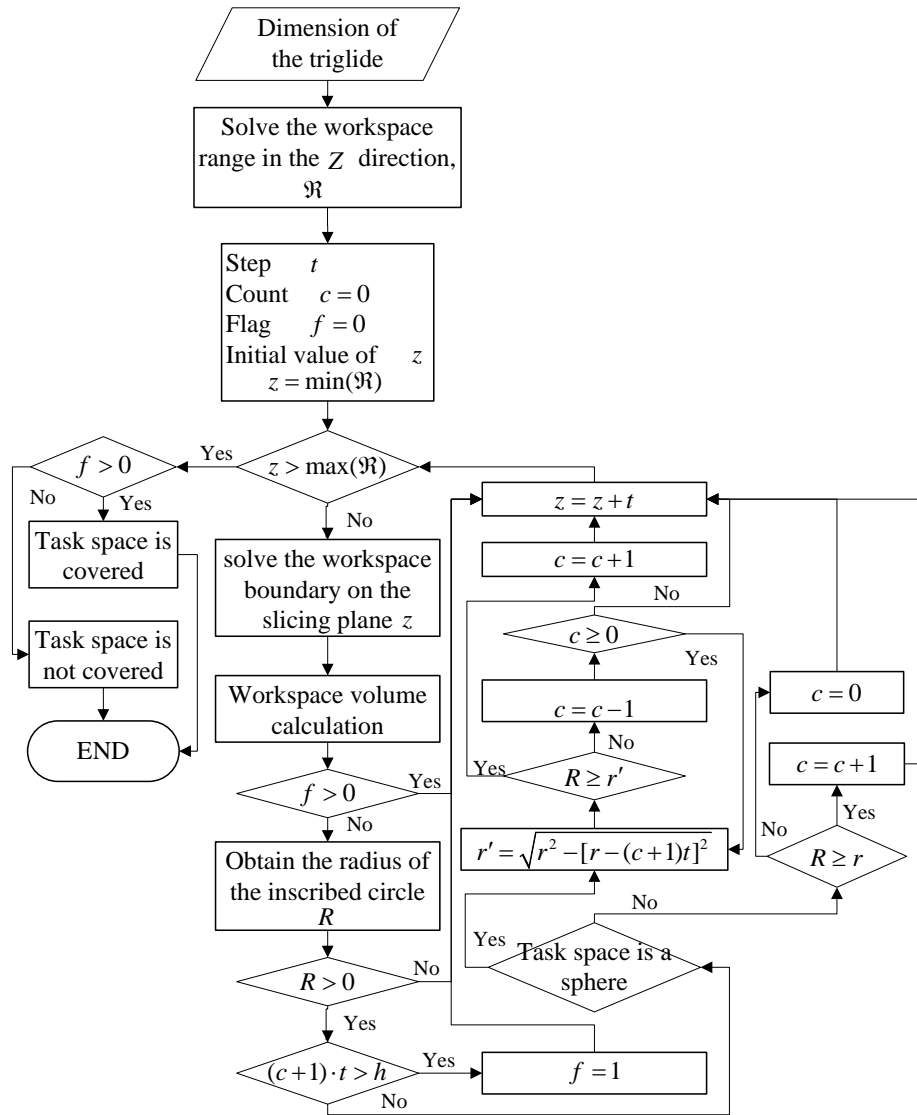


Figure 5-3: The flow chart of constraint evaluation of prescribed task space

5.3 Architecture optimization

5.3.1 Design Variables

Tens of variables are necessary to describe a general parallel manipulator. The optimization of all these variables is complicated and time-consuming. Since the triglide is symmetrical, five variables can be used to construct the manipulator, including the radius of the base plate, R_a , the radius of the

mobile platform, R_b , the limb length, l , the tilting angle, α , and the full stroke of the actuator, s_d .

5.3.2 Objective functions

As described in section 5.1, this chapter aims to maximize the GDI, GSI and RWV. If the GDI, GSI and RWV are denoted using η , η_k and η_v , the optimization can be formulated into Equation (5-9), where $\mathbf{F} = [\eta \quad \eta_k \quad \eta_v]^T$, \mathbf{C}_t denotes the constraints posed by the motion range of the passive joints and the requirements of collision avoidance and the specified task space, and \mathbf{C}_b denotes the requirements of boundaries of all the design parameters.

$$\begin{cases} \max \mathbf{F}(\mathbf{X}) \\ \mathbf{C}_t \leq 0 \\ \mathbf{C}_b \leq 0 \end{cases} \quad (5-9)$$

5.3.3 Solution algorithm

The non-dominance sorted genetic algorithm (NSGA) is used to solve the multi-objective optimization. The populations in each generation are grouped into feasible and non-feasible sets based on the constraints. The members in the feasible set are first sorted according to the level of non-domination, and later sorted using the distance of the objective values of each member to its neighbors in the space of objective functions. A member with a higher rank of non-domination means there are fewer other members that are better than it, and a higher rank of the distance provides better diversity of the populations. The non-feasible set is first sorted based on the violation numbers of the

constraints. A member with fewer violations is assigned a higher rank. The following sorting procedure is the same as the feasible set. More information about the NSGA algorithm can be found in [89]. During the genetic operation, the selection follows the principles depicted in Figure 5-4.

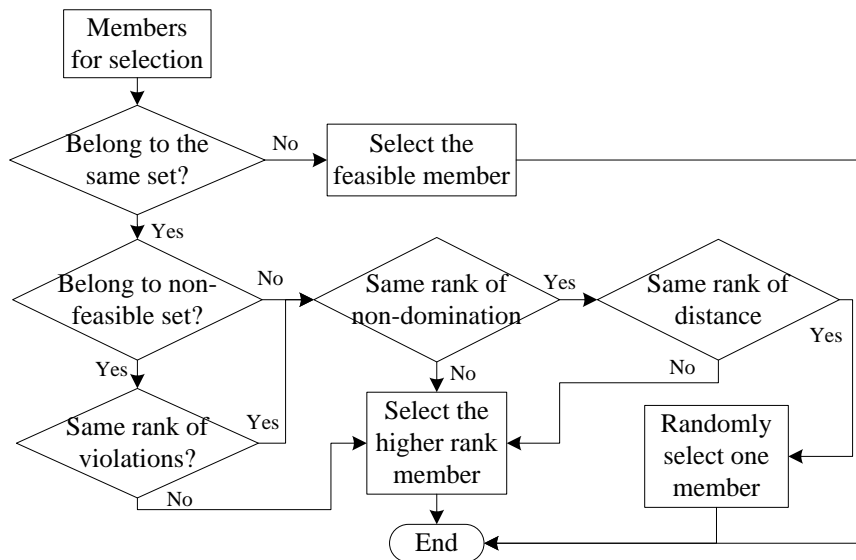


Figure 5-4: The selection principle of the NSGA

5.4 Optimization results and comparison

In order to evaluate the proposed optimization method for a general triglide, it is compared to the method proposed by Li and Xu [118]. In [118], Li and Xu optimized a 3-PUU parallel manipulator to improve its dexterity and space utilization, which has the same kinematics as the triglide. The only difference between the 3-PUU manipulator and the triglide is the different limb structures. The triglide uses a parallelogram-type structure in its limb to constrain the orientations of its mobile platform, while the 3-PUU manipulator adopts a prismatic-universal-universal limb. Only if the limb satisfies the principles described by Tsai and Joshi in [25], the 3-PUU manipulator can have three

purely translational DOFs. Because of the same kinematics, the calculations of the GDI and RWV are not affected due to the different limbs which can cause different values of the GSI. Since Li and Xu only considered the optimization of the GDI and RWV, their optimization results can be used as a comparison with the method proposed in this chapter.

Li and Xu aggregated the objectives into a scalar function using weight parameters to solve the optimization. One optimal solution, which was obtained using equal weight parameters of the dexterity and space utilization, is selected for the comparison. This solution is labelled as reference 1. The variable values of reference 1 are listed in Table 5-1. Since Li and Xu did not consider the stiffness performance, the GSI of reference 1 is obtained using the method introduced in Chapter 4. As discussed in Chapter 4, the stiffness analysis requires the geometrical and physical properties of the manipulator. For simplicity, the mobile platform, the limbs and the leads of the actuators are constructed using identical spherical solid beams. Their properties are listed in Table 5-2. The calculation of the GSI requires a unit wrench. The unit wrench can be arbitrary if the virtual work completed by the forces and moments contained in the wrench has the same unit. The applied wrench on the mobile platform is assumed to be $\begin{bmatrix} 0 & 0 & \sqrt{2}/2 & 0 & 0 & \sqrt{2}/2 \end{bmatrix}$, which means the triglide experiences a force in the z direction and a moment about z , since the triglide is the stiffest in the z direction at symmetrical configurations as shown in Chapter 4. To make the comparison convincing, the optimization in this study adopts the same constraints and the same design variables as used in [118] and they are listed in Table 5-3. The optimization

includes four variables, which are the radii R_a and R_b of the base plate and the mobile platform, limb length l and tilting angle α . The stroke of the actuator is defined to be a constant and its value is set as 2.

Table 5-1: Variable values of references 1, 2 and 3

Variables	R_a	R_b	l	α	s_d
Units	mm	Mm	mm	degree	mm
Reference 1	3	1	3	45	2
Reference 2	2.96	1.02	3.76	88.68	2
Reference 3	4.22	1.06	4.75	89.81	5.59

Table 5-2: The geometrical and physical properties of the optimized parallel manipulator

Parameters	Units	Value
A_b (Cross section area of the solid beams)	mm ²	3.1416
E (Elastic modulus of the solid beams)	GPa	210
G (Shear modulus of the solid beams)	GPa	80
N (Transmission ratio of the gear box used in actuators)		5
P (Lead of the lead screw used in actuators)	mm	3
k_{tor} (Equivalent stiffness of the motor)	N · m/rad	3×10^5

Table 5-3: Design variables and constraints

Design variables	R_a /mm	$1 \leq R_a \leq 8$
	R_b /mm	$1 \leq R_b \leq 8$
	l /mm	$2 \leq l \leq 8$
	α /degree	$0 \leq \alpha \leq 105$
Constant variable	s_d /mm	2
Motion range	α_{lim} /degree	40
	β_{lim} /degree	40
Other constraints		$R_a > R_b$

In addition, the number of populations in each generation is set as 200, and the total generations are 1000 in the NSGA algorithm. This optimization algorithm is implemented using MatLab (Mathworks, Inc).

Figure 5-5 depicts the Pareto front obtained in the 1000th generation and its projection on three coordinate planes. From Figure 5-5, it can be seen that the RWV is conflicting with the GDI and GSI. It is impossible to achieve optimal RWV, GDI and GSI simultaneously. It is also found that the GDI and GSI are nearly harmonious when the GDI is less than about 0.5, but they become conflicting as the GDI becomes larger. Due to the complex relationship among these three properties, the NSGA algorithm is capable of providing various solutions. With these solutions, the user can select the appropriate one based on other requirements. If the requirement is set to be better than reference 1, 14 solutions are found from the Pareto front. The values of objective functions of these solutions are depicted in Figure 5-6. It can be seen that the objective values of all the solutions are better than those reported in reference 1.

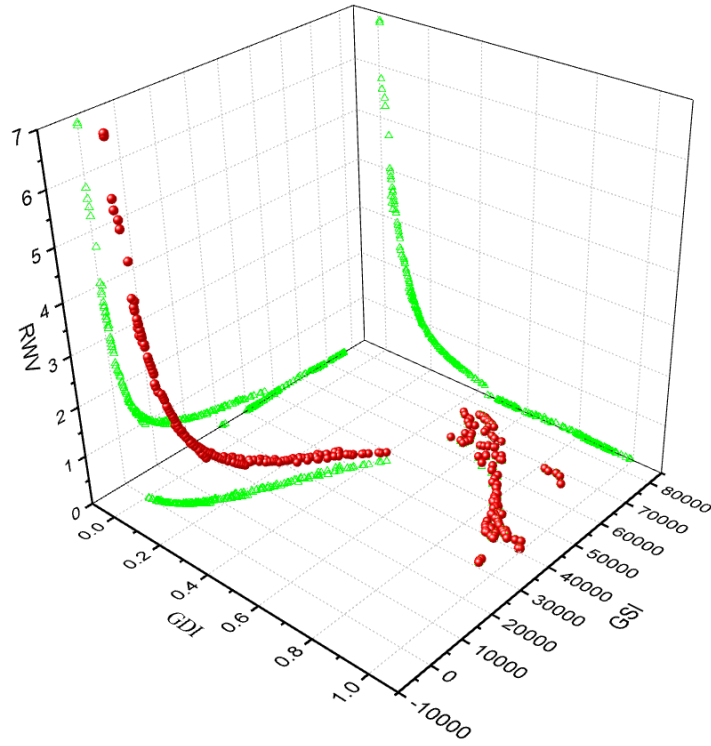


Figure 5-5: The Pareto front obtained using the NSGA algorithm

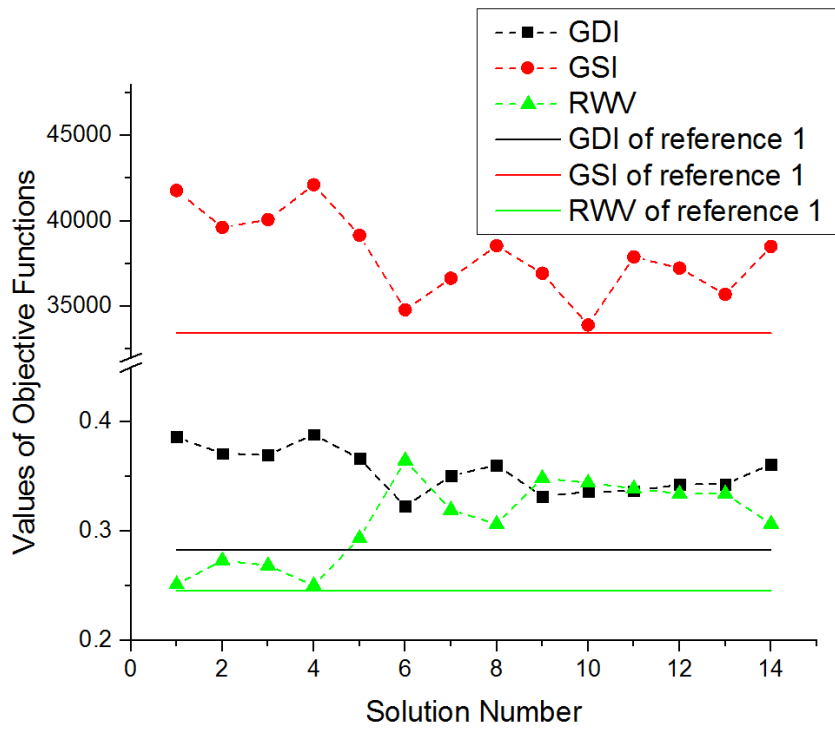


Figure 5-6: The objective values of reference 1 and 14 optimal solutions

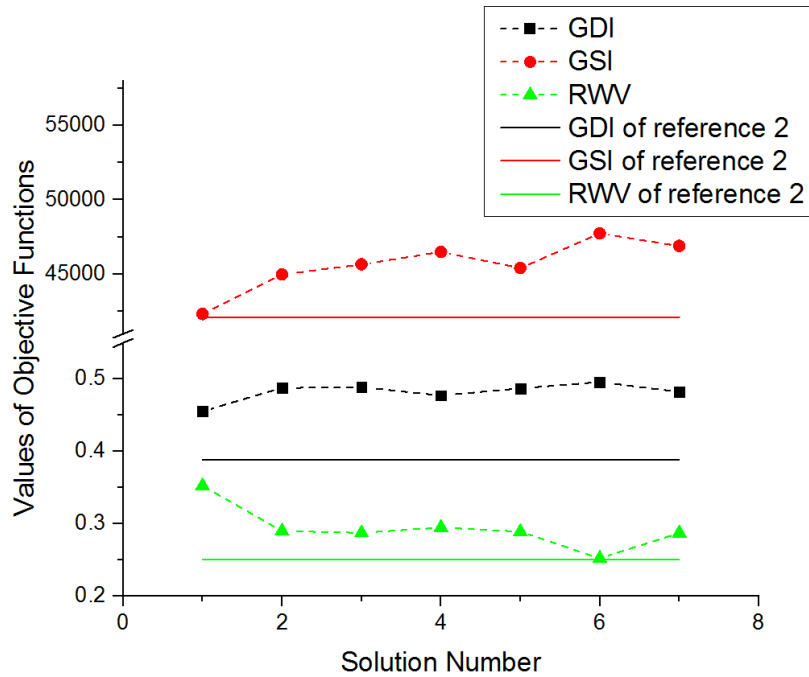


Figure 5-7: The objective values of reference 2 and the seven optimal solutions

It should be noted that the optimization compared to reference 1 does not include the stroke s_d . However, the stroke is believed to have significant effect on the performance of a parallel manipulator. Thus, the stroke is considered in the design variables and the optimization is performed again. The boundary of the stroke is defined to be $2 \leq s_d \leq 8$. In this optimization, one of the 14 optimal solutions plotted in Figure 5-6 is selected as in reference 2. Its variable values are listed in Table 5-1. This solution has the largest values of the GDI and GSI in all the 14 solutions.

Compared to reference 2, seven optimal solutions are obtained from the new optimization. Their objective values are depicted in Figure 5-7, which shows that these optimal solutions are better than reference 2. From Figure 5-6 and Figure 5-7, it shows that the optimization proposed in this study can provide

better solutions as compared to the method proposed in [118], and the inclusion of the stroke into the design variables is able to improve the optimal solutions further.

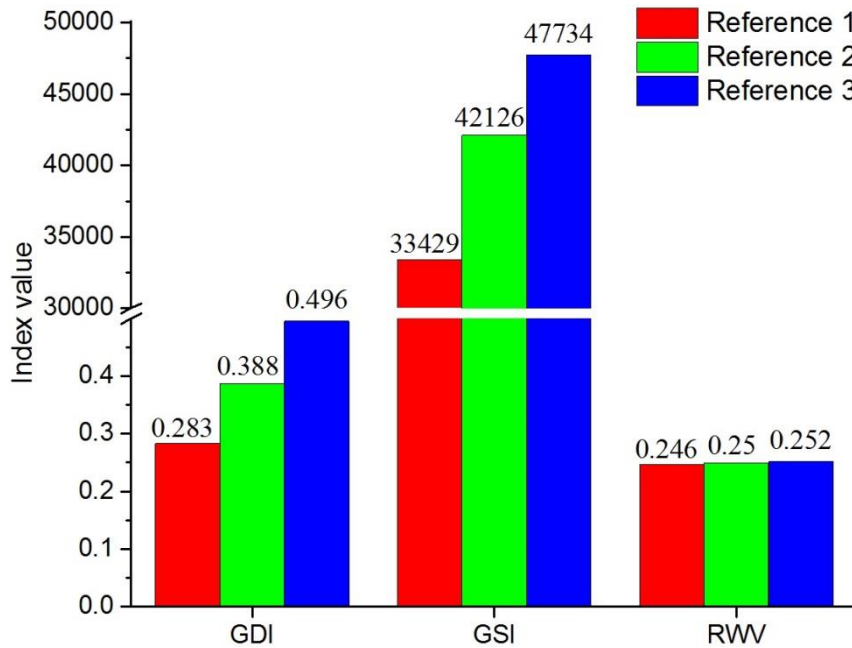


Figure 5-8: The GDI, GSI and RWV of references 1, 2 and 3

One solution is selected from the seven optimal results obtained using the methodology considering the stroke of actuators and labelled as reference 3. This reference has the maximum GDI and GSI compared with the other six optimal results. Table 5-1 lists the variable values of reference 3 and Figure 5-8 compares the GDI, GSI and RWV of references 1, 2 and 3. From this figure, it can be seen that reference 3 has the largest GDI, GSI and RWV. Comparing with reference 1, the GDI is improved by 75.26%, the GSI is raised by 42.79% and the RWV is increased by 2.44%.

5.5 Conclusion

This chapter provides an optimization method for a general triglide-structure parallel manipulator. The optimization aims to improve the dexterity, stiffness and space utilization of the manipulator. The deformation of the mobile platform, the limbs and the actuators is considered to obtain the stiffness matrix. A novel stiffness index is used to measure the stiffness property related to applied external wrench. The variable dimensional volume due to the posture of a general triglide is computed to obtain its ratio of space utilization without using an approximate regular shape to estimate its physical size. This method can be used to optimize all general triglides, and it can also be used to optimize specific triglides, such as the linear delta and orthoglide.

Comparing with published work, the method proposed in this chapter is shown to be capable of providing optimal designs in terms of dexterity, stiffness and space utilization. The inclusion of the stroke of the actuators into the design variables has also shown to be capable of improving the performance of a general triglide further. Hence, the proposed method is competent for the optimization of general triglides and it is highly recommended to consider the stroke of the actuators in the optimization of a parallel manipulator.

CHAPTER 6 REGISTRATION OF THE HYBRID ROBOT

The registration of an industrial robot is crucial whenever its interaction with objects has to be detected by a tracking system. However, there is no reported solution to address this issue for a hybrid robot. As discussed in Chapter 2, The registration can be represented with an equation where \mathbf{X} is the transformation matrix of the relative pose of a global coordinate frame with respect to the end effector of the parallel manipulator, \mathbf{Y} is a transformation from a global coordinate frame to the base coordinate frame of the serial robot, \mathbf{Z} is a constant matrix that denotes the transformation from the flange of the serial robot to the base of the parallel manipulator.

$$\mathbf{AX} = \mathbf{YBZC} \quad (6-1)$$

Different from classical registration, the registration of a hybrid robot requires the need to solve an equation with three unknowns, which includes the transformation matrices \mathbf{X} , \mathbf{Y} and \mathbf{Z} . Two of these unknowns are coupled together as shown in Equation (6-1). This property makes it difficult to obtain a closed-form solution. To determine these unknowns, this chapter presents the Degradation-Kronecker (D-K) method, which provides a closed-form solution for the registration of a hybrid robot. Since closed-form methods were reported to suffer from low accuracy under perturbation [51], a pure nonlinear (PN) method, which uses an iterative algorithm, is proposed in this study to overcome this problem. The product of exponentials (POE) method is also used to solve this registration, since this method is able to avoid kinematic

singularity. The proposed methods are compared to analyze their performance with respect to computation time, accuracy and robustness to noise.

6.1 The D-K method

The D-K method separates the hybrid robot into two components, namely, the serial and parallel components. This separation allows the hybrid robot to be registered with respect to a tracking system using three steps. The serial component and the parallel component are determined individually in the first two steps, and the results are used to complete the registration of the hybrid robot in the last step.

First, the parallel manipulator is locked for the registration of the serial component. The transformation from the tool to the flange of the serial robot which is described in Figure 2-4, is denoted by \mathbf{X}_t , $\mathbf{X}_t = \mathbf{X}\mathbf{C}^{-1}\mathbf{Z}^{-1}$. Since the parallel manipulator is locked, \mathbf{X}_t is a constant due to the constant \mathbf{C} , which denotes the transformation from the base of the parallel manipulator to its end effector. Hence, Equation (6-1) is degraded to an equation that is similar to the HEC problem,

$$\mathbf{A}\mathbf{X}_t = \mathbf{Y}\mathbf{B} \quad (6-2)$$

In the second step, the serial robot is locked to allow the registration of the parallel component. The transformation from the global coordinate to the base of the parallel manipulator is denoted by \mathbf{Y}_t , $\mathbf{Y}_t = \mathbf{Y}\mathbf{B}\mathbf{Z}$. Since \mathbf{Y}_t is a

constant, similar to the first step, Equation (6-1) is degraded to the following equation.

$$\mathbf{A}\mathbf{X} = \mathbf{Y}_t \quad (6-3)$$

Many solutions have been proposed for Equations (6-2) and (6-3). Since the Kronecker product method is claimed to be fast and accurate, this method is used to obtain \mathbf{X}_t , \mathbf{Y}_t , \mathbf{X} and \mathbf{Y} . For arbitrary matrix \mathbf{A} and matrix \mathbf{B} , their Kronecker product is denoted as $\mathbf{A} \otimes \mathbf{B}$. It should be noted that $\mathbf{A} \otimes \mathbf{B}$ and $\mathbf{B} \otimes \mathbf{A}$ are usually different. A homogenous transformation matrix \mathbf{A}

$$\mathbf{A} = \begin{bmatrix} \mathbf{R}_A & \mathbf{t}_A \\ 0 & 1 \end{bmatrix}$$

has rotation and translation components,

$$\mathbf{R}_A = \begin{bmatrix} r_1 & r_2 & r_3 \\ r_4 & r_5 & r_6 \\ r_7 & r_8 & r_9 \end{bmatrix}, \quad \mathbf{t}_A = [t_x \quad t_y \quad t_z]^T$$

with the representation $\text{Vec}(\mathbf{R}) = [r_1 \quad r_2 \quad \dots \quad r_9]^T$.

With the Kronecker product method, Equation (6-2) can be reformulated to be a linear equation,

$$\begin{bmatrix} \mathbf{R}_A \otimes \mathbf{I}_3 & -\mathbf{I}_3 \otimes \mathbf{R}_B^T & 0 & 0 \\ 0 & \mathbf{I}_3 \otimes \mathbf{t}_B^T & -\mathbf{R}_A & \mathbf{I}_3 \end{bmatrix} \begin{bmatrix} \text{Vec}(\mathbf{R}_{X_t}) \\ \text{Vec}(\mathbf{R}_Y) \\ \mathbf{t}_{X_t} \\ \mathbf{t}_Y \end{bmatrix} = \begin{bmatrix} 0 \\ \mathbf{t}_A \end{bmatrix} \quad (6-4)$$

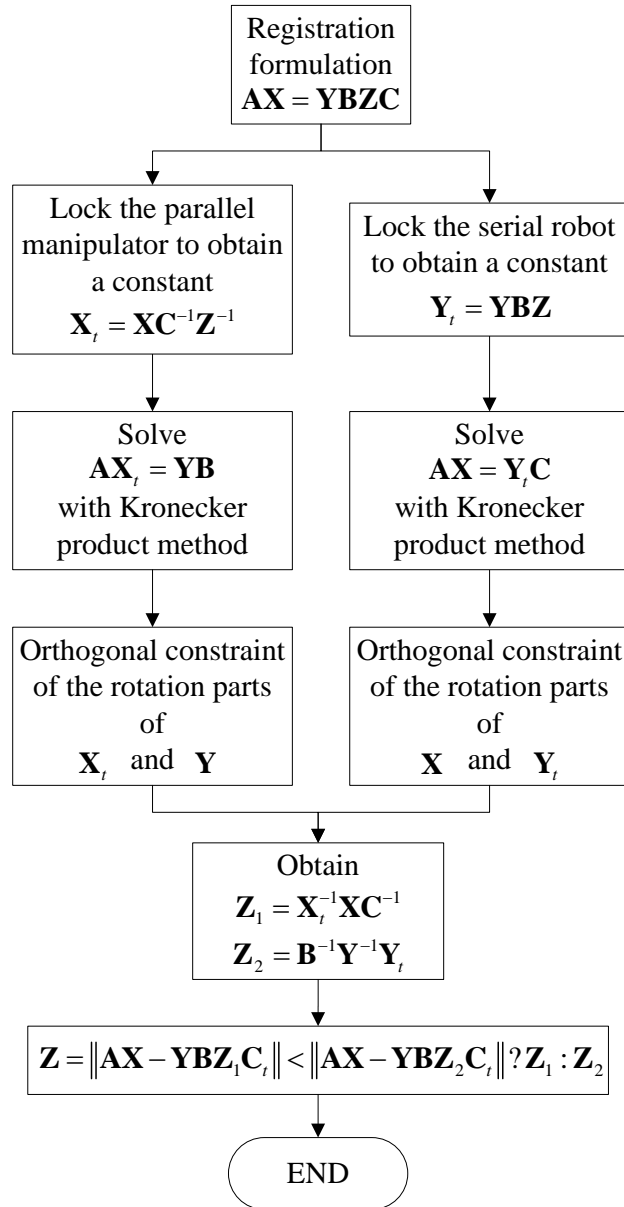


Figure 6-1: The flowchart of the D-K method

Using several measurements, Equation (6-4) can be used to form an equation system to obtain a unique solution. Generally, \mathbf{R}_{X_t} and \mathbf{R}_Y that have been determined, which are the rotation components of the transformation matrices \mathbf{X}_t and \mathbf{Y} , are not orthogonal. An orthogonal constraint is necessary to determine appropriate rotation matrices. The SVD approach is used to obtain the closest orthogonal matrices of \mathbf{R}_{X_t} and \mathbf{R}_Y . For example, the closest

orthogonal matrix $\mathbf{\Omega}_{X_i}$ of \mathbf{R}_{X_i} can be obtained from minimizing the Frobenius norm $\|\mathbf{\Omega}_{X_i} - \mathbf{R}_{X_i}\|$. If the SVD result of \mathbf{R}_{X_i} is $\mathbf{R}_{X_i} = \mathbf{U}_{X_i} \mathbf{\Sigma}_{X_i} \mathbf{V}_{X_i}^*$, where \mathbf{U}_{X_i} is a unitary matrix, $\mathbf{\Sigma}_{X_i}$ is a diagonal matrix and $\mathbf{V}_{X_i}^*$ is the conjugate transpose of a unitary matrix, it can be proved that the product $\mathbf{U}_{X_i} \mathbf{V}_{X_i}^*$ is the solution of the minimization of the Frobenius norm $\|\mathbf{\Omega}_{X_i} - \mathbf{R}_{X_i}\|$. Equation (6-3) can be solved using the same procedure. After obtaining \mathbf{X}_i , \mathbf{Y} , \mathbf{X} and \mathbf{Y}_i , $\mathbf{Z}_1 = \mathbf{X}_i^{-1} \mathbf{X} \mathbf{C}^{-1}$ and $\mathbf{Z}_2 = \mathbf{B}^{-1} \mathbf{Y}^{-1} \mathbf{Y}_i$ can be obtained in the third step. In theory, $\mathbf{Z} = \mathbf{Z}_1 = \mathbf{Z}_2$. However, noise always causes $\mathbf{Z}_1 \neq \mathbf{Z}_2$ in practice. Therefore, the unknown \mathbf{Z} is assigned the value of \mathbf{Z}_1 or \mathbf{Z}_2 , whichever has the smaller registration residuals. Figure 6-1 presents the flowchart of the D-K method.

6.2 The PN method

Different from the D-K method, the PN method [51] solves all the unknowns, \mathbf{X} , \mathbf{Y} and \mathbf{Z} simultaneously. Since each rigid transformation is composed of one translation and one rotation, Equation (6-1) can be decomposed into Equation (6-5). In Equation (6-5), \mathbf{R}_A , \mathbf{R}_B , \mathbf{R}_C , \mathbf{R}_X , \mathbf{R}_Y , \mathbf{R}_Z denote the rotation components of the transformation matrices \mathbf{A} , \mathbf{B} , \mathbf{C} , \mathbf{X} , \mathbf{Y} , \mathbf{Z} , and \mathbf{t}_A , \mathbf{t}_B , \mathbf{t}_C , \mathbf{t}_X , \mathbf{t}_Y , \mathbf{t}_Z denote their translation components.

$$\begin{cases} \mathbf{R} = \mathbf{R}_A \mathbf{R}_X - \mathbf{R}_Y \mathbf{R}_B \mathbf{R}_Z \mathbf{R}_C \\ \mathbf{t} = \mathbf{R}_A \mathbf{t}_X - \mathbf{R}_Y \mathbf{t}_B - \mathbf{R}_Y \mathbf{R}_B \mathbf{t}_Z - \mathbf{R}_Y \mathbf{R}_B \mathbf{R}_Z \mathbf{t}_C + \mathbf{t}_A - \mathbf{t}_Y \end{cases} \quad (6-5)$$

Correspondingly, the error function can be defined as

$$\mathbf{F} = \begin{bmatrix} \text{Vec}(\mathbf{R}) \\ \mathbf{t} \end{bmatrix} \quad (6-6)$$

where \mathbf{F} is a row vector with 12 elements.

For an arbitrary rotation matrix \mathbf{R} , it can be represented by a normalized quaternion $\mathbf{q} = [s \ i \ j \ k]$. If the normalization of the quaternion is defined as $\mathbf{q} = \mathbf{q}/\|\mathbf{q}\|$, and $\mathbf{q} = [1 \ 0 \ 0 \ 0]$ if $s = 0$, there is only one normalized quaternion for an arbitrary quaternion. Thus, for a given quaternion, its corresponding rotation matrix can always be found. If the conversion from the quaternion to the rotation matrix is denoted by $\mathbf{R}(q)$, Equation (6-7) can be obtained from Equation (6-5). With the quaternion representations, the rotation components of \mathbf{X} , \mathbf{Y} and \mathbf{Z} are always orthogonal in the iterative computation process.

$$\begin{cases} \mathbf{R} = \mathbf{R}_A \mathbf{R}(q_X) - \mathbf{R}(q_Y) \mathbf{R}_B \mathbf{R}(q_Z) \mathbf{R}_C \\ \mathbf{t} = \mathbf{R}_A \mathbf{t}_X - \mathbf{R}(q_Y) \mathbf{t}_B - \mathbf{R}(q_Y) \mathbf{R}_B \mathbf{t}_Z - \mathbf{R}(q_Y) \mathbf{R}_B \mathbf{R}(q_Z) \mathbf{t}_C + \mathbf{t}_A - \mathbf{t}_Y \end{cases} \quad (6-7)$$

Assuming that the number of measurements is n , each measurement produces a F_i with Equations (6-7) and (6-6). The PN method aims to find optimal solutions of \mathbf{q}_X , \mathbf{q}_Y , \mathbf{q}_Z , \mathbf{t}_X , \mathbf{t}_Y , and \mathbf{t}_Z to minimize Equation (6-8),

$$\sum_{i=1}^n \sum_{j=1}^{12} f_j^2 \quad (6-8)$$

where f_j denotes the i th entry of the error vector \mathbf{F} .

The registration has been transformed into a least-square problem. The Levenberg–Marquardt (L-M) algorithm can be used to obtain the optimal solutions. With the conversion $\mathbf{R}(q)$, the final solutions of \mathbf{X} , \mathbf{Y} and \mathbf{Z} can be obtained from \mathbf{q}_X , \mathbf{q}_Y , \mathbf{q}_Z , \mathbf{t}_X , \mathbf{t}_Y , and \mathbf{t}_Z .

6.3 The POE method

The POE formula can be used to solve the calibration problem. This method has been adopted by several researchers for the calibration of a serial robot [119–122] or a parallel manipulator [123]. According to Okamura [122], the POE method can avoid kinematic singularity which always happens in the kinematic representations based on the Denavit-Hartenberg parameters. With the POE method, each rigid transformation is represented by $e^{\hat{\xi}_i}$. $\hat{\xi}_i$ denotes the twist of the i th joint, which belongs to the Lie algebra $se(3)$ of the special Euclidean group $SE(3)$. If \mathbf{v}_i denotes the position vector of the i th joint axis, and $\hat{\omega}_i$ denotes the skew-symmetric matrix of ω_i , which is the unit directional vector of the i th joint axis, Equation (6-9) can be obtained,

$$\hat{\xi}_i = \begin{bmatrix} \hat{\omega}_i & \mathbf{v}_i \\ 0 & 0 \end{bmatrix} \quad (6-9)$$

where $\omega_i = [\omega_{1i} \ \omega_{2i} \ \omega_{3i}]^T$, $\mathbf{v}_i = [v_{1i} \ v_{2i} \ v_{3i}]^T$, and

$$\xi_i = \begin{bmatrix} \mathbf{v}_i \\ \omega_i \end{bmatrix}, \quad \hat{\omega}_i = \begin{bmatrix} 0 & -\omega_{3i} & \omega_{2i} \\ \omega_{3i} & 0 & -\omega_{1i} \\ -\omega_{2i} & \omega_{1i} & 0 \end{bmatrix}.$$

For the hybrid robot, its forward kinematics can be represented as Equation (6-10), if \mathbf{X}^{-1} , \mathbf{Y} , and \mathbf{Z} are represented by $e^{\hat{\xi}_{xst}}$, $e^{\hat{\xi}_{yst}}$ and $e^{\hat{\xi}_{zst}}$, and $\mathbf{B} = e^{\hat{\xi}_s}$, $\mathbf{A} = e^{\hat{\xi}_p}$.

$$f = e^{\hat{\xi}_{yst}} e^{\hat{\xi}_s} e^{\hat{\xi}_{zst}} e^{\hat{\xi}_p} e^{\hat{\xi}_{xst}} \quad (6-10)$$

Since the registration of the hybrid robot only considers errors in $\hat{\xi}_{xst}$, $\hat{\xi}_{yst}$ and $\hat{\xi}_{zst}$, The error model can be obtained as Equation (6-11).

$$\delta f = \delta e^{\hat{\xi}_{yst}} e^{\hat{\xi}_s} e^{\hat{\xi}_{zst}} e^{\hat{\xi}_p} e^{\hat{\xi}_{xst}} + e^{\hat{\xi}_{yst}} e^{\hat{\xi}_s} \delta e^{\hat{\xi}_{zst}} e^{\hat{\xi}_p} e^{\hat{\xi}_{xst}} + e^{\hat{\xi}_{yst}} e^{\hat{\xi}_s} e^{\hat{\xi}_{zst}} e^{\hat{\xi}_p} \delta e^{\hat{\xi}_{xst}} \quad (6-11)$$

If right multiplied by f^{-1} , Equation (6-12) can be obtained.

$$\begin{aligned} \delta f \cdot f^{-1} &= \delta e^{\hat{\xi}_{yst}} e^{-\hat{\xi}_{yst}} + e^{\hat{\xi}_{yst}} e^{\hat{\xi}_s} \delta e^{\hat{\xi}_{zst}} e^{-\hat{\xi}_{zst}} e^{-\hat{\xi}_s} e^{-\hat{\xi}_{yst}} \\ &\quad + e^{\hat{\xi}_{yst}} e^{\hat{\xi}_s} e^{\hat{\xi}_{zst}} e^{\hat{\xi}_p} \delta e^{\hat{\xi}_{xst}} e^{-\hat{\xi}_{xst}} e^{-\hat{\xi}_p} e^{-\hat{\xi}_{zst}} e^{-\hat{\xi}_s} e^{-\hat{\xi}_{yst}} \end{aligned} \quad (6-12)$$

If the operator \vee maps $\hat{\xi}_i \in se(3)$ into $\xi_i \in \mathbf{R}^6$, with the explicit expression given in [121],

$$\begin{aligned} [\delta e^{\hat{\xi}_{ist}} e^{-\hat{\xi}_{ist}}]^\vee &= (\mathbf{I}_6 + \frac{4 - \theta_{ist} s \theta_{ist} - 4c \theta_{ist}}{2\theta_{ist}^2} \boldsymbol{\Omega}_{ist} + \frac{4\theta_{ist} - 5s \theta_{ist} + \theta_{ist} c \theta_{ist}}{2\theta_{ist}^3} \boldsymbol{\Omega}_{ist}^2 \\ &\quad + \frac{2 - \theta_{ist} s \theta_{ist} - 2c \theta_{ist}}{2\theta_{ist}^4} \boldsymbol{\Omega}_{ist}^3 + \frac{2\theta_{ist} - 3s \theta_{ist} + \theta_{ist} c \theta_{ist}}{2\theta_{ist}^5} \boldsymbol{\Omega}_{ist}^4) \delta \xi_{ist} \\ &= A_{ist} \delta \xi_{ist} \end{aligned}$$

where $\boldsymbol{\Omega}_{ist} = \begin{bmatrix} \hat{\boldsymbol{\omega}}_{ist} & 0 \\ \hat{\mathbf{v}}_{ist} & \hat{\boldsymbol{\omega}}_{ist} \end{bmatrix}$, and $\theta_{ist} = \|\boldsymbol{\omega}_{ist}\|$, Equation (6-13) can be obtained.

$$\begin{aligned} [\delta f \cdot f^{-1}]^\vee &= [\delta e^{\hat{\xi}_{yst}} e^{-\hat{\xi}_{yst}}]^\vee + Ad(e^{\hat{\xi}_{yst}} e^{\hat{\xi}_s}) [\delta e^{\hat{\xi}_{zst}} e^{-\hat{\xi}_{zst}}]^\vee \\ &\quad + Ad(e^{\hat{\xi}_{yst}} e^{\hat{\xi}_s} e^{\hat{\xi}_{zst}} e^{\hat{\xi}_p}) [\delta e^{\hat{\xi}_{xst}} e^{-\hat{\xi}_{xst}}]^\vee \end{aligned} \quad (6-13)$$

If letting $y = [\delta f \cdot f^{-1}]^\vee$, $\mathbf{J} = \begin{bmatrix} A_{yst} & Ad(e^{\hat{\xi}_{yst}} e^{\hat{\xi}_{zs}})A_{zst} & Ad(e^{\hat{\xi}_{yst}} e^{\hat{\xi}_{zs}} e^{\hat{\xi}_{zst}} e^{\hat{\xi}_p})A_{xst} \end{bmatrix}$,

and $\mathbf{x} = [\delta \xi_{yst} \quad \delta \xi_{zst} \quad \delta \xi_{xst}]^T$, Equation (6-13) can be reformulated to Equation (6-14).

$$y = \mathbf{J} \cdot \mathbf{x} \quad (6-14)$$

With Equation (6-14), a generic error model has been proposed. If f_n denotes the nominal pose and f_a denotes the measured pose, Equation (6-15) can be obtained if f_n and f_a are assumed to be sufficiently close.

$$\delta f \cdot f^{-1} = \log(f_a \cdot f_n^{-1}) \quad (6-15)$$

The iterative L-M method can be used to solve the least-square problem. The process is illustrated in Figure 6-2.

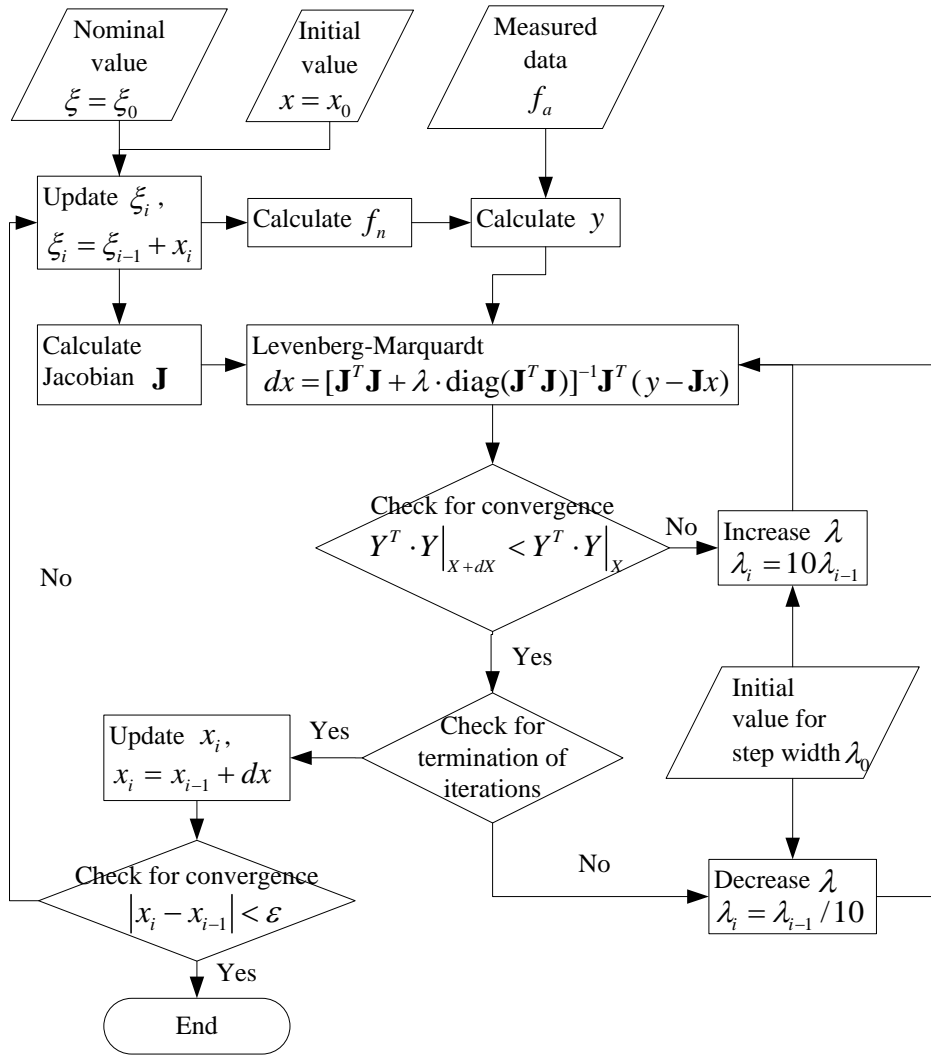


Figure 6-2: The flowchart of POE method

6.4 Simulations

The D-K method, PN method and POE method are tested and compared with numerical simulations. Assuming \mathbf{X} , \mathbf{Y} and \mathbf{Z} are known, the value of \mathbf{A} can be obtained using Equation (6-1) for each joint configuration of the serial robot and the parallel manipulator. Shah [96] proved that at least three different poses are necessary to obtain a unique solution to Equation (6-2). Since the D-K method degrades the registration of a hybrid robot into two equations, the number of poses to be measured should be $n \geq 6$. It has been found that rotation and translation errors tend to decrease with more pose

measurements [52], hence a set of data with $n=20$ is prepared in this simulation with $n_1=10$ for the serial component and $n_2=10$ for the parallel component. This set of data is not perturbed by noise. Nevertheless, noise is common in practice. It is necessary to have several sets of data with noise included to investigate the performance of the proposed methods against perturbation. Hence, different magnitudes of noise are added to the nominal values. Noise can have normal distribution and its standard deviations are defined to be 0.5%, 1% and 2% of their nominal values. Since each pose contains a rotation component and a translation component, noise generation is separated into two parts. For the rotation component, the rotation matrix is first converted to an angle-axis representation, and the noise is added to the angle and every axial value of the axis. For the translation component, the noise is added to every axial value.

To ensure that the final result is globally optimal, the methods are implemented several times with different initial starting points until the variation of the norm of the residuals is within a specified tolerance. The initial starting points are generated randomly with their translation components in a range $[-1000 \ 1000]$, and the tolerance is defined to be smaller than 1.0×10^{-6} in this study. For visual representation, the rotation residual is defined to be $\|\mathbf{R}\|$, and $\|\mathbf{t}\|$ denotes the translation residual.

Figure 6-3 shows the rotation residuals of the nominal values and the optimal solutions obtained using the POE method, D-K method and PN method under

different noise magnitudes. The box and whiskers in Figure 6-3 depict the distributions of the residuals of all the 20 simulated measurements. It can be seen that the mean values of the rotation residuals increase with increase in noise. Higher noise level also increases the intervals between the minima and the maxima of the residuals. There are larger residuals when more noise is included in the measurements. This phenomenon can be observed in Figure 6-4, which illustrates the translation residuals under different noise levels. Figure 6-3 and Figure 6-4 show that the PN method can obtain smaller mean value and maximum of the residuals than the D-K method, and hence the PN method is more accurate than the D-K method. The low accuracy of the D-K method is possibly attributed to error propagation in the degradation process and the orthogonal regulation in the Kronecker product method. Additionally, it should be noted that the rotation residuals of the PN method are comparable to that of the nominal values, while the translation residuals of the PN method are smaller than that of the nominal values. From Figure 6-3, it can be seen that the POE method can obtain comparable rotation residuals to the PN method. However, the translational residuals obtained using the POE method are larger than that obtained using the PN method. The larger errors might be due to the assumption of the POE method in which the measured poses and computed poses are considered to be sufficiently close. Although the POE and D-K methods cannot decrease the residuals compared to the nominal values, the difference is not significant. Therefore, it can be stated that all the methods can succeed in solving the registration problem under different noise magnitudes. These methods are robust to perturbances.

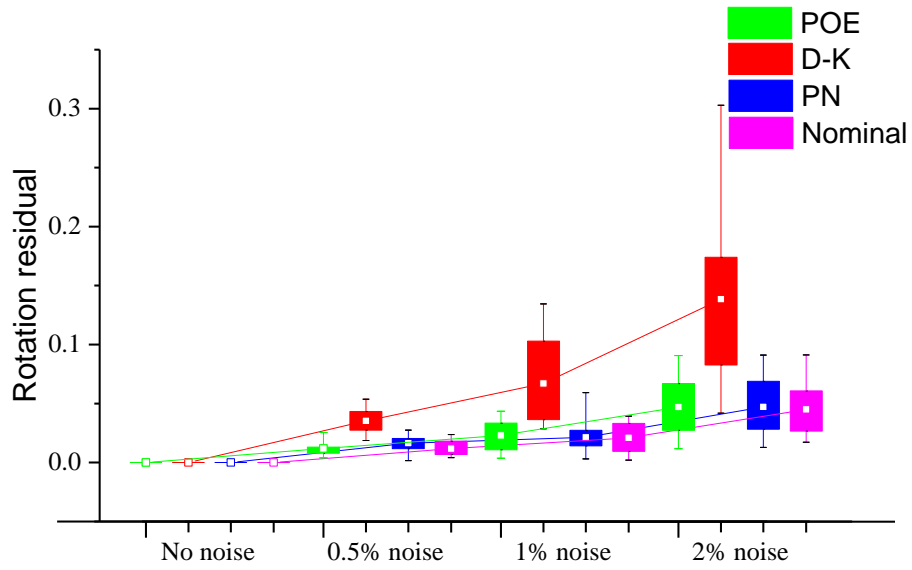


Figure 6-3: Rotation residuals obtained from the POE, D-K and PN method

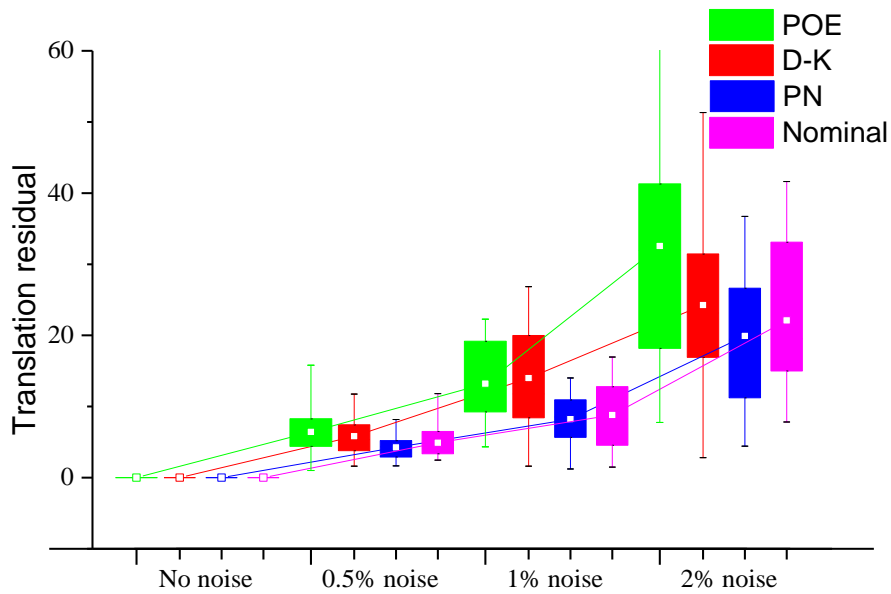


Figure 6-4: Translation residuals obtained from the POE, D-K and PN method

To compare the computation time of these methods, they are implemented 100 times under each noise level using the same software and hardware described in Chapter 3. The average computation time is listed in Table 6-1. This table shows that the computation time of the D-K method is not affected by noise since it is a closed-form approach, while noise increases obviously the average

computation time of the PN method since it is an iterative process. Although noise also increases the average computation time of the POE method, the effect of noise is not obvious. Without noise, the computation time of the POE method is the longest. It is noted that shortest computation time can be obtained with the PN method due to its one-step process if there is no noise. However, with the presence of 2% noise, the PN method requires the longest time compared with the D-K and POE methods.

Table 6-1: The average computation time of the POE, D-K and PN methods under different noise levels

	No noise	0.5% noise	1% noise	2% noise
Units	Millisecond	Millisecond	Millisecond	Millisecond
POE method	4798.7	5392.3	5700.9	6557.8
D-K method	629.6	720.0	668.2	698.5
PN method	409.0	5404.9	15112.2	24880.6

6.5 Experiments

In this section, the POE, D-K and PN method are compared using real data obtained from a hybrid robot, which comprises a serial robot Scorbot-ER VII (Eshed Robotec Inc.) and a self-constructed triglide, as shown in Figure 6-5. The dimensions of the triglide are obtained using the optimization method proposed in Chapter 5 with a constant stroke $s_d = 50$ and the requirement of a task space which is a cuboid with 60mm in length and width and 30mm height. The dimensions of the triglide are listed in Table 6-2. The tool pose of the hybrid robot is captured using an OptiTrack system (Natural Point Inc.) with three cameras. The computer and programming environment used for the

implementation of the proposed methods are the same as that described in the simulation section.

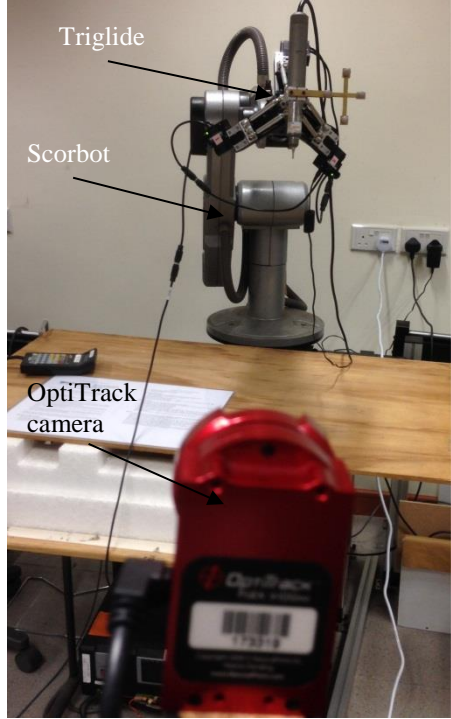


Figure 6-5: The experimental setup of a hybrid robot

Table 6-2: Dimensions of the triglide

Parameters	R_a	R_b	l	α	s_d
Units	mm	mm	mm	degree	mm
Value	43.9168	18.2703	164.4371	44.5647	50

In this experiment, 40 measurements are obtained by adjusting the joint configurations of the serial robot and the parallel manipulator. As each step of the first two steps of the D-K method requires the number of poses measured to be $n \geq 3$, and the serial robot has a much larger workspace than the triglide, 30 poses are obtained when the parallel manipulator is locked, and the remaining 10 measurements are obtained when the serial robot is locked. Similar to the simulation, all the methods are implemented several times with

different initial starting points to obtain the final results. Figure 6-6 shows the rotation residuals of the final result, and the translation residuals are depicted in Figure 6-7. Their average values are listed in Table 6-3 with the average computation times of these methods. The average time is obtained by performing each method 100 times using the same set of real data.

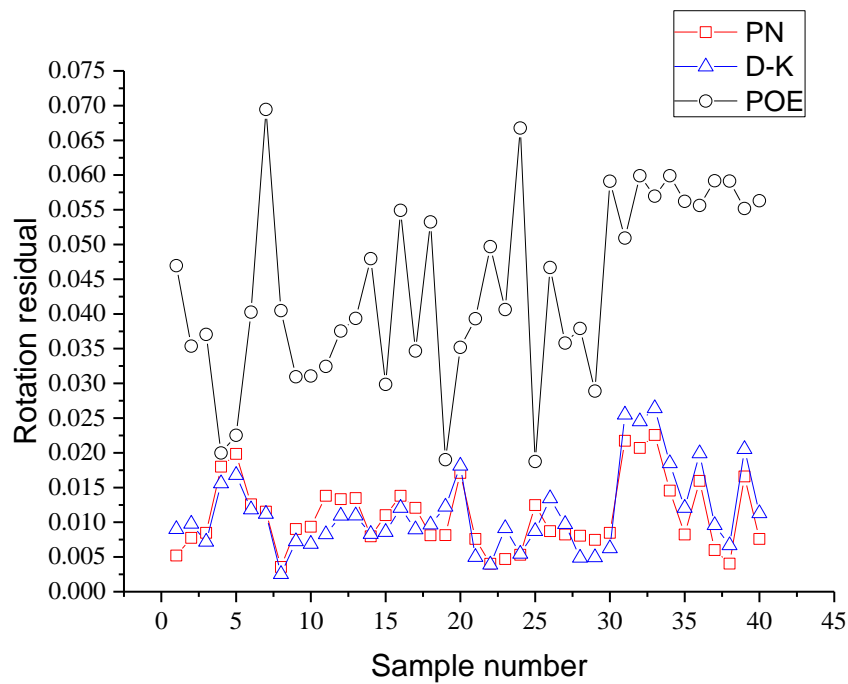


Figure 6–6: Rotation residuals obtained using the POE, D-K and the PN method

As depicted in Figure 6-6, the rotation residuals obtained using the PN method overlaps significantly with the rotation residuals obtained using the D-K method, but the rotation residuals obtained using the POE method are larger than the PN and D-K method. Table 6-3 shows that the average rotation residual of the PN method is slightly smaller than that of the D-K method, while the difference of the translation residuals between them is significant, as shown in Figure 6-7. Figure 6-7 illustrates that all the translation residuals of

the PN method are located in the interval of 0 to 2mm. The average residual is 1.1004 as listed in Table 6-3. In contrast, the D-K method produces translation residuals which maximum is about 10mm. Although the difference between rotation residuals is very small, the smaller translation residuals show that the PN method is more accurate than the D-K method. Table 6-3 shows that the computation time of the PN method is longer than that of the D-K method. This finding is consistent with the simulation result. However, the translation residuals obtained using the POE method are much larger than those obtained using the D-K and PN methods. The computation time of the POE method is also longer than the other two methods.

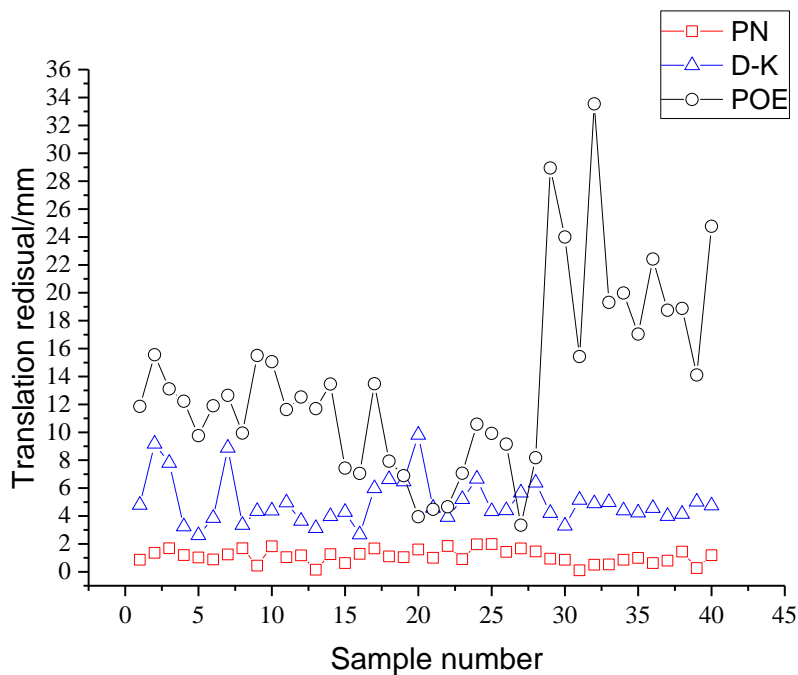


Figure 6-7: Translation residuals obtained using the POE, D-K and the PN method

Table 6-3: Average residuals and average computation time obtained with the POE, D-K and PN methods

	Average rotation residual	Average translation residual/mm	Average time/ms
POE method	0.0438	13.4540	5887.4
D-K method	0.0113	4.8609	1322.9
PN method	0.0109	1.1004	1873.6

6.6 Conclusion

This chapter proposes three different methods for the registration of a hybrid robot. Various solutions have been described by many researchers for HEC and RWHEC. To the best of the author's knowledge, this chapter gives a first attempt to propose methods to address this issue for a hybrid robot. This issue can be solved using the D-K method, which is a closed-form solution, with three steps. Besides the D-K method, the POE and PN method can solve the problem using nonlinear iterative techniques.

Simulation results show that these methods are capable of obtaining globally optimal solutions. The methods are robust to noise. With the simulation results, it is found that the PN method is more accurate than the other two methods. Due to the degradation and orthogonal constraint in the D-K method, this method cannot achieve better accuracy than the PN method. The assumption adopted in the POE method worsens its accuracy as shown in the simulation results.

In practice, the D-K method requires shorter computation time and is not affected by noise, which can be attributed to its closed form. Different from the D-K method, better accuracy and longer computation time of the PN

method have been validated with an experiment. The POE method has longer computation time compared to the D-K method. The experiment shows that the result obtained using the POE method is the worst. Hence, it is not a good choice to select the POE method to solve this registration problem.

In conclusion, the proposed methods can obtain optimal solutions of the registration of a hybrid robot, except for the POE method. The D-K method can be used to present an approximate solution under the requirement of shorter computation time or narrow the search area for the PN method, and the PN method is suitable for refining the solution.

CHAPTER 7 ACCURACY INVESTIGATION OF THE HYBRID ROBOT

In order to investigate the machining quality of the hybrid robot, its machining accuracy is compared with a CNC machining center and the serial robot which is used to construct the hybrid robot in this chapter. This chapter does not intend to provide an exhaustive test of the machining accuracy, while several basic criteria of machining qualities are investigated, such as circularity of a circular path, straightness of a linear path and cylindricity of a drilled hole.

7.1 Materials

In order to compare the circularity, straightness and cylindricity, the workpiece described in Figure 7-1 is to be machined using the hybrid robot, the serial robot and a CNC machining center. The two straight sides plotted in Figure 7-1 which are denoted using L1 and L2 are used to test the straightness of the machines, the semi-circle platform is for the circularity and two holes denoted using H1 and H2 are for the cylindricity. The material of the workpiece is machining wax. The information of the serial robot and the CNC machining center is listed in Table 7-1. The accuracy of the CNC machining center refers to its positional uncertainty according to VDI/DGQ 3441/ISO 230-2.

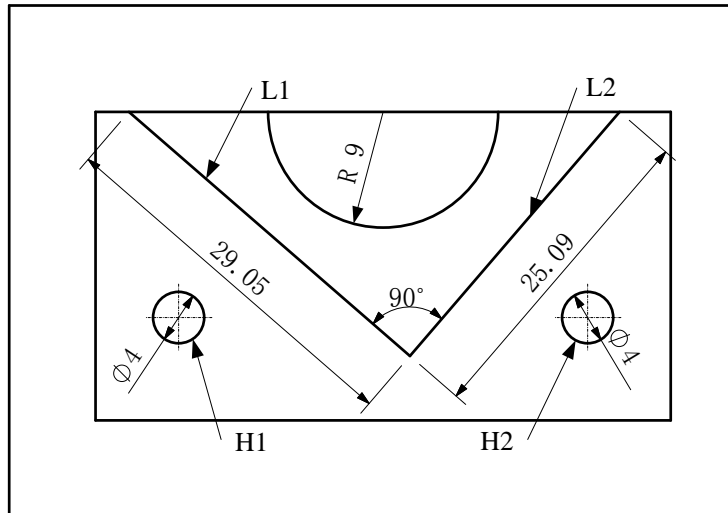


Figure 7-1: The top view of the workpiece

Table 7-1: Information of the serial robot, the CNC machining center and the CMM

	The Serial robot	The CNC machining center	The CMM
Product name	SCORBOT – ER VII	DMU 80 P duo BLOCK	DEA GAMMA 0101
Manufacturer	ESHED ROBOTEC INC.	DMG MORI SEIKI CO., LTD.	DEA
Accuracy (Claimed by manufacturer)	0.2mm	0.005mm	4+4L/1000 (VDI/VDE 2617)

After the completion of machining, a coordinate measuring machine (CMM) is used to obtain the quality of the machined workpieces. The information of the CMM is listed in Table 7-1. The accuracy of the CMM is in microns, and L is the measurement length in millimeters.

7.2 Definitions

7.2.1 Circularity

The CMM is used to measure several points along a circular outline. These points can be fitted into a circle using the least-square method. The difference

between the radius of the best-fit circle and the nominal radius of the semi-circle platform depicted in Figure 7-1 is denoted using R_d . The distance range of all the measured points to the best-fit circle is denoted using R_i . The circularity is represented using both R_d and R_i , since R_d describes the difference between a machined circle and its nominal circle, and R_i describes the roundness of the machined circle.

7.2.2 Straightness

The positions of several points along a linear path can be obtained using the CMM. These sampled points can be fitted into a line using the least-square method. The distance range of these points to this best-fit line is denoted by L_i , and L_i represents the straightness of a machined outline.

7.2.3 Cylindricity

The CMM can be used to obtain the positions of several points on a cylindrical surface. These sampled points can be fitted on a cylinder. The difference between the radii of the best-fit cylindrical surface and its nominal surface is denoted using C_R . The distance range of all the points to the best-fit surface is denoted using C_i . The cylindricity is represented using both C_R and C_i .

7.3 Machining Results

Figure 7-2 plots the machined workpieces using the CNC machining center, the hybrid robot and the serial robot, and Figure 7-3 depicts surfaces of the semi-circle platforms of the workpieces. It can be seen that the machining

results of the CNC machining center is the best and the serial robot is the worst. The surface of the semi-circle platform machined using the CNC machining center is the flattest compared to the hybrid robot and the serial robot. Although the surface machined using the hybrid robot cannot be flatter than the CNC machining center, it is much better than the serial robot.

Table 7-2: Circularity, straightness and cylindricity of workpieces machined using the CNC system, the hybrid robot and the serial robot

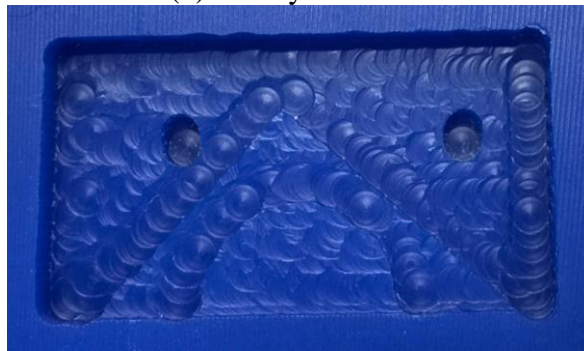
			The CNC machining center	The hybrid robot	The serial robot
Circularity/mm		R_d	0.0178	0.1279	0.6338
		R_i	[-0.0094, 0.0128]	[-0.0782, 0.0671]	[-0.4575, 0.5948]
Straightness/mm	L1	L_i	[-0.0216, 0.0145]	[-0.1717, 0.0966]	[-0.4825, 0.5853]
	L2	L_i	[-0.0205, 0.0194]	[-0.1615, 0.0720]	[-0.4907, 0.4736]
Cylindricity/mm	H1	C_R	0.0107	0.0988	0.5315
		C_i	[-0.0298, 0.0051]	[-0.0669, 0.0459]	[-0.4644, 0.3978]
	H2	C_R	0.0165	0.0884	0.4719
		C_i	[-0.0187, 0.0089]	[-0.0451, 0.0573]	[-0.4059, 0.5661]



(a) The CNC machining center



(b) The hybrid robot

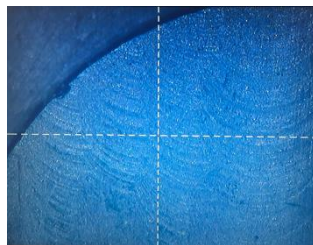


(c) The serial robot

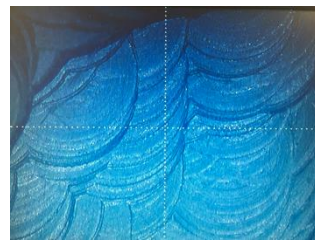
Figure 7-2: The machined workpieces using the CNC machining center, the hybrid robot and the serial robot



(a) The CNC machining center



(b) The hybrid robot



(c) The serial robot

Figure 7-3: Surfaces of the semi-circle platforms machined using the CNC machining center, the hybrid robot and the serial robot

Table 7-2 lists circularity, straightness and cylindricity of the machined workpieces using the CNC machining center, the hybrid robot and the serial robot.

The ranges of circularity, straightness and cylindricity are depicted in Figure 7-4. Since straightness and cylindricity evaluates two straight sides and two holes specifically, the errors of the sampled points are combined to obtain the statistical boxes for the straightness and cylindricity in Figure 7-4. Table 7-2 and Figure 7-4 show clearly that circularity, straightness and cylindricity of the workpiece machined using the hybrid robot is worse than the CNC machining center, but the hybrid robot improves significantly in geometrical errors compared to the serial robot. For example, the workpiece machined using the serial robot has circularity error within the interval (-0.5, 0.6), while the circularity of the workpiece machined using the hybrid robot is within the interval (-0.08, 0.07), which is at least one sixth of the error of the serial robot. It can be stated that the accuracy of the hybrid robot is much better than the serial robot.

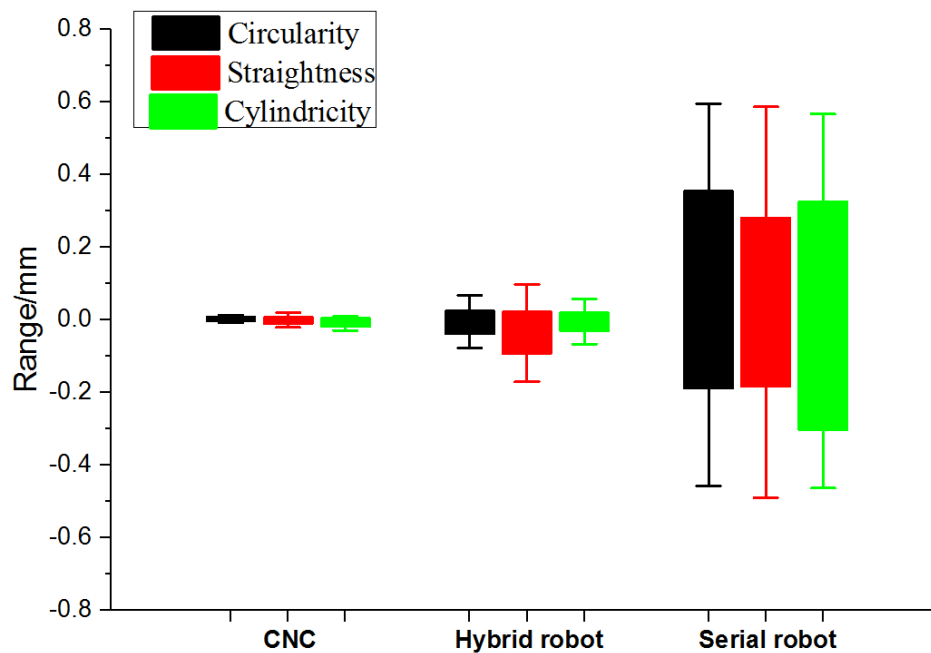


Figure 7-4: The error ranges of the workpieces machined using the CNC machine, the hybrid robot and the serial robot

7.4 Conclusion

This chapter provides accuracy comparisons among a CNC machining center, the hybrid robot constructed in this study and the serial robot which is used to build the hybrid robot. After the machining of workpieces with the same geometry and material, the circularity, straightness and cylindricity of the workpieces is obtained using a CMM. Although the accuracy of the hybrid robot is lower than the CNC machining center, measurement results show clearly that the accuracy of the hybrid robot is much better than the serial robot.

It should be noted that the hybrid robot is more flexible than the CNC machining center. If the dimension of the triglide is decreased further with the requirement of a smaller task space, and the clearance within the passive joints of the triglide can be minimized, and the accuracy of the hybrid robot may be better.

CHAPTER 8 CONCLUSIONS AND FUTURE WORKS

8.1 Conclusions and contributions

A hybrid robot consisting of a serial robot and a parallel manipulator has been constructed to achieve MOCS. The serial robot works as a rough positioner and the parallel manipulator carries out the machining operations. The parallel manipulator is a 3-DOF pure translational mechanism which uses parallelogram-type limbs to constrain the orientations of its mobile platform. This group of manipulators with similar structures is termed triglides.

To improve the performance of a general triglide, its workspace and stiffness are analyzed. This study uses a geometrical method to obtain the workspace boundary and workspace volume of a general triglide, since it is faster and more accurate. An algebraic expression is provided to obtain the stiffness matrix of a general triglide, and a novel VW index is proposed to reflect its stiffness property considering the applied external wrench on its mobile platform.

An optimization method is presented to improve the dexterity, stiffness and space utilization of a general triglide considering practical constraints, such as the motion range of passive joints and the requirement of task space. With the proposed methodology, an optimal triglide is constructed. The triglide is attached on a 5-axis serial robot to form a hybrid robot.

Since it is crucial to register the hybrid robot to link the robot with a tracking system, this study uses three different methods to address the registration problem. These methods are compared to evaluate their accuracy and computation time.

Finally, in order to investigate the machining accuracy of the hybrid robot, it is compared with a CNC machining center and a serial robot. With the machining of workpieces under the same geometry and material, it is proven that the hybrid robot is able to achieve much better accuracy than the serial robot, although the accuracy of the hybrid robot is not comparable to the CNC machining center.

The main contributions made in this study can be summarized as follows.

1. A geometrical method has been proposed for the workspace analysis of a general triglide. Although workspace analysis of the orthoglide and the linear delta which belongs to the group of triglide have been reported, the workspace analysis of a general triglide is still lacking. With the comparison with a discretization method which is popular to obtain the workspace of a parallel manipulator, it is found that the geometrical method is more accurate and faster than the discretization method if high resolution is required. With the geometrical method, it is also more convenient to find regular workspace to represent approximately the true workspace, since the true workspace is irregular, and can cause some difficulties in path planning or the estimation of a task space.

2. An algebraic expression is provided to obtain the stiffness matrix of a general triglide. The stiffness analysis of parallel manipulators has been addressed by many researchers. However, most of them have ignored the deformation of the mobile platform while conducting the stiffness analysis. Additionally, there is no reported algebraic expression for the stiffness analysis of a general triglide. Comparing with an FEA method, the algebraic expression is able to reach comparable accuracy with FEA results, but the algebraic method is much faster and more convenient.
3. A new stiffness index has been proposed in this study. This index uses virtual work to avoid interpretation difficulty caused by the different units of translation and orientation, which can occur in several other stiffness indices, such as the indices of eigenvalues and determinant. Compared to these indices, the proposed index can relate its value to the direction of the wrench experienced by a parallel manipulator in an operation, since this index measures the resistance of the parallel manipulator to deformation caused by the applied wrench. Generally, the direction of an applied wrench has a significant effect on the deformation of a parallel manipulator.
4. The optimization methodology proposed in this study aims to improve the dexterity, stiffness and space utilization of a general triglide. It is a first attempt to consider the compliance of the mobile platform, the limbs and the actuators in the stiffness optimization and the variable dimensional volume of a parallel manipulator due to its different postures in the space

utilization optimization. Compared to an optimal solution obtained by other researchers, this optimization methodology is able to provide a better solution, which improves the GDI of the triglide by 75.26%, the GSI by 42.79% and the RWV by 2.44%.

5. This study proposes three different methods for the registration of a hybrid robot. Although various solutions have been described by many researchers for HEC and RWHEC, this study presents a first attempt to address this issue for a hybrid robot. All the proposed methods can provide globally robust solutions. The proposed D-K method requires the shortest computation time and its computation time is not affected by noise, while the PN method has the best accuracy but it needs longer computation time under perturbation, while the result obtained using the POE method is the worst. Hence, the D-K method can be used to present an approximate solution under the requirement of shorter computation time or narrow the search area for the PN method, and the PN method is suitable for refining a solution. It is not a good choice to select the POE method to solve this registration problem.

8.2 Future works

This study has designed and constructed an optimal hybrid robot focusing on performance improvement of the parallel manipulator which is used to form the hybrid robot and address the registration of the hybrid robot to link it with a tracking system. Although this study has attempted to address the workspace

and stiffness issues to improve the performance of the hybrid robot, additional studies can be undertaken in the following directions.

1. The stiffness of the serial robot has important influence on the accuracy of the hybrid robot. Research can be carried out to improve the stiffness of a serial robot. It should be noted that the stiffness of a serial robot is in conflict with its flexibility, and it is difficult to achieve optimal stiffness and flexibility simultaneously. However, the serial robot is expected to be locked after positioning the parallel manipulator during an operation. Future research can focus on the stiffness improvement of a locked serial robot.
2. The clearance within the passive joints in a parallel manipulator can affect its stiffness and accuracy. Since it is difficult to avoid clearance in practice, clearance analysis and modelling can help build an efficient compensation system to improve the accuracy of a parallel manipulator.
3. Although it is challenging to set up the precise experimental configuration to investigate the stiffness of a multi-body robot, experimental methods should be used to validate the mechanical design. The main challenge is the isolation of the displacement caused by deformation from that caused by other error sources, such as clearance and actuator backlash. Future research can be undertaken on displacement investigation due to error sources. If the effect of the error sources can be analyzed, it will be easier to identify solutions for the deformation.

Apart from machining operations, the combined flexibility and accuracy of the hybrid robot is feasible to be applied in surgical operations, bearing in mind the stringent medical conditions which must be met. The robotic systems for surgical operations generally use serial robots or parallel manipulators as the main operation tools. The hybrid robot is able to achieve larger workspace than a parallel manipulator and with higher accuracy than a serial robot. Hence, the research in this field could improve the performance of robots applied in robotic surgery.

REFERENCES

- [1] G. C. Loney and T. M. Ozsoy, "NC machining of free form surfaces," *Computer-Aided Design*, vol. 19, no. 2, pp. 85–90, Mar. 1987.
- [2] L. N. López de Lacalle and A. Lamikiz, "Sculptured Surface Machining," in *Machining*, J. P. Davim, Ed. Springer London, 2008, pp. 225–248.
- [3] H. Tam, O. Chi-hang Lui, and A. C.K. Mok, "Robotic polishing of free-form surfaces using scanning paths," *Journal of Materials Processing Technology*, vol. 95, no. 1–3, pp. 191–200, Oct. 1999.
- [4] H. Kihlman, G. Ossbahr, M. Engström, and J. Anderson, "Low-Cost Automation for Aircraft Assembly," in *SAE Technical Paper*, 2004, pp. 2004–01–2830.
- [5] B. Roy and H. H. Asada, "Design of a Reconfigurable Robot Arm for Assembly Operations inside an Aircraft Wing-Box," in *Proceedings of the 2005 IEEE International Conference on Robotics and Automation*, 2005, pp. 590–595.
- [6] P. Webb, S. Eastwood, N. Jayaweera, and Y. Chen, "Automated aerostructure assembly," *The Industrial Robot*, vol. 32, no. 5, pp. 383–387, 2005.
- [7] R. DeVlieg and E. Feikert, "One-Up Assembly with Robots," in *SAE Technical Paper*, 2008, pp. 2008–01–2297.
- [8] A. P. Schulz, K. Seide, C. Queitsch, A. von Haugwitz, J. Meiners, B. Kienast, M. Tarabolsi, M. Kammal, and C. Jürgens, "Results of total hip replacement using the Robodoc surgical assistant system: clinical outcome and evaluation of complications for 97 procedures," *The International Journal of Medical Robotics and Computer Assisted Surgery*, vol. 3, no. 4, pp. 301–306, 2007.
- [9] R. Tarwala and L. Dorr, "Robotic assisted total hip arthroplasty using the MAKO platform," *Current Reviews in Musculoskeletal Medicine*, vol. 4, no. 3, pp. 151–156, 2011.
- [10] J. Kim, F. C. Park, and J. M. Lee, "A New Parallel Mechanism Machine Tool Capable of Five-Face Machining," *CIRP Annals - Manufacturing Technology*, vol. 48, no. 1, pp. 337–340, Jan. 1999.
- [11] V. B. Saputra, "DEVELOPMENT OF TWO COOPERATIVE STEWART PLATFORMS FOR MACHINING," National University of Singapore, 2012.

- [12] P. Tang, L. Hu, H. Du, M. Gong, and L. Zhang, "Novel 3D hexapod computer-assisted orthopaedic surgery system for closed diaphyseal fracture reduction," *The International Journal of Medical Robotics and Computer Assisted Surgery*, vol. 8, no. 1, pp. 17–24, 2012.
- [13] Y. Koren, *Computer Control of Manufacturing Systems*, 1st ed. New York: McGraw-Hill, Inc., 1983.
- [14] R. Devlieg, K. Sitton, E. Feikert, and J. Inman, "ONCE (ONe-sided Cell End effector) Robotic Drilling System," in *SAE Technical Paper*, 2002, pp. 2002–01–2626.
- [15] M. Saadat and L. Cretin, "Measurement systems for large aerospace components," *Sensor Review*, vol. 22, no. 3, pp. 199–206, 2002.
- [16] N. Jayaweera and P. Webb, "Automated assembly of fuselage skin panels," *Assembly Automation*, vol. 27, no. 4, pp. 343–355, 2007.
- [17] G. Mosqueira, J. Apetz, K. M. Santos, E. Villani, R. Suterio, and L. G. Trabasso, "Analysis of the indoor GPS system as feedback for the robotic alignment of fuselages using laser radar measurements as comparison," *Robotics and Computer-Integrated Manufacturing*, vol. 28, no. 6, pp. 700–709, Dec. 2012.
- [18] E. C. Pua, M. P. Fronheiser, J. R. Noble, E. D. Light, P. D. Wolf, D. von Allmen, and S. W. Smith, "3-D ultrasound guidance of surgical robotics: a feasibility study," *Ultrasonics, Ferroelectrics and Frequency Control, IEEE Transactions on*, vol. 53, no. 11, pp. 1999–2008, 2006.
- [19] D. V Amin, T. Kanade, A. M. Digioia, and B. Jaramaz, "Ultrasound Registration of the Bone Surface for Surgical Navigation," *Computer Aided Surgery*, vol. 8, no. 1, pp. 1–16, 2003.
- [20] G. J. Bootsma, J. H. Siewerdsen, M. J. Daly, and D. A. Jaffray, "Initial investigation of an automatic registration algorithm for surgical navigation," *Engineering in Medicine and Biology Society, 2008. EMBS 2008. 30th Annual International Conference of the IEEE*. pp. 3638–3642, 2008.
- [21] K. Logishetty, A. Bedi, and A. S. Ranawat, "The Role of Navigation and Robotic Surgery in Hip Arthroscopy," *Operative Techniques in Orthopaedics*, vol. 20, no. 4, pp. 255–263, 2010.
- [22] A. Mozes, T.-C. Chang, L. Arata, and W. Zhao, "Three-dimensional A-mode ultrasound calibration and registration for robotic orthopaedic knee surgery," *The International Journal of Medical Robotics and Computer Assisted Surgery*, vol. 6, no. 1, pp. 91–101, 2010.

- [23] J. P. Merlet, "Parallel robots - Open problems," in *Proceedings of the 9th International Symposium of Robotics Research*, pp. 27–32.
- [24] R. E. Stamper, T. Lung-Wen, and G. C. Walsh, "Optimization of a three DOF translational platform for well-conditioned workspace," in *Robotics and Automation, 1997. Proceedings., 1997 IEEE International Conference on*, 1997, vol. 4, pp. 3250–3255 vol.4.
- [25] L. W. Tsai and S. Joshi, "Kinematics and Optimization of a Spatial 3-UPU Parallel Manipulator," *Journal of Mechanical Design*, vol. 122, pp. 439–446, 2000.
- [26] H. S. Kim and L.-W. Tsai, "Design Optimization of a Cartesian Parallel Manipulator," *Journal of Mechanical Design*, vol. 125, no. 1, p. 43, 2003.
- [27] B. Monsarrat and C. M. Gosselin, "Workspace analysis and optimal design of a 3-leg 6-DOF parallel platform mechanism," *Robotics and Automation, IEEE Transactions on*, vol. 19, no. 6, pp. 954–966, 2003.
- [28] X.-J. Liu, "Optimal kinematic design of a three translational DoFs parallel manipulator," *Robotica*, vol. 24, no. 02, pp. 239–250, 2006.
- [29] A. B. K. Rao, P. V. M. Rao, and S. K. Saha, "Dimensional design of hexaslides for optimal workspace and dexterity," *Robotics, IEEE Transactions on*, vol. 21, no. 3, pp. 444–449, 2005.
- [30] D. Chablat and P. Wenger, "Architecture Optimization of a 3-DOF Translational Parallel Mechanism for Machining Applications, the Orthoglide," *Robotics and Automation, IEEE Transactions on*, vol. 2000, pp. 1–8, Aug. 2007.
- [31] Y. J. Lou, G. F. Liu, and Z. X. Li, "Randomized Optimal Design of Parallel Manipulators," *Automation Science and Engineering, IEEE Transactions on*, vol. 5, no. 2, pp. 223–233, 2008.
- [32] O. Altuzarra, C. Pinto, B. Sandru, and A. Hernandez, "Optimal Dimensioning for Parallel Manipulators: Workspace, Dexterity, and Energy," *Journal of Mechanical Design*, vol. 133, no. 4, p. 41007, 2011.
- [33] M. Laribi, L. Romdhane, and S. Zeghloul, "Analysis and dimensional synthesis of the DELTA robot for a prescribed workspace," *Mechanism and Machine Theory*, vol. 42, no. 7, pp. 859–870, 2007.
- [34] S. Herrero, T. Mannheim, I. Prause, C. Pinto, B. Corves, and O. Altuzarra, "Enhancing the useful workspace of a reconfigurable parallel manipulator by grasp point optimization," *Robotics and Computer-Integrated Manufacturing*, vol. 31, pp. 51–60, Feb. 2015.

- [35] J. Aginaga, I. Zabalza, O. Altuzarra, and J. Nájera, “Improving static stiffness of the parallel manipulator using inverse singularities,” *Robotics and Computer-Integrated Manufacturing*, vol. 28, no. 4, pp. 458–471, Aug. 2012.
- [36] G. Cheng, P. Xu, D. Yang, and H. Liu, “Stiffness analysis of a 3CPS parallel manipulator for mirror active adjusting platform in segmented telescope,” *Robotics and Computer-Integrated Manufacturing*, vol. 29, no. 5, pp. 302–311, Oct. 2013.
- [37] A. Rezaei, A. Akbarzadeh, and M.-R. Akbarzadeh-T, “An investigation on stiffness of a 3-PSP spatial parallel mechanism with flexible moving platform using invariant form,” *Mechanism and Machine Theory*, vol. 51, pp. 195–216, 2012.
- [38] B. Hu, Y. Lu, Q. Tan, J. Yu, and J. Han, “Analysis of stiffness and elastic deformation of a 2(SP+SPR+SPU) serial–parallel manipulator,” *Robotics and Computer-Integrated Manufacturing*, vol. 27, no. 2, pp. 418–425, Apr. 2011.
- [39] B. Hu and Y. Lu, “Solving stiffness and deformation of a 3-UPU parallel manipulator with one translation and two rotations,” *Robotica*, vol. 29, no. 06, pp. 815–822, Jan. 2011.
- [40] A. Pashkevich, D. Chablat, and P. Wenger, “Stiffness analysis of overconstrained parallel manipulators,” *Mechanism and Machine Theory*, vol. 44, no. 5, pp. 966–982, May 2009.
- [41] B. S. El-Khasawneh and P. M. Ferreira, “Computation of stiffness and stiffness bounds for parallel link manipulators,” *International Journal of Machine Tools and Manufacture*, vol. 39, no. 2, pp. 321–342, Feb. 1999.
- [42] C. Gosselin, “Stiffness mapping for parallel manipulators,” *IEEE Transactions on Robotics and Automation*, vol. 6, no. 3, pp. 377–382, Jun. 1990.
- [43] G. Carbone and M. Ceccarelli, “Comparison of indices for stiffness performance evaluation,” *Frontiers of Mechanical Engineering in China*, vol. 5, no. 3, pp. 270–278, May 2010.
- [44] Y. Shiu and S. Ahmad, “Calibration of wrist-mounted robotic sensors by solving homogeneous transform equations of the form $AX=XB$,” *Robotics and Automation, IEEE Transactions on*, vol. 5, no. 1, pp. 16–29, 1989.
- [45] L. Richter, F. Ernst, A. Schlaefler, and A. Schweikard, “Robust real-time robot–world calibration for robotized transcranial magnetic stimulation,” *The International Journal of Medical Robotics and Computer Assisted Surgery*, vol. 7, no. 4, pp. 414–422, Dec. 2011.

- [46] J. C. K. Chou and M. Kamel, "Finding the Position and Orientation of a Sensor on a Robot Manipulator Using Quaternions," *The International Journal of Robotics Research*, vol. 10, no. 3, pp. 240–254, Jun. 1991.
- [47] R. Horaud and F. Dornaika, "Hand-Eye Calibration," *The International Journal of Robotics Research*, vol. 14, no. 3, pp. 195–210, Jun. 1995.
- [48] K. Daniilidis, "Hand-Eye Calibration Using Dual Quaternions," *The International Journal of Robotics Research*, vol. 18, no. 3, pp. 286–298, Mar. 1999.
- [49] H. Chen, "A screw motion approach to uniqueness analysis of head-eye geometry," in *Computer Vision and Pattern Recognition, 1991. Proceedings CVPR '91., IEEE Computer Society Conference on*, 1991, pp. 145–151.
- [50] M. K. Ackerman and G. S. Chirikjian, "A Probabilistic Solution to the $AX = XB$ Problem : Sensor Calibration without Correspondence," in *Geometric Science of Information*, F. Nielsen and F. Barbaresco, Eds. Springer Berlin Heidelberg, 2013, pp. 693–701.
- [51] F. Dornaika and R. Horaud, "Simultaneous robot-world and hand-eye calibration," *Robotics and Automation, IEEE Transactions on*, vol. 14, no. 4, pp. 617–622, 1998.
- [52] A. Li, L. Wang, and D. Wu, "Simultaneous robot-world and hand-eye calibration using dual-quaternions and Kronecker product," *International Journal of Physical Sciences*, vol. 5, no. 10, pp. 1530–1536, 2010.
- [53] H. Q. Zhuang, Z. S. Roth, and R. Sudhakar, "Simultaneous robot/world and tool/flange calibration by solving homogeneous transformation equations of the form $AX=YB$," *Robotics and Automation, IEEE Transactions on*, vol. 10, no. 4, pp. 549–554, 1994.
- [54] R. L. Hirsh, G. N. DeSouza, and A. C. Kak, "An iterative approach to the hand-eye and base-world calibration problem," in *Robotics and Automation, 2001. Proceedings 2001 ICRA. IEEE International Conference on*, 2001, vol. 3, pp. 2171–2176.
- [55] K. Strobl and G. Hirzinger, "Optimal Hand-Eye Calibration," in *Intelligent Robots and Systems, 2006 IEEE/RSJ International Conference on*, 2006, no. 3, pp. 4647–4653.
- [56] H.-S. Choi, C.-S. Han, K. Lee, and S. Lee, "Development of hybrid robot for construction works with pneumatic actuator," *Automation in Construction*, vol. 14, no. 4, pp. 452–459, Aug. 2005.
- [57] H. Liu, T. Huang, J. Mei, X. Zhao, D. G. Chetwynd, M. Li, and S. Jack Hu, "Kinematic Design of a 5-DOF Hybrid Robot with Large

- Workspace/Limb–Stroke Ratio,” *Journal of Mechanical Design*, vol. 129, no. 5, p. 530, 2007.
- [58] D. Pisla, B. Gherman, C. Vaida, M. Suciu, and N. Plitea, “An active hybrid parallel robot for minimally invasive surgery,” *Robotics and Computer-Integrated Manufacturing*, vol. 29, no. 4, pp. 203–221, 2013.
- [59] T. Nakano, N. Sugita, T. Ueta, Y. Tamaki, and M. Mitsuishi, “A parallel robot to assist vitreoretinal surgery,” *International Journal of Computer Assisted Radiology and Surgery*, vol. 4, no. 6, pp. 517–526, 2009.
- [60] G. Carbone and M. Ceccarelli, “A Serial-parallel robotic architecture for surgical tasks,” *Robotica*, vol. 23, no. 03, pp. 345–354, 2005.
- [61] A. B. K. Rao, P. V. M. Rao, and S. K. Saha, “Workspace and dexterity analyses of hexaslide machine tools,” in *Robotics and Automation, 2003. Proceedings. ICRA '03. IEEE International Conference on*, 2003, vol. 3, pp. 4104–4109 vol.3.
- [62] G. Cheng, B. Qiu, D. Yang, and H. Liu, “Workspace analysis of 3-CPS parallel micro-manipulator for mirror active adjusting platform,” *Journal of Mechanical Science and Technology*, vol. 27, no. 12, pp. 3805–3816, Dec. 2013.
- [63] A. Rezaei, A. Akbarzadeh, P. M. Nia, and M.-R. Akbarzadeh-T, “Position, Jacobian and workspace analysis of a 3-PSP spatial parallel manipulator,” *Robotics and Computer-Integrated Manufacturing*, vol. 29, no. 4, pp. 158–173, Aug. 2013.
- [64] Z. Wang, Z. Wang, W. Liu, and Y. Lei, “A study on workspace, boundary workspace analysis and workpiece positioning for parallel machine tools,” *Mechanism and Machine Theory*, vol. 36, no. 5, pp. 605–622, 2001.
- [65] A. K. Dash, I.-M. Chen, S. H. Yeo, and G. Yang, “Workspace generation and planning singularity-free path for parallel manipulators,” *Mechanism and Machine Theory*, vol. 40, no. 7, pp. 776–805, Jul. 2005.
- [66] Z. Wang, S. Ji, Y. Li, and Y. Wan, “A unified algorithm to determine the reachable and dexterous workspace of parallel manipulators,” *Robotics and Computer-Integrated Manufacturing*, vol. 26, no. 5, pp. 454–460, Oct. 2010.
- [67] D.-Y. Jo and E. J. Haug, “Workspace Analysis of Multibody Mechanical Systems Using Continuation Methods,” *Journal of Mechanisms Transmissions and Automation in Design*, vol. 111, no. 4, p. 581, 1989.

- [68] L. T. Wang and J. Hsieh, "Extreme Reaches and Reachable Workspace Analysis of General Parallel Robotic Manipulators," *Journal of Robotic Systems*, vol. 15, no. 3, pp. 145–159, 1998.
- [69] V. B. Saputra, S. K. Ong, and a. Y. C. Nee, "A swarm optimization approach for solving workspace determination of parallel manipulators," *Robotica*, no. March, pp. 1–20, Mar. 2014.
- [70] C. Gosselin, "Determination of the Workspace of 6-DOF Parallel Manipulators," *Journal of Mechanical Design*, vol. 112, no. 3, pp. 331–336, Sep. 1990.
- [71] J. P. Merlet, "Determination of 6D Workspaces of Gough-Type Parallel Manipulator and Comparison between Different Geometries," *The International Journal of Robotics Research*, vol. 18, no. 9, pp. 902–916, 1999.
- [72] T. Huang, J. Wang, and D. J. Whitehouse, "Closed Form Solution to Workspace of Hexapod-Based Virtual Axis Machine Tools," *Journal of Mechanical Design*, vol. 121, no. 1, pp. 26–31, 1999.
- [73] T. C. Lee and M. H. Perng, "Analysis of simplified position and 5-DOF total orientation workspaces of a hexapod mechanism," *Mechanism and Machine Theory*, vol. 42, no. 12, pp. 1577–1600, 2007.
- [74] I. A. Bonev and J. Ryu, "A geometrical method for computing the constant-orientation workspace of 6-PRRS parallel manipulators," *Mechanism and Machine Theory*, vol. 36, no. 1, pp. 1–13, Jan. 2001.
- [75] R. Di Gregorio and R. Zanforlin, "Workspace analytic determination of two similar translational parallel manipulators," *Robotica*, vol. 21, no. 5, pp. 555–566, Oct. 2003.
- [76] a. Pashkevich, D. Chablat, and P. Wenger, "Kinematics and workspace analysis of a three-axis parallel manipulator: the Orthoglide," *Robotica*, vol. 24, no. 01, p. 39, Nov. 2006.
- [77] T. Huang, X. Zhao, and D. J. Whitehouse, "Stiffness estimation of a tripod-based parallel kinematic machine," *IEEE Transactions on Robotics and Automation*, vol. 18, no. 1, pp. 50–58, 2002.
- [78] C. Pinto, J. Corral, O. Altuzarra, and A. Hernández, "A methodology for static stiffness mapping in lower mobility parallel manipulators with decoupled motions," *Robotica*, vol. 28, no. 05, pp. 719–735, Sep. 2009.
- [79] C. Gosselin and J. Angeles, "A Global Performance Index for the Kinematic Optimization of Robotic Manipulators," *Journal of Mechanical Design*, vol. 113, pp. 220–226, 1991.

- [80] S. Joshi and T. Lung-Wen, "A comparison study of two 3-DOF parallel manipulators: one with three and the other with four supporting legs," in *Robotics and Automation, 2002. Proceedings. ICRA '02. IEEE International Conference on*, 2002, vol. 4, pp. 3690–3697 vol.4.
- [81] J. P. Merlet, "Jacobian, Manipulability, Condition Number, and Accuracy of Parallel Robots," *Journal of Mechanical Design*, vol. 128, no. 1, pp. 199–206, 2006.
- [82] T. Huang, M. Li, X. M. Zhao, J. P. Mei, D. G. Chetwynd, and S. J. Hu, "Conceptual design and dimensional synthesis for a 3-DOF module of the TriVariant-a novel 5-DOF reconfigurable hybrid robot," *Robotics, IEEE Transactions on*, vol. 21, no. 3, pp. 449–456, 2005.
- [83] X.-J. Liu, Z.-L. Jin, and F. Gao, "Optimum design of 3-DOF spherical parallel manipulators with respect to the conditioning and stiffness indices," *Mechanism and Machine Theory*, vol. 35, no. 9, pp. 1257–1267, 2000.
- [84] R. Unal, G. Kiziltas, and V. Patoglu, "Multi-criteria Design Optimization of Parallel Robots," in *Robotics, Automation and Mechatronics, 2008 IEEE Conference on*, 2008, pp. 112–118.
- [85] S. D. Stan, M. Manic, V. Maties, and R. Balan, "Evolutionary approach to optimal design of 3 DOF translation exoskeleton and medical parallel robots," in *Human System Interactions, 2008 Conference on*, 2008, pp. 720–725.
- [86] C. M. Fonseca and P. J. Fleming, "An Overview of Evolutionary Algorithms in Multiobjective Optimization," *Evolutionary Computation*, vol. 3, no. 1, pp. 1–16, 1995.
- [87] E. Zitzler and L. Thiele, "Multiobjective evolutionary algorithms: a comparative case study and the strength Pareto approach," *Evolutionary Computation, IEEE Transactions on*, vol. 3, no. 4, pp. 257–271, 1999.
- [88] P. K. Shukla and K. Deb, "On finding multiple Pareto-optimal solutions using classical and evolutionary generating methods," *European Journal of Operational Research*, vol. 181, no. 3, pp. 1630–1652, 2007.
- [89] K. Deb, A. Pratap, S. Agarwal, and T. Meyarivan, "A fast and elitist multiobjective genetic algorithm: NSGA-II," *Evolutionary Computation, IEEE Transactions on*, vol. 6, no. 2, pp. 182–197, 2002.
- [90] R. Y. Tsai and R. K. Lenz, "A new technique for fully autonomous and efficient 3D robotics hand/eye calibration," *Robotics and Automation, IEEE Transactions on*, vol. 5, no. 3, pp. 345–358, Jun. 1989.

- [91] N. Andreff, R. Horaud, and B. Espiau, "On-line hand-eye calibration," in *Second International Conference on 3-D Digital Imaging and Modeling, 1999 Proceedings*, 1999, pp. 430–436.
- [92] Z. Zhao and Y. Liu, "A hand–eye calibration algorithm based on screw motions," *Robotica*, vol. 27, no. 02, pp. 217–223, May 2008.
- [93] A. Malti, "Hand–eye calibration with epipolar constraints: Application to endoscopy," *Robotics and Autonomous Systems*, vol. 61, no. 2, pp. 161–169, Nov. 2013.
- [94] Z. Zhao and Y. Weng, "A flexible method combining camera calibration and hand–eye calibration," *Robotica*, vol. 31, no. 05, pp. 747–756, Feb. 2013.
- [95] Y. Motai and A. Kosaka, "Hand–Eye Calibration Applied to Viewpoint Selection for Robotic Vision," *IEEE Transactions on Industrial Electronics*, vol. 55, no. 10, pp. 3731–3741, Oct. 2008.
- [96] M. Shah, "Solving the Robot-World/Hand-Eye Calibration Problem Using the Kronecker Product," *Journal of Mechanisms and Robotics*, vol. 5, no. 3, p. 031007, Jun. 2013.
- [97] F. Ernst, L. Richter, L. Matth äus, V. Martens, R. Bruder, A. Schlaefer, and A. Schweikard, "Non-orthogonal tool/flange and robot/world calibration," *The International Journal of Medical Robotics and Computer Assisted Surgery*, vol. 8, no. 4, pp. 407–420, Dec. 2012.
- [98] C. Budde, P. Last, and J. Hesselbach, "Development of a Triglide-Robot with Enlarged Workspace," in *Robotics and Automation, 2007 IEEE International Conference on*, pp. 543–548.
- [99] Y. Lou, Z. Li, Y. Zhong, J. Li, and Z. Li, "Dynamics and contouring control of a 3-DoF parallel kinematics machine," *Mechatronics*, vol. 21, no. 1, pp. 215–226, 2011.
- [100] C. C. Ng, S. K. Ong, and A. Y. C. Nee, "Design and development of 3–DOF modular micro parallel kinematic manipulator," *The International Journal of Advanced Manufacturing Technology*, vol. 31, no. 1–2, pp. 188–200, 2006.
- [101] R. Clavel, "Device for the movement and positioning of an element in space," 49765821990.
- [102] M. Hebsacker, T. Treib, O. Zirn, and M. Honegger, "Hexaglide 6 DOF and Triaglide 3 DOF Parallel Manipulators," in *Parallel Kinematic Machines*, 1st ed., C. R. B. MAS, L. Molinari-Tosatti, and K. S. Smith, Eds. Springer London, 1999, pp. 345–355.

- [103] P. Wenger and D. Chablat, “Kinematic Analysis of a New Parallel Machine Tool: The Orthoglide,” in *Advances in Robot Kinematics*, J. Lenarčič and M. M. Stanišić, Eds. Springer Netherlands, 2000, pp. 305–314.
- [104] R. Di Gregorio and P. C. Vincenzo, “Mobility Analysis of the 3-UPU Parallel Mechanism Assembled for a Pure Translational Motion,” *Journal of Mechanical Design*, vol. 124, no. 2, pp. 259–264, 2002.
- [105] Y. Li and Q. Xu, “Stiffness analysis for a 3-PUU parallel kinematic machine,” *Mechanism and Machine Theory*, vol. 43, no. 2, pp. 186–200, 2008.
- [106] C. Han, J. Kim, J. Kim, and F. C. Park, “Kinematic sensitivity analysis of the 3-UPU parallel mechanism,” *Mechanism and Machine Theory*, vol. 37, no. 8, pp. 787–798, 2002.
- [107] L.-W. Tsai, “Structural Analysis of Mechanisms,” in *Mechanism Design: Enumeration of Kinematic Structures According to Function*, L.-W. Tsai, Ed. CRC Press, 2000.
- [108] J. Merlet, *Parallel Robots*, Second Edi., vol. 128. Berlin/Heidelberg: Springer-Verlag, 2006.
- [109] Q. Xu and Y. Li, “GA-Based Architecture Optimization of a 3-PUU Parallel Manipulator for Stiffness Performance,” in *Intelligent Control and Automation, 2006. WCICA 2006. The Sixth World Congress on*, vol. 2, pp. 9099–9103.
- [110] E. Courteille, D. Deblaise, and P. Maurine, “Design optimization of a Delta-like parallel robot through global stiffness performance evaluation,” in *2009 IEEE/RSJ International Conference on Intelligent Robots and Systems*, pp. 5159–5166.
- [111] Z.-F. Wang, S.-M. Ji, Y.-H. Wan, C.-J. Ou, J.-H. Sun, and G. Wang, “Optimal Design of Parallel Robots for the Prescribed Regular Dexterous Workspace,” in *Automation and Logistics, 2007 IEEE International Conference on*, pp. 563–568.
- [112] Z. Chi, D. Zhang, L. Xia, and Z. Gao, “Multi-objective optimization of stiffness and workspace for a parallel kinematic machine,” *International Journal of Mechanics and Materials in Design*, vol. 9, no. 3, pp. 281–293, Mar. 2013.
- [113] Z. Gao, D. Zhang, X. Hu, and Y. Ge, “Design, analysis, and stiffness optimization of a three degree of freedom parallel manipulator,” *Robotica*, vol. 28, no. 03, pp. 349–357, May 2010.

- [114] K. Miller, "Optimal Design and Modeling of Spatial Parallel Manipulators," *The International Journal of Robotics Research*, vol. 23, no. 2, pp. 127–140, 2004.
- [115] T. Yoshikawa, "Manipulability of Robotic Mechanisms," *The International Journal of Robotics Research*, vol. 4, no. 2, pp. 3–9, Jun. 1985.
- [116] G. Abbasnejad, H. M. Daniali, and A. Fathi, "Architecture optimization of 4PUS+1PS parallel manipulator," *Robotica*, vol. 29, no. 05, pp. 683–690, Sep. 2011.
- [117] M. Stock and K. Miller, "Optimal Kinematic Design of Spatial Parallel Manipulators: Application to Linear Delta Robot," *Journal of Mechanical Design*, vol. 125, no. 2, p. 292, 2003.
- [118] Y. Li and Q. Xu, "A New Approach to the Architecture Optimization of a General 3-PUU Translational Parallel Manipulator," *Journal of Intelligent & Robotic Systems*, vol. 46, no. 1, pp. 59–72, 2006.
- [119] I. M. Chen, G. Yang, C. T. Tan, and S. H. Yeo, "Local POE model for robot kinematic calibration," *Mechanism and Machine Theory*, vol. 36, no. 11–12, pp. 1215–1239, 2001.
- [120] X. Yang, L. Wu, J. Li, and K. Chen, "A minimal kinematic model for serial robot calibration using POE formula," *Robotics and Computer-Integrated Manufacturing*, vol. 30, no. 3, pp. 326–334, Jun. 2014.
- [121] H. Ruibo, Z. Yingjun, Y. Shunian, and Y. Shuzi, "Kinematic-Parameter Identification for Serial-Robot Calibration Based on POE Formula," *Robotics, IEEE Transactions on*, vol. 26, no. 3, pp. 411–423, 2010.
- [122] K. Okamura and F. C. Park, "Kinematic calibration using the product of exponentials formula," *Robotica*, vol. 14, no. 04, pp. 415–421, 1996.
- [123] G. Yang, I.-M. Chen, S. H. Yeo, and W. K. Lim, "Simultaneous base and tool calibration for self-calibrated parallel robots," *Robotica*, vol. 20, no. 04, pp. 367–374, Jun. 2002.

PUBLICATIONS FROM THE RESEARCH

- 1 S.J. Yan, S.K. Ong, A.Y.C. Nee, “A hybrid robot for robot-assisted orthopaedic surgery,” in *The 2013 World Congress on Advances in Nano, Biomechanics, Robotics, and Energy Research (ANBRE13)*, Seoul, South Korea, 25-28 August 2013, 164-176.
- 2 S.J. Yan, S.K. Ong, A.Y.C. Nee, “Registration of a hybrid robot using the Degradation-Kronecker method and a purely nonlinear method”, *Robotica*, accepted April 2015.
- 3 S.J. Yan, S.K. Ong, A.Y.C. Nee, “Stiffness analysis of parallelogram-type parallel manipulators using a strain energy method”, *Robotics and Computer-Integrated Manufacturing*, accepted May 2015.
- 4 S.J. Yan, S.K. Ong, A.Y.C. Nee, “Optimization design of general triglide parallel manipulators”, *Advanced Robotics*, April 2015, under review.